



HAL
open science

Mesozoic evolution of NW Africa: implications for the Central Atlantic Ocean dynamics

Rémi Leprêtre, Jocelyn Barbarand, Yves Missenard, Cécile Gautheron,
Rosella Pinna-Jamme, Omar Saddiqi

► **To cite this version:**

Rémi Leprêtre, Jocelyn Barbarand, Yves Missenard, Cécile Gautheron, Rosella Pinna-Jamme, et al.. Mesozoic evolution of NW Africa: implications for the Central Atlantic Ocean dynamics. *Journal of the Geological Society*, 2017, 174 (5), pp.817 - 835. 10.1144/jgs2016-100 . hal-01676091

HAL Id: hal-01676091

<https://hal.sorbonne-universite.fr/hal-01676091>

Submitted on 5 Jan 2018

HAL is a multi-disciplinary open access archive for the deposit and dissemination of scientific research documents, whether they are published or not. The documents may come from teaching and research institutions in France or abroad, or from public or private research centers.

L'archive ouverte pluridisciplinaire **HAL**, est destinée au dépôt et à la diffusion de documents scientifiques de niveau recherche, publiés ou non, émanant des établissements d'enseignement et de recherche français ou étrangers, des laboratoires publics ou privés.

1 **Mesozoic evolution of Northwest Africa: implications for the Central Atlantic**
2 **Ocean dynamics**

3
4 Rémi Leprêtre^{1,2,*}, Jocelyn Barbarand¹, Yves Missenard¹, Cécile Gautheron¹, Rosella Pinna-Jamme¹,
5 Omar Saddiqi³
6

7
8 ¹*Université Paris Sud-XI, Paris-Saclay, GEOPS, UMR 8148, Bâtiment 504, rue du Belvédère, F-91405,*
9 *Orsay, France*

10 ²*Université Pierre et Marie Curie Paris-VI, ITeP, UMR 7193, EMBS, 4 place Jussieu, 75005, Paris,*
11 *France*

12 ³*Université Hassan II, Faculté des Sciences, 20000, Casablanca 20000, Morocco*

13 *Correspondence (remi.lepretre@upmc.fr, remi.lep@gmail.com)
14
15

16 **Abbreviated title:** Mesozoic Evolution of NW Africa
17

18 **Abstract**

19 The Central Atlantic Ocean opened during the Early Jurassic and represents the oldest
20 portion of the Atlantic Ocean. Although the American margin has been well-studied, the onshore
21 evolution of its African counterpart is poorly understood. We investigated the evolution of a ~1300
22 km transect across the Reguibat Shield (Morocco, Mauritania, Algeria) in the northern West African
23 Craton using low-temperature thermochronology. Fourteen samples were dated using apatite
24 fission-track analysis. Nine of these samples were also dated using (U-Th-Sm)/He analysis. Fission-
25 track ages range from 118 ± 10 to 497 ± 61 Ma, with mean track lengths between 11.2 ± 0.4 and 12.5
26 ± 0.2 μm . (U-Th-Sm)/He single-grain ages range from 32 ± 3 Ma to 396 ± 32 Ma. Through forward and
27 inverse thermal modeling, we demonstrate that the craton underwent kilometeric exhumation
28 between the Early-Middle Jurassic and the Late Cretaceous. Based on our new results, published data
29 on Northwest Africa and data from the conjugate eastern North American passive margin, we show
30 that this post-rift Early-Middle Jurassic/Early Cretaceous exhumation affected both margins in a

31 similar areal extent and simultaneously. Transient mantle dynamic support is suggested as
32 accounting for the major erosional phase recorded on both margins.

33

34 **Supplementary material:** methodology for thermal modeling, individual thermal modeling for all
35 samples and the relationship between apatite chemistry and (U-Th)/He ages are available at
36 <https://figshare.com/s/05461f8ec0de274456c6>

37 **Keywords**

38 Low-temperature thermochronology – West African Craton – Central Atlantic Ocean – post-rift
39 evolution of passive margin – Reguibat Shield

40

41

42 **Introduction**

43 In the past two decades, substantial evidence has been presented to show that passive
44 margins are anything but passive. For example, the Atlantic-type margins have been thoroughly
45 studied and show repeated uplift or burial events in the course of their post-rift history (Gallagher *et*
46 *al.*, 1998; Turner *et al.*, 2008; Holford *et al.*, 2009; Japsen *et al.*, 2006, 2012; Cogné *et al.*, 2012; Green
47 *et al.*, 2013; Leprêtre *et al.*, 2015; Wildman *et al.*, 2015). These studies have demonstrated that the
48 precise determination of the timing of burial/uplift phase of the onshore margins can offer a better
49 understanding of the stratigraphical record along the margins (Japsen *et al.*, 2012). Despite the
50 evidence that passive margins are active features in plate tectonics, these studies also highlight the
51 poor knowledge we have on the underlying mechanisms controlling these processes (Japsen *et al.*,
52 2012; Green *et al.*, 2013 and references therein).

53 In order to better understand the underlying mechanisms controlling rift and post-rift
54 evolution, it is necessary to assess the simultaneous uplift/burial events on conjugate passive
55 margins (*e.g.* Turner *et al.*, 2008; Green & Duddy, 2010). In this study, we compare the stratigraphical
56 record of the conjugate margins of the Central Atlantic Ocean during the Mesozoic and the vertical
57 evolution of the onshore domains. These margins have received considerable attention in the past
58 (eastern North America: Sheridan & Grow, 1988; Miall, 2008; Northwest Africa: von Rad *et al.*, 1982;
59 Poag & Schlee, 1984), although there have been a limited number of comparison studies focusing on
60 their respective stratigraphical records (Jansa & Wiedmann, 1982; von Rad & Sarti, 1986) and no
61 study has ever compared the two margins considering their onshore evolutions. Many low-
62 temperature thermochronology studies have been undertaken along the onshore eastern North
63 American passive margin (Crowley, 1991; Wang *et al.*, 1994; Boettcher & Milliken, 1994; Roden-Tice
64 *et al.*, 2000; Roden-Tice & Wintsch, 2002; Grist & Zentilli, 2003; Lorencak *et al.*, 2004; Spotila *et al.*,
65 2004; Roden-Tice & Tice, 2005; Taylor & Fitzgerald, 2011; Roden-Tice *et al.*, 2012). However, along
66 the Northwest African passive margin, a similarly large coverage of onshore data is still lacking (first

67 data in Leprêtre *et al.*, 2014 and 2015) to achieve a detailed comparison of both margins and
68 addressing this issue is a major goal of this study.

69 This study reports low-temperature thermochronology (LTT) data across the whole range of
70 the northern West African Craton, which is the main continental domain of the eastern Central
71 Atlantic Ocean (Fig. 1a). We used apatite fission-track and (U-Th-Sm)/He (AFT and AHe, respectively)
72 LTT and thermal modeling techniques (Gallagher, 2012) to constrain the timing and amplitude of
73 erosion/burial events for Mesozoic-Cenozoic times. Given a 40-120°C thermal sensitivity, these
74 methods provide insights into the evolution of the uppermost 3-4 km of the crust (Gallagher *et al.*,
75 1998; Flowers *et al.*, 2009; Gautheron *et al.*, 2009, Djimbi *et al.*, 2015). We then combine our new LTT
76 study with the wealth of LTT data on the eastern American passive margin and the sedimentary
77 records of both conjugate passive margins. These data form the basis of our comparison between the
78 two margins and discussion of the Mesozoic evolution of the Central Atlantic Ocean.

79

80 **Geological setting**

81 Within the northern West African Craton (NWAC), the Reguibat Shield is a flat basement
82 domain, divided into a western Archean domain (> 2.5 Ga; Potrel *et al.*, 1998; Schofield *et al.*, 2012)
83 and an eastern Eburnean domain (2-2.2 Ga; Lahondère *et al.*, 2001; Peucat *et al.*, 2005). Its
84 westernmost tip is part of the Variscan Mauritanides (Villeneuve, 2008; Michard *et al.*, 2010). North
85 and south of the Reguibat Shield, the Tindouf and Taoudeni basins display a km-scale Paleozoic infill
86 (Boote *et al.*, 1998), unconformably lying on the Neoproterozoic rocks (Fig. 1b). Both basins have
87 large-scale synclinal shapes with low (5-10°) dipping flanks, with the exception of the steeper
88 northern flank of the Tindouf Basin, which was involved in the Variscan deformation (Burkhard *et al.*,
89 2006). Most authors acknowledge the existence of a continuous sedimentary realm until the Early
90 Carboniferous (Bertrand-Sarfati *et al.*, 1991; Legrand-Blain & Perret-Mirouse, 2000). On top of

91 Paleozoic formations, unconformable horizontal Mesozoic-Cenozoic formations are observed. The
92 oldest Mesozoic deposits are Early Cretaceous rocks in the Tindouf Basin (Gevin, 1960; Fabre, 2005).
93 In the eastern Taoudeni Basin (Tanezzrouft), the oldest Mesozoic deposits are possibly Late
94 Cretaceous (Fabre *et al.*, 1996) (Fig. 1). This hiatus of more than 100 Myr (from Late
95 Carboniferous/Permian to at least Early Cretaceous) differentiates the WAC from the central and
96 eastern Sahara domains where post-Variscan deposits can be as old as Triassic in central Sahara
97 (Busson, 1972; Boudjema, 1987).

98 The Tarfaya-Laayoune-Dakhla Basin (TLDB; Fig. 1b) is a NE-SW oriented basin which bounds
99 the Atlantic Ocean. This basin formed during the opening of the Central Atlantic Ocean, with an
100 estimated break-up in the Late Sinemurian (~190 Ma; Labails *et al.*, 2010). The basin is built on a 100-
101 km wide stretched crustal domain with a crust thickness that varies from 27 to 7 km oceanward
102 (Klingelhoefer *et al.*, 2009). The thick Mesozoic-Cenozoic infill reaches more than 10 km (AUXINI,
103 1969; Martinis & Visintin, 1966; Ratschiller, 1968; Ranke *et al.*, 1982; Fig. 1c) and represents a
104 reliable record of the large-scale changes, which occurred during that time. On top of Triassic clastic-
105 evaporitic deposits, the Middle-Late Jurassic witnesses the build-up of a large carbonate platform
106 that ended in the Neocomian (up to the Barremian). The margin was then buried under
107 unconformable km-scale continental clastic deposits before marine conditions resumed in Aptian-
108 Albian and continued during the Late Cenomanian-Turonian times. The early Paleogene environment
109 was still marine but characterized by shallower depths before becoming continental from the Eocene
110 onwards. Paleogene formations lie unconformably on the Early and Late Cretaceous in TLDB.
111 Neogene deposits are scarce, thin and usually continental.

112

113 **Sampling and methodology**

114 *Sampling*

115 The dataset presented here consists of 29 samples and allows us to present a ~1300 km E-W
116 LTT transect of the NWAC from the Atlantic passive margin to the Panafrican suture in the east. Our
117 new data adds two AFT data to the 11 existing AFT data in the western Reguibat Shield (Leprêtre *et*
118 *al.*, 2015), four new AFT and three new AHe datasets to the existing four AFT and one AHe datasets
119 (Leprêtre *et al.*, 2014) and eight new AFT and 6 new AHe datasets for the eastern Reguibat Shield
120 (Fig. 1b). For the reader's information, the complete dataset encompassing samples from Leprêtre *et*
121 *al.* (2014, 2015) are presented in Supplementary data (Tables S1, S2).

122 The Reguibat Shield was geographically divided into three regions on the basis of the LTT
123 results. With the exception of one AFT age (256 Ma from TEN1153 sample, in central Reguibat
124 Shield), AFT age ranges largely overlap between western and central domains (Fig. 2). Mean track
125 lengths (MTLs) are also comparable between these two domains whereas MTLs from the eastern
126 domain are shorter (Fig. 3). Western and central Reguibat Shield domains are differentiated based on
127 their AHe age ranges. AHe ages from western Reguibat Shield are younger than 127 Ma (only one
128 replicate is older) whereas they range from 38 to 191 Ma for central Reguibat Shield (4 of 11 AL10
129 replicates are out of the trend) with significantly older AHe ages at eU > 20 ppm. Compared to
130 central Reguibat Shield (AFT range: 139 to 256 Ma; AHe range: 38 to 269 Ma when excluding the two
131 anomalously old AL10 replicate; see Table 2), eastern Reguibat Shield yielded significantly older AFT
132 ages (237 to 497 Ma against 139 to 256 Ma for central Reguibat; Table 1; Fig. 2, 3) and shows a larger
133 scattering of the AHe data (32 to 384 Ma).

134

135 *Low-temperature thermochronology*

136 Samples were processed at the GEOPS laboratory (Université Paris-Sud, Orsay, France). AFT
137 dating was carried out using the external detector method (Gleadow & Duddy, 1981) for calculating
138 the central age (Galbraith & Laslett, 1993) using the Zeta calibration (Hurford & Green, 1983). Zeta
139 calibration was done with a CN5 glass dosimeter and Durango/Fish Canyon apatite standards

140 (Hurford, 1990; $\zeta = 368 \pm 10$ for RL). Neutron irradiation was carried out at Garching facility
141 (Germany). Spontaneous tracks were revealed by etching in 5M HNO₃ for 20 seconds at 20±1°C. The
142 size of the etch pit made between the track and polished apatite surface (Dpar) was measured and
143 used as a kinetic parameter for fission track annealing (Carlson *et al.*, 1999). Dpar measurements act
144 as a proxy for compositional and structural variations in apatite (Barbarand *et al.*, 2003). Horizontal
145 confined track-lengths were measured using a LEICA microscope with a x1000 magnification and a
146 digitizing tablet linked via a drawing tube to the microscope. AFT ages, lengths and Dpar
147 measurements are given in Table 1 and figures 2-4.

148 AHe analysis was carried out on euhedral inclusion-free apatite crystals with a minimum of
149 four replicates per sample. Crystal dimensions and geometry were measured along the three axes
150 and grains were placed into a platinum basket. Ejection factors and sphere equivalent radius were
151 determined using the Monte Carlo simulation from Ketcham *et al.* (2011). More details on He, U, Th
152 and Sm content determination can be found in Gautheron *et al.* (2013). The analysis was
153 calibrated using internal and external age standards (Durango: McDowell *et al.*, 2005; Limberg Tuff:
154 Kraml *et al.*, 2006). The error on the AHe age at 1 σ is estimated to be a maximum of 8% reflecting
155 uncertainty in the ejection factor (FT) correction and standard dispersion. The final He, U-Th-Sm
156 content and AHe age are reported in Table 2.

157 AHe closure temperature was defined after Dodson (1973) depending on apatite grain size,
158 the cooling rate and on He diffusion coefficient. It has been shown that a pure apatite crystal “free-
159 default crystals” yield closure temperature of *c.a.* 30-40°C depending on chemical content (Djimbi *et*
160 *al.*, 2015). For natural apatite, the closure temperature is tightly linked to the alpha-recoil damage
161 fraction (Shuster *et al.*, 2006; Shuster & Farley, 2009). This behavior has been incorporated into two
162 predictive models by Flowers *et al.* (2009) and Gautheron *et al.* (2009). These models consider that
163 recoil damage annealing follows kinetics similar to fission-tracks, after the results of Ketcham *et al.*
164 (2007). Different closure temperatures can be monitored through the relationship of AHe age vs.

165 efficient uranium (eU). The eU represents the amount of radioactive elements contributing to the
166 ^4He production and its amount controls the closure temperature for a given thermal history (Shuster
167 *et al.*, 2006). Thus, scattered AHe ages emphasize, at first order, differences in AHe closure
168 temperatures between replicates in the same sample. Moreover, the damage-annealing rates can be
169 influenced by the apatite chemistry (Gautheron *et al.*, 2013; Djimbi *et al.*, 2015). In particular,
170 Gautheron *et al.* (2013) demonstrated that complex thermal histories in slow moving geological
171 settings can greatly enhance the scattering in the data given the chemistry differences between
172 grains. Also, the ^4He apatite content can increase through implantation from rich eU neighbors
173 crystals in the rock (Spiegel *et al.*, 2009; Gautheron *et al.*, 2012) or for low eU apatite, this effect has
174 also been observed (Kendra *et al.*, 2013; Murray *et al.*, 2014; Janowski *et al.*, 2017). Helium
175 implantation produces an artificial aging trend for the more exposed apatite crystals. In addition, the
176 analysis of broken apatite crystals can add scattering to the data (Brown *et al.*, 2013).

177 *Thermal modeling*

178 Modeling procedure

179 Inverse thermal modeling was performed using the software QTQt (Gallagher, 2012) while
180 HeFTy (Ketcham, 2005) was used for forward modeling. We used the fission track annealing kinetics
181 of Ketcham *et al.* (2007) and the He-trapping/diffusion model of Flowers *et al.* (2009). The Flowers *et al.*
182 *et al.* (2009) radiation damage accumulation and annealing model is empirically calibrated and is not
183 well-representative of the physical processes of diffusion compared to the Gautheron *et al.* (2009)
184 model but it gives better predictions, mainly for low-eU apatite (< 20 ppm; majority of our samples,
185 see Table 2). QTQt works with a probabilistic Bayesian approach for inverse modeling. It samples
186 numerous thermal histories and from them builds a population of models selected according to the
187 degree of agreement between data and model—this is the burn-in phase. It then proceeds with
188 inverse modeling, which is called the post burn-in phase. For each phase, the user can choose the

189 number of iterations, depending on the complexity of its own data set. In QTQt, the fit between the
190 data and the model is defined by the Log Likelihood (LL; details are given in Gallagher, 2012).

191

192 Strategy for thermal modeling

193 The strategy for the thermal modeling of the LTT data relies on the geological context of the
194 study. Importantly for this study, we consider, following Burov (2011), that deformation of old
195 lithospheres (> 1Ga) is mostly controlled by the rheology of the lithosphere which is dependent on its
196 age. The Reguibat Shield is an old lithosphere (> 2 Ga; Potrel *et al.*, 1998; Lahondère *et al.*, 2001;
197 Peucat *et al.*, 2005; Schofield *et al.*, 2012; Bea *et al.*, 2013) and as such, its deformation will involve
198 the whole lithosphere with wavelengths > 500 km. We thus infer that samples separated from each
199 other by less than few hundred kilometers should behave coherently and share similar thermal
200 paths. Furthermore, it implies that stratigraphical unconformities located on the boundaries of the
201 Reguibat Shield can give precious information for the evolution of its basement since the latter is
202 rarely wider than 400 km (Fig. 1).

203 For eastern Reguibat Shield, two major stratigraphical constraints were used: (1)
204 unconformable Cambrian deposits on the NWAC basement (Trompette, 1973; Deynoux, 1980 for
205 Taoudeni Basin; Boote *et al.*, 1998 for Tindouf Basin); (2) unconformable poorly-dated upper
206 Cretaceous deposits on the eastern boundary of the Reguibat basement. We used a large
207 temperature box (20-180°C) for the 470-230 Ma interval as no constrain exists for this period. Firstly,
208 a general thermal path was modeled with inverse modeling for eastern Reguibat shield samples that
209 have both AFT and AH data (Fig. 6a-c, 7a; Fig. S2-7). By combining AFT and AHe datasets, we can
210 achieve a better resolution of the thermal history path. The important temperature/time (or (T,t))
211 nodes obtained in this first modeling were used as constraints for other eastern Reguibat Shield
212 samples where only AFT data were available (CH2 and DEG6, Fig. S2-3). Only final models are
213 presented in the results (Fig. 6a, 7a). Considering the old LTT ages of samples from eastern Reguibat

214 Shield ($> 237 \pm 21$ Ma), we only used the constraint that rocks were at surface during Cambrian. In
215 the course of thermal modeling, no stable solutions were obtained for samples GH20 and IG3.

216 For central Reguibat Shield only one meaningful stratigraphical constraint was used: Lower
217 Cretaceous deposits rest unconformably on the Paleozoic succession in the Tindouf Basin and directly
218 on the basement in the east of the TLDB (Fig. 1b). This Lower Cretaceous unconformity is distant
219 from the samples by less than 400 km. We suggest that it likely implies that even samples from the
220 interior of the Reguibat Shield were at or close to the surface at this time. We used here a two-step
221 approach for thermal modeling.

222 Firstly, we carried out a phase of forward modeling to explain the AHe age-eU positive
223 correlation (Fig. 5b, 8). In this phase, we consider the AHe data of all samples as these data should
224 behave coherently given that they are restricted to cratonic areas and the entire AHe dataset
225 samples a larger eU range than any one sample. Various thermal paths were tested to check their
226 AHe predictions and compare them to the measured data. Given that the AFT ages are all younger
227 than 250 Ma, the tested thermal history paths are chosen in order to display cooling initiated by the
228 Early Jurassic. Using the initial forward modeling step, we have identified the scenarios that best
229 explain the observed AHe data. These scenarios yield (T,t) constraints, *i.e.* compulsory nodes in the
230 (T,t) space through which the thermal path must go to fit the AHe age-eU relationship. Secondly, we
231 then performed inverse modeling that included these (T, t) constraints, so as to investigate the
232 degree of freedom left to fit the AFT data. The same stratigraphic constraint was used for all samples.
233 All detailed individual models are presented figures S8-15 and only the final thermal paths are
234 presented in figure 7b.

235 The two new samples from the western Reguibat Shield were modeled using the (T, t)
236 constraints determined in Leprêtre *et al.* (2015) (Fig. S16-17 and Text S1). One detailed thermal
237 modeling is presented in figure 6c and all thermal paths for the western Reguibat Shield are shown in
238 figure 7c.

239 Finally, considering the predictions made by the He-trapping/diffusion models (Flowers *et al.*,
240 2009; Gautheron *et al.*, 2009), we advocate that for a given thermal history path, single-grain AHe
241 ages are expected to display a correlation with eU. As a methodological consequence for our thermal
242 modeling, we removed the single-grain AHe ages that were outliers from the mean AHe age-eU
243 correlation, *i.e.* in our samples, being outliers by more than 50-100 Ma or a very different eU value
244 (*e.g.* Flowers and Kelley, 2011). Using these “outlier” replicates would impede the thermal modeling
245 as the model would attempt to fit out-of-trend data and lead to either no acceptable solutions being
246 found (in the case of HeFTy) or to a thermal model with bad fit for many replicates (*e.g.* QTQt, Fig.
247 S1). A clear assumption is made here that favors an acceptable goodness of fit for the majority of
248 replicates, which belong to a common AHe age-eU trend, instead of trying to explain all the
249 replicates resulting in a poor fit between predicted and observed data. Following this criteria, one
250 single-grain AHe age of nine was removed in sample CH1 and TL3 for being too far from the mean
251 AHe age-eU correlation (Fig. 5d, i; Table 2). Also, 3 of 11 replicates were removed in sample AL10 for
252 the same reason (Fig. S1).

253

254 **Results**

255 The new and published AFT and AHe ages presented for 29 samples give the first
256 comprehensive dataset across the whole Reguibat Shield. Based on the data location and their
257 thermal histories, the studied area has been divided into western, central and eastern domains.
258 Published data from the western and central Reguibat Shield (Leprêtre *et al.*, 2014; 2015) are only
259 briefly summarized, but the complete Reguibat dataset is presented together in Tables S1 and S2.

260 *LTT results*

261 The eastern domain shows the oldest and the most scattered AFT ages, ranging from $237 \pm$
262 21 to 497 ± 61 Ma (Table 1). MTLs are slightly shorter than in the other domains, between 11.2 ± 0.4

263 and $12 \pm 0.2 \mu\text{m}$ (Fig. 3). Track length distributions (TLDs) are largely unimodal and spread around the
264 mean (Fig. 4). Dpar measurements range from 1.7 ± 0.2 to $2.1 \pm 0.2 \mu\text{m}$. AHe ages corrected from
265 alpha ejection range from 32 ± 3 to 384 ± 31 Ma with eU contents that range from 2 to 32 ppm. No
266 clear trend in the AHe age vs. eU plot exists (Fig. 5a) and the very variable AHe ages for similar eU
267 contents suggest that process other than a variable diffusion coefficient. This process will be
268 discussed later.

269 In the central Reguibat Shield, new AFT ages range from 150 ± 8 to 202 ± 14 Ma (Table 1) and
270 are in agreement with published data (139 ± 9 to 256 ± 21 Ma; Leprêtre *et al.*, 2014). New MTLs
271 range from 11.4 ± 0.3 to $12.0 \pm 0.2 \mu\text{m}$ and are undistinguishable from the 11.9 ± 0.2 to $12.4 \pm 0.2 \mu\text{m}$
272 range for published data (Fig. 3, 4). Dpar measurements range from 1.6 ± 0.2 to $2.1 \pm 0.5 \mu\text{m}$. AHe
273 ages corrected from alpha ejection range from 38 ± 3 to 396 ± 32 Ma (Table 2) with eU content
274 ranging from 7 to 83 ppm. Overall, they are younger than AFT ages with the exception of some
275 replicates from samples AL10 and TGH3163. AHe age vs. eU plot shows a general positive correlation
276 (Fig. 5b).

277 In the western Reguibat Shield, the two new samples yielded AFT ages of 137 ± 12 Ma and
278 118 ± 10 Ma with no measurable confined lengths (Table 1). Published AFT ages range from 107 ± 8
279 to 175 ± 16 Ma, with mean track length (MTL) ranging from $11.8 \pm 0.2 \mu\text{m}$ to $12.5 \pm 0.2 \mu\text{m}$ (Leprêtre
280 *et al.*, 2015). Track length distributions (TLDs) are largely unimodal, slightly spread around the mean
281 with some complex shapes but for samples with few confined lengths (Fig. 3, 4). Dpar measurements
282 range from 1.5 ± 0.2 to $1.8 \pm 0.3 \mu\text{m}$. Overall, AFT ages are quite homogenous, with a mean around
283 130-140 Ma. All AFT ages are younger than the 190 Ma rifting (Labails *et al.*, 2010). AHe ages
284 corrected from the alpha-ejection range from 14 ± 1 Ma to 185 ± 15 Ma, with an eU content ranging
285 from 7 to 71 ppm. AHe age vs. eU plot shows positive correlations when samples are grouped by
286 region (Fig. 5c) and these AHe age-eU relationships reflect thermal histories with successive
287 reheating/cooling events (Leprêtre *et al.*, 2015). Leprêtre *et al.* (2015) demonstrated that AHe age

288 scattering within each data set could be explained by radiation damage effects with a secondary role
289 played by variations in apatite chemistry.

290

291 *Thermal modeling results*

292 For each domain of the Reguibat Shield, we present one representative thermal model with
293 all predicted vs. measured AFT and AHe data (Fig. 6). All individual models are presented in detail in
294 the supplementary data (Fig. S2-S17).. A synthesis with all the thermal paths is given in figure 7. The
295 models for western Reguibat Shield are highly dependent on the constraints determined by Leprêtre
296 *et al.* (2015) as neither AHe nor length data are available for the two new samples (Fig. 6g-h).

297 Sample GH3 illustrates the general shape of the thermal paths for the eastern Reguibat
298 Shield (Fig. 1b, 6a-c). Thermal paths obtained from the inverse modeling for 6 of the 8 samples of this
299 domain are presented in figure 7a. For the best constrained, double LTT dated samples (TL3, GH3,
300 CH1 and CH3), thermal paths show a major cooling episode during the Early Cretaceous. This cooling
301 is variable among samples. At the very end of the Jurassic, samples were generally at temperatures
302 higher than 60°C (except for TL3) and were not undergoing cooling. Results are similar for AFT-dated
303 samples CH2 and DEG6. Whereas the western and central domains suffered post-Early Cretaceous
304 reheating, samples from the eastern domain cooled by $30 \pm 10^\circ\text{C}$ and stayed at relatively low
305 temperatures up to the present-day.

306 For the central Reguibat Shield, the forward modeling with AHe datasets clearly favored the
307 scenario involving the occurrence of a Jurassic-Early Cretaceous cooling event followed by a low-
308 amplitude reheating step (Fig.8; Table S3). Five forward scenarios were tested: a small Middle
309 Jurassic-Lower Cretaceous cooling with stable thermal conditions during Late Cretaceous (HT1); a
310 large Jurassic-Early Cretaceous cooling ($> 40^\circ\text{C}$) bringing samples close to the surface (HT2 and HT3)
311 before reheating episode; a continuous slow cooling (HT4); a major cooling between Early and Late

312 Cretaceous (HT5). HT1, HT4 and HT5 all provide too young AHe ages compared to the HT2 and HT3.
313 This preliminary treatment confirms the necessity to set a constraint related to the Lower Cretaceous
314 unconformity in the Tindouf Basin and the TLDB. It is also in line with our consideration regarding the
315 wavelength of cratonic deformation at large wavelength. The inverse modeling was conducted using
316 the Lower Cretaceous unconformity and constraints deduced from the forward modeling. The latter
317 suppose that samples were (1) at temperatures higher than 80°C before Early-Middle Jurassic and (2)
318 reheated after the beginning of the Early Cretaceous by 20-40°C. We let the inverse modeling
319 determine the temperature before the Jurassic, between 0 and 200°C. Samples with double LTT
320 datings display similar thermal paths (Fig. 6d-f, 7b). A significant cooling event ($\Delta T > 40^\circ\text{C}$) is recorded
321 between the beginning of the Jurassic (220-190 Ma) with minimum temperatures reached in the
322 Early Cretaceous (150-140 Ma) ranging from 55 to 45°C. Samples underwent a small reheating event
323 (by 20-25°C) until the beginning of the Late Cretaceous (with the exception of a later and stronger
324 reheating for sample TEN1153). Afterwards, samples cooled down to present-day temperature.

325 The two samples from the western Reguibat Shield yield similar results than the other
326 samples (Fig. 6g-h, 7c). Their thermal path shows an important cooling from Early-Middle Jurassic to
327 Early Cretaceous, from temperatures higher than 100°C to 35-40°C. A reheating phase occurred until
328 the beginning of Late Cretaceous (between 100-80 Ma), reaching temperatures as high as 65-70°C. It
329 is followed by a rapid cooling event until early Cenozoic up to 35-40°C before a slow cooling until
330 present.

331

332 **Discussion**

333 *Interpretation of LTT data*

334 *AFT and AHe ages*

335 Data show a clear increase of AFT and AHe ages towards the east and both datasets also
336 display more scattering eastwards (Fig. 2). From the LTT data and our thermal modelings one can
337 clearly see that samples stayed in the Partial Retention Zone (PRZ)/Partial Annealing one (PAZ) for a
338 long time. This more or less protracted stay within the PRZ strongly impacts the distribution of AHe
339 ages with respect to the eU (Fig. 5). For example, the curved positive trend of the AHe age-eU plot in
340 figure 5b can be explained by low-eU apatites experiencing greater diffusive loss of He (causing
341 younger AHe ages) than high-eU apatites during a short time in the PRZ during Early Cretaceous (10-
342 30 Myrs at $T > 50-60^{\circ}\text{C}$; Fig. 7b). This short stay within the PRZ was sufficient to partially reset the low-
343 eU AHe ages in the case of the central Reguibat Shield. We consider for now that the best
344 explanation for anomalous replicates behavior (mostly showing older AHe than what is expected) lies
345 in process of implantation of He from minerals neighbouring apatite in the rock (Spiegel *et al.*, 2009).
346 Up to $>300\%$ ^4He excess has been estimated in most extreme cases by Gautheron *et al.* (2012).
347 Moreover, low-eU apatites are logically more sensitive to implantation than high-eU apatite and this
348 can dramatically distort the AHe ages (Janowski *et al.*, 2017). With this hypothesis, we propose that
349 implantation and a long residence in the PRZ might explain the larger dispersion of the AHe ages for
350 the eastern Reguibat Shield compared to the central Reguibat Shield. In the case of the western
351 Reguibat Shield, Leprêtre *et al.* (2015) demonstrated that the apatite crystal chemistry was
352 responsible for an enhanced scattering around a mean AHe age-eU trend (their Fig. 5-7). In addition
353 to eU and equivalent sphere radius, the influence of apatite composition may also explain some of
354 the scattering seen here given the range of Dpar measurements for the central and eastern Reguibat
355 Shield samples (Tables S1, S2; further discussion in Text S2; Fig. S18).

356 *The NWAC in the Mesozoic*

357 Our results show that the Reguibat Shield experienced significant cooling event between the
358 Early-Middle Jurassic and the Late Cretaceous. This cooling occurred between Early-Middle Jurassic
359 and Early Cretaceous for western and central Reguibat Shield whereas it happened later, by the end

360 of the Early Cretaceous, for the eastern Reguibat Shield. Elevated temperatures during the Early
361 Jurassic can have two origins: (1) a thermal perturbation, linked either to the emplacement of the
362 Central Atlantic Magmatic Province (CAMP, Verati *et al.*, 2007) or to thermal flux increase in
363 connection with rifting; (2) a burial under a sedimentary cover which has been removed only after
364 the break-up. Importantly, the CAMP rocks do not crop out within the Reguibat Shield (Marzoli *et al.*,
365 1999; Verati *et al.*, 2005). Basal heat flow might have been higher during CAMP magmatism and/or
366 rifting, but would not be anymore anomalous during Cretaceous (Fig. 7b-c). LTT data from borehole
367 samples in the cratonic Anti-Atlas domain, north of the Tindouf Basin (Sehrt, 2014) estimate an
368 average $40^{\circ}\text{C.km}^{-1}$ palaeogeotherm during the Early-Middle Jurassic/Early Cretaceous without
369 measurable changes afterward. We thus favor the hypothesis of burial of the Reguibat Shield by a
370 Paleozoic sedimentary cover. This cover was removed during Lower-Middle Jurassic/Lower
371 Cretaceous erosion in the western and central Reguibat Shield and fed the clastic deposits of the
372 TLDB during the Early Cretaceous. Similarly, the reheating in the western and central domains
373 between 150 and 100 Ma is interpreted as a re-burial of the samples as no large magmatic anomaly
374 is recorded (Matton & Jebrak, 2009). The timing and, to a lesser extent, the amplitude of the re-
375 burial differs slightly to that proposed in Leprêtre *et al.* (2014). This can be attributed to the
376 additional AHe datasets used for thermal modeling in the present study. The models differ in the
377 onset and duration of the heating after the Upper Jurassic/Lower Cretaceous transition for models of
378 the central Reguibat (Fig. 7b; Leprêtre *et al.*, 2014, their figure 5). Our present study refines the
379 Leprêtre *et al.* (2014) models and adds more consistency to them. The heating phase occurred from
380 the end of Early Cretaceous up to the beginning of Late Cretaceous (Fig. 7b) when the major
381 Cenomanian-Turonian flooding is recorded. Plus, the beginning of cooling occurred at the beginning
382 of the Late Cretaceous when the Africa-Europe convergence began. We assert that AHe datasets
383 have helped to better constrain the post-Jurassic evolution of central Reguibat Shield, in comparison
384 with our previous investigations using only AFT analysis.

385 Assuming a palaeogeotherm of $30\text{-}50^{\circ}\text{C.km}^{-1}$ during the cooling and reheating and using the duration
386 and amplitude of the thermal changes predicted by our thermal models, we estimated the
387 eroded/deposited rock thicknesses for each event. The ranges of Jurassic/Cretaceous erosion are
388 between 0.8-2.1 km and 1-1.6 km from western to eastern Reguibat Shield respectively. The
389 amplitude of re-burial reaches 0.4 to 1.7 km for the western and central domains, with no re-burial in
390 the eastern Reguibat Shield (Fig. 7a). During the re-burial, the southern TLDB record Albian-Turonian
391 thicknesses that can reach 1 km (AUXINI, 1969), which are compatible with our estimates. Moreover
392 this cover might have been even thicker given the subsequent Late Cretaceous erosion. In
393 comparison with western and central domains, the eastern Reguibat Shield shows a late cooling
394 event, mostly occurring at the Lower/Upper Cretaceous transition (Fig. 7a). Whether this cooling can
395 be linked to the one recognized in western and central domains is challenging; however, we believe
396 that cooling in the eastern domain represents another phenomenon. There is no significant time
397 lapse between the cooling phase recorded in the western and central Reguibat Shield. If all three
398 domains were cooled by the same process we would then expect the timing of cooling in the eastern
399 Reguibat Shield to be approximately the same as the west and central domains, which is not the
400 case. As there is a significantly delay before the eastern Reguibat Shield cools, this cooling could
401 better be related to the Austrian phase recognized in the Sahara platform (Boudjema, 1987),
402 occurring in Aptian-Albian times. The former N/S Panafrican faults separating the WAC from the
403 Tuareg Shield were reactivated as the northern Tuareg Shield underwent anticlockwise rotation
404 resulting from the opening of the South Atlantic Ocean. The cooling in the eastern Reguibat Shield
405 might stem from the large-scale tectonic reorganization at that time.

406 Few other studies have dealt with the evolution of cratonic domains on the NWAC. In the
407 Anti-Atlas north of the Tindouf Basin, Ruiz *et al.* (2011) and Oukassou *et al.* (2013) demonstrated
408 using LTT data that the northern tip of the craton also underwent uplift and erosion during
409 Jurassic/Early Cretaceous times before a reheating step. Further east (Ahnet-Reggane-Timimoun
410 basins), based on organic matter maturity, AFT and zircon fission-tracks from several wells, Logan &

411 Duddy (1998) proposed a general cooling from Triassic to Early Cretaceous. They also show that the
412 Variscan erosion is highly reduced in most of the area, in agreement with our results. Eastward, in
413 the central and eastern Sahara, the evolution becomes more diverse. In the Illizi Basin, LTT and
414 organic matter maturity were used by English *et al.* (2016) to support Cenozoic uplift undergone by
415 the Tuareg Shield. However, their borehole data are not able to resolve the Mesozoic history since
416 they found various likely scenarios for the Jurassic-Cretaceous period, with one scenario involving a
417 small cooling event in the Early Cretaceous. A limited number of LTT studies have been undertaken
418 on the Hoggar basement and they are focused on the Cenozoic exhumation without being able to
419 properly address the Mesozoic history given their poor confined length contents and the abundance
420 of Cenozoic AFT ages (Carpéna, 1988; Cavellec, 2006; Rougier, 2012; Rougier *et al.*, 2013).

421

422 **Evolution of the conjugate passive margins of the Central Atlantic Ocean**

423 Several lines of evidence testify to the existence of common processes on each side of the
424 northern Central Atlantic Ocean during Jurassic-Cretaceous times. We present them in the following
425 section.

426 *LTT record on the onshore eastern American passive margin*

427 Outcrops from the Appalachian orogen and surroundings basins have been used in numerous
428 LTT studies but have never been considered as a whole dataset (Crowley, 1991; Wang *et al.*, 1994;
429 Boettcher & Milliken, 1994; Roden-Tice *et al.*, 2000; Roden-Tice & Wintsch, 2002; Grist and Zentilli,
430 2003; Lorencak *et al.*, 2004; Spotila *et al.*, 2004; Roden-Tice & Tice, 2005; Taylor & Fitzgerald, 2011;
431 Roden-Tice *et al.*, 2012). We have collated all of the existing AFT data along eastern North America
432 (Fig. 9a,c). A clear division in AFT ages is observed with young AFT ages along a 600-km wide strip of
433 land parallel to the hinge line (*i.e.* the place where the continental crust begin to thin toward the
434 ocean; Fig. 1b, 9a). The “young” AFT datings range between *c.a.* 80-180 Ma, with the exception of

435 slightly older samples along the Nova Scotia segment in the north. AFT ages become progressively
436 older landward (up to 600 Ma, beyond 600-700 km off the hinge line). The spatial pattern of AFT age
437 is strikingly similar to the NWAC (Fig. 9b-c; after the data of Ghorbal *et al.*, 2008; Saddiqi *et al.*, 2009;
438 Ruiz *et al.*, 2011; Oukassou *et al.*, 2013; this study), with ages being younger (c.a. 100-220 Ma) from
439 the coast to 600 km. AFT-MTL plots are given for both margins (Fig. 9c-d) and show that there is no
440 relationship between the age of rifting and length datasets. This significant observation means that
441 for samples within the 600/700-km proximal land strip, the effects of the Lower Jurassic rifting (c.a.
442 190 Ma) are barely distinguishable. Both margins seem coherently affected by a more regional event.

443

444 *Along-strike variations of the passive margin stratigraphical record*

445 Passive margin sedimentary infills have been studied along both passive margins and can be
446 compared to identify the similarities in their evolution. For this comparison, we use the regional
447 studies of Jansa & Wiedmann (1982) for Northwest Africa, Grew & Sheridan (1988) and Miall (2008)
448 for eastern North America. In the following, we present only the stratigraphical records from Early-
449 Middle Jurassic to the end of Early Cretaceous.

450 From north to south along the eastern American passive margin, four segments have been
451 well-documented: Nova Scotia, the Georges Bank, the Baltimore canyon Trough and the Blake
452 plateau (Fig. 10). On the African counterpart, we will present the Essaouira, Tarfaya and Senegal
453 segments.

454 The Nova Scotia and Georges Bank basins and the Baltimore Canyon Trough are defined by
455 similar stratigraphical formations. The Early Jurassic witnessed the deposition of dolomite and
456 anhydrite layers. These unconformably overlie Triassic formations and gradually became clastic
457 deposits moving laterally and upward in the section. On top of the Early Jurassic rocks, a large
458 carbonate platform aggraded and prograded seaward although a clastic influx still occurred during
459 Middle- Late Jurassic. During Early Cretaceous, carbonate platforms were buried under a thick clastic

460 influx of coarse sandstones, which even bypassed the platform edge (Jansa & Wiedman, 1982; Wade
461 & MacLean, 1990). By the end of the Early Cretaceous, clastic sedimentation was still ongoing but
462 with a lower influx during the Aptian-Turonian interval when a major transgressive period occurred.
463 South of these three basins, the Blake Plateau has received little attention. Its Middle Jurassic
464 stratigraphy is less known but the Late Jurassic witnessed the formation of a mixed terrigenous-
465 carbonated platform and the build-up of a massive carbonate platform occurred during the Early
466 Cretaceous. The platform was drowned during the Late Cretaceous due to the high-stand sea-level
467 which brought carbonate facies up to the Appalachian range with the deposition of deep-marine
468 marls on the former carbonate platform (Poag & Valentine, 1988).

469 On the northwest African passive margin, Jansa & Wiedmann (1982) described very similar
470 successive facies. In the Essaouira Basin, middle-upper Liassic (Lower Jurassic) records the early post-
471 rift transgression with the deposition of dolomites and evaporites, subsequently covered during
472 lower-middle Dogger (Middle Jurassic) by clastics with features characteristic of a marine regression.
473 A stable carbonate platform was built afterwards up to the end of the Late Jurassic. Carbonate
474 deposition was interrupted by some clastic deposition before a last regression in Berriasian times.
475 The Lower Cretaceous formations buried the former platform under kilometer-thick clastics with
476 large prograding deltas until the Aptian. Marine conditions resumed during Aptian with carbonate
477 deposition. From the Cenomanian-Turonian onwards, deeper marine conditions prevailed with
478 outer-shelf to slope type deposit. In the TLDB, the sedimentary record is similar to that in the
479 Essaouira Basin. Finally, in the southern segment of the Senegal Basin, a large carbonate platform
480 formed during the Middle-Late Jurassic to the end of Early Cretaceous. In contrast to the northern
481 segments, deposition of the carbonate platform was not interrupted and small volumes of clastic
482 sediments deposited in the Senegal Basin (Brownfield & Charpentier, 2003). A carbonate platform
483 even prevailed until the Late Cretaceous in the southern part of the basin.

484 The overall stratigraphical record on both sides of the Central Atlantic Ocean is strikingly
485 similar for the considered period. It becomes increasingly different afterwards in the Late Cretaceous
486 (Jansa & Wiedmann, 1982) during the convergence climax of Africa and Europe. For the whole
487 margin, the Jurassic witnessed the build-up of an almost continuous carbonate platform, which
488 ended in the beginning of the Early Cretaceous for the north Central Atlantic Ocean whereas this
489 build-up persisted until the Late Cretaceous for the southern segments of the margin. Given the LTT
490 record for both sides of the northern Central Atlantic Ocean described previously, we consider that
491 this abundant clastic feeding of the margins during the Neocomian must be related to a common
492 process which will be discussed in the next section.

493 *Evolution of the Central Atlantic Ocean*

494 The Central Atlantic Ocean underwent break-up during the Sinemurian (~190 Ma; Labails *et*
495 *al.*, 2010). During rifting and the early post-rift stage, a shared stratigraphical record is observed
496 predictably on both sides of the ocean (Jansa & Wiedmann, 1982; Fig. 10). The spreading rate of the
497 young Atlantic has been estimated by various authors (Cogné & Humler, 2006; Schettino & Turco,
498 2009; Labails *et al.*, 2010; Kneller *et al.*, 2012) for the Jurassic period. We present in figure 11 a
499 compilation of these rates. Even if slight differences exist between the different models, all authors
500 agree with a significant increase of this rate during Middle and Late Jurassic before a dramatic
501 decrease in the Early Cretaceous.

502 One must remember that LTT studies only give the simplest thermal paths between
503 constraint points that can reproduce the data. As such, the Jurassic-Early Cretaceous cooling we
504 obtained could alternate between discrete phases of accelerations and decelerations of the cooling
505 rate from the Early-Middle Jurassic to the Early Cretaceous. Considering the regression and clastic
506 burial of the Jurassic carbonate platforms, we think that an acceleration of the cooling rate would
507 have occurred during the Late Jurassic/Early Cretaceous because of enhanced exhumation. This
508 process can also be suggested for the symmetrical clastic feeding on the conjugate American passive

509 margin. Indeed, LTT studies on eastern North America suggest that a significant cooling occurred
510 over large areas during the Middle-Late Late Jurassic to the Early Cretaceous (Fig. 12a-c). This cooling
511 event is partially hidden in the northern Appalachian domain (central transect, the portion close to
512 the Atlantic Ocean in figure 9) where, a strong Early-Late Cretaceous cooling event is attributed to
513 the passage over/close to the Great Meteor hotspot (Taylor & Fitzgerald, 2011), which could have
514 disrupted the record of the earliest cooling phase (Fig. 12d).

515 Valid explanations for this Jurassic-Lower Cretaceous uplift must consider the following: (1)
516 the uplift event affected the onshore domains of either side of the conjugate passive margins and
517 over a longer wavelength than it is typically the case usually for other passive margins settings (up to
518 600 km landward compared to less than 200-300 km; see Gallagher *et al.*, 1998); (2) in spite of a
519 shared spreading history (Labails *et al.*, 2010), the Central Atlantic Ocean behaved differently at that
520 time and was split into a northern domain, whose margins were uplifted and a southern domain,
521 which experienced the continuous build-up of carbonate platforms (Fig. 10); (3) it must be followed
522 by a significant burial stage during the Early Cretaceous on the western and central Reguibat Shield,
523 with decreasing intensity landward. This burial is not evidenced on the American conjugate margin
524 and thermal stability has been retained after these changes (*e.g.* Taylor & Fitzgerald, 2011, their fig.
525 8; Roden-Tice *et al.*, 2012, their fig. 6-7).

526 The exhumation recorded on both margins peaked during the post-rift phase, interrupting
527 the classical subsidence post-rift phase, associated with the carbonated platform build-up. It is
528 difficult to argue that early post-rift geomorphological models like scarp retreat or pinned-divide
529 (Gallagher *et al.*, 1998) could be responsible for the distribution of the AFT ages and the evolution of
530 the margin. The NW African passive margin is characterized by a low-elevation profile which does not
531 seem to indicate any erosion retreat and that these rift-related processes usually exert themselves
532 on more restricted geographical scales (< 300 km inland). Moreover, huge erosion on the coastal
533 plain (and commonly ONLY studied for high-elevation passive margins) is classically explained by

534 primary controls such as the geometry of the rifting and the flexural rebound (see Bishop, 2007 and
535 Green *et al.*, 2013 for contrasted reviews). In our studied case, the asymmetrical mechanism of
536 rifting and the different crust-lithosphere geometries of the conjugate margins do not argue for both
537 margins to behave in such a similar way (Maillard *et al.*, 2006; Labails *et al.*, 2009). We also discard an
538 explanation involving regional compression to account for these results in the western and central
539 domains of the Reguibat Shield and the American conjugate passive margin. Bertotti & Gouiza (2012)
540 proposed this tectonic hypothesis for northern Morocco over the Late Jurassic/Early Cretaceous.
541 However, their arguments are based on limited structural evidence that is focused on their study
542 area. These features could also be explained as being halokinesis features (*e.g.* Saura *et al.*, 2014).
543 Additionally, pre-Late Cretaceous compressional features have never been described on the
544 Moroccan-Mauritanian passive margin during this period, before the onset of Africa-Europe
545 convergence (Rosenbaum *et al.*, 2002).

546 We propose a hypothesis that involves mantle-related dynamic processes to account for the
547 symmetrical uplifts on both sides of the northern Central Atlantic. The geographical extension of the
548 eroded area points to a large-scale process, which could be attributed to ascending hot mantle
549 material below the northern Central Atlantic Ocean. During Late Jurassic-Early Cretaceous,
550 magmatism is absent across both margins (see the review by Matton & Jebrak, 2009). Scarce basic
551 magmatic outcrops exist in northern Morocco (Frizon de Lamotte *et al.*, 2008) and in North America
552 (McHone & Butler, 1984) from this period. Their absence over most of the NWAC can be explained by
553 lack of structural pathways that allow the magma to pierce through the cratonic domain of the
554 Reguibat Shield. Spreading of a large shallow plume head below the northern Central Atlantic Ocean
555 lithosphere is thus not discarded but it would have to have impacted the base of the lithosphere at a
556 lower temperature than typical plume heads or at great sub-lithospheric depths, which therefore
557 prevent the development of a large volume of magmatism. Such a large hot mantle would have had
558 wide reaching effects at this time and would have impacted Northwest Africa and eastern North
559 America (this study), and even Iberia (*e.g.* Grobe *et al.*, 2014). The timing of the mantle plume is

560 concomitant with the second phase of the rifting between Iberia and Newfoundland (Tucholke *et al.*,
561 2007). The delay between the increase in Middle-Upper Jurassic spreading rates in the Central
562 Atlantic Ocean and the Lower Cretaceous clastic influx to the margins (Fig. 10, 11) is consistent with
563 the lag time for the thermal mantle anomaly to reach the surrounding continents and create uplift.
564 On a smaller scale, such a mechanism, as proposed here, could be similar to the “hot pulses” linked
565 to the Icelandic plume that spread out radially beneath the lithosphere as proposed by Hartley *et al.*
566 (2011) to explain various Cenozoic uplifts in this area of North Atlantic Ocean. In our case, the more
567 important Mesozoic uplift-burial cycle affecting Northwest Africa is interpreted as being a result of
568 NW Africa residing closest to an underlying mantle thermal anomaly compared to the conjugate
569 margin. This has resulted in a stronger dynamic uplift effect which triggered episodes of erosion and
570 burial that are able to be recorded by LTT methods. After the “dynamic pulse” that pushed upward
571 the NWAC, its decrease led consequently to an opposite trend in the western and central Reguibat
572 domains that allowed the re-burial of the margin in the extent revealed by our study, fading
573 eastward within the craton. A potential contribution of eroding material from the eastern Reguibat
574 Shield to this burial may be possible. Nevertheless, we are not able to properly evaluate this
575 contribution since no sedimentary remnants are preserved within the Reguibat Shield nowadays.

576

577 **Conclusion**

578 This LTT study evidenced a Lower-Middle Jurassic to Upper Cretaceous kilometric erosion
579 event that occurred in the previously presumed to be stable Northwest Africa. This result has major
580 consequences for the Reguibat Shield and Northwest Africa and is probably related to the Central
581 Atlantic expansion.

582 Along a roughly E-W ~1300 km transect of the Reguibat Shield, we show that kilometer-scale
583 erosion occurred from Early-Middle Jurassic to the Early Cretaceous for the western and central

584 domains. The eastern domain of the Reguibat Shield also underwent an erosional event but it
585 occurred later in the Early Cretaceous. The erosion of central and western domains was followed by
586 subsequent reheating/burial with decreasing intensity landward, before final cooling from Late
587 Cretaceous to present-day in western and central Reguibat Shield domains. For eastern Reguibat
588 Shield domain, the brief pulse of erosion can be identified at the Lower-Upper Cretaceous transition
589 and we may tentatively relate it to the Austrian unconformity.

590 These results have important implications when placed in the wider context of the
591 geodynamic setting of the Central Atlantic Ocean evolution. We demonstrate a similar pattern of
592 erosion occurring on the conjugate passive margin of eastern North America during the same period.
593 This long wavelength uplift event only affected the northern part of the continents surrounding the
594 young ocean and has an extent compatible with transient large scale mantle processes. A low-
595 temperature or deeply located sub-lithospheric mantle plume head responsible for this uplift is
596 concomitant with the second and last phase of rifting in the southern North Atlantic Ocean and could
597 have played a significant role in triggering its oceanic opening.

598

599 **Acknowledgements**

600 We thank Eric Douville for accessing the ICP-MS (LSCE, Gif-sur-Yvette) and Louise Bordier for the U-Th
601 measurements. This work has been supported by the Académie Hassan II des Sciences, Casablanca,
602 Morocco. We acknowledged P.F. Green and an anonymous reviewer for the remarks and comments
603 that greatly helped clarifying and precisising numerous points in the present manuscript.

604

605

606 **References**

- 607 Armitage, J.J., Jaupart, C., Fourel, L. & Allen, P.A. 2013. The instability of continental passive margins
608 and its effect on continental topography and heat flow. *Journal of Geophysical Research: Solid Earth*,
609 **118**, 1817-1836, doi: 10.1002/jgrb.50097.
- 610 AUXINI 1969. Correlación estratigrafica de los sondeos perforados en el Sahara Español. *Boletín*
611 *Geológico y Minero*, **83**, 235–251.
- 612 Barbarand, J., Carter, A., Wood, I. & Hurford, T. 2003. Compositional and structural control of fission-
613 track annealing in apatite. *Chemical Geology*, **198**, 107-137, doi: 10.1016/S0009-2541(02)00424-2.
- 614 Bea, F., Montero, P., Haissen, F. & El Archi, A. 2013. 2.46 Ga kalsilite and nepheline syenites from the
615 Awsard pluton, Reguibat Rise of the West African Craton, Morocco. Generation of extremely K-rich
616 magmas at the Archean–Proterozoic transition, *Precambrian Research*, **224**, 242-254, doi:
617 10.1016/j.precamres.2012.09.024.
- 618 Bertotti, G. and Gouiza, M. 2012. Post-rift vertical movements and horizontal deformations in the
619 eastern margin of the Central Atlantic: middle Jurassic to Early Cretaceous evolution of Morocco.
620 *International Journal of Earth Sciences*, **101**, 2151–65, doi: 10.1007/s00531-012-0773-4.
- 621 Bertrand-Sarfati, J., Moussine-Pouchkine, A., Affaton, P., Trompette, R. & Bellion, Y. 1991. Cover
622 sequences of the West African Craton. In: Dallmeyer, R.D. & Lécorché, J.P. (eds) *The West African*
623 *Orogens and Circum-Atlantic Correlatives*, Springer-Verlag, IGCP-Project, **223**, 65-82.
- 624 Boettcher, S.S. and Milliken, K.L., 1994. Mesozoic-Cenozoic unroofing of the Southern Appalachian
625 Basin: Apatite fission track evidence from Middle Pennsylvanian sandstones. *Journal of Geology*, **102**,
626 655- 663.

627 Boote, D.R.D, Clark-Lowes, D.D. & Traut, M.W. 1998. Paleozoic petroleum systems of North Africa. *In:*
628 MacGregor, D.S., Moody, R.T.J. & Clark-Lowes, D.D. (eds) *Petroleum Geology of North Africa*.
629 Geological Society, London, Special Publications, **132**). , 7-68, doi: 10.1144/GSL.SP.1998.132.01.02

630 Boudjema, A. 1987. *Evolution structurale du bassin pétrolier "triasique" du Sahara nord oriental*
631 *(Algerie)*. PhD thesis, Université Paris Sud XI, France.

632 Brown, R.W., Beucher, R., Roper, S., Persano, C., Stuart, F. & Fitzgerald, P. 2013. Natural age
633 dispersion arising from the analysis of broken crystals. Part I: Theoretical basis and implications for
634 the apatite (U–Th)/He thermochronometer. *Geochimica et Cosmochimica Acta*, **122**, 478-497, doi:
635 10.1016/j.gca.2013.05.041.

636 Brownfield, M.E. and Charpentier, R.R., 2003. Assessment of the undiscovered oil and gas of the
637 Senegal Province, Mauritania, Senegal, The Gambia, and Guinea-Bissau, Northwest Africa, United
638 States Geological Survey Bulletin, 25p.

639 Burkhard, M., Caritg, S., Helg, U., Robert-Charrue, C. & Soulaïmani, A. 2006. Tectonics of the Anti-
640 Atlas of Morocco. *Comptes Rendus Géoscience*, **338** (1-2), 11-24.

641 Busson, G., 1972. *Principes, méthodes et résultats d'une étude stratigraphique du mésozoïque*
642 *saharien*. Mémoires du Muséum d'Histoire Naturelle, Nouvelle Series, Série C, Sciences de la Terre,
643 **26**, 441p.

644 Burov, E.B. 2011. Rheology and strength of the lithosphere. *Marine and Petroleum Geology*, **28**,
645 1402-1443, doi:10.1016/j.marpetgeo.2011.05.008.

646 Carlson, W.D., Donelick, R.A. & Ketcham, R.A. 1999. Variability of apatite fission-track annealing
647 kinetics: I. Experimental results. *American Mineralogist*, **84**, 1213-1223, doi: 10.2138/am-1999-0901.

648 Carpéna, J., Kienast, J., Ouzegane, K., & Jehanno, C. 1988. Evidence of the contrasted fission-track
649 clock behavior of the apatites from In Ouzzal carbonatites (northwest Hoggar): The low-temperature

650 thermal history of an Archean basement. *Geological Society of America Bulletin*, **100**, 1237-1243,
651 doi : 10.1130/0016-7606(1988)100.

652 Cavellec, S., 2006. *Evolution diagénétique du bassin de Tim Mersoï et conséquences pour la génèse des*
653 *minéralisations uranifères dans les formations carbonifères du Guezouman et du Tarat (district Arlit-*
654 *Akokan, Niger)*. PhD thesis, Université Paris Sud XI.

655 Cogné, J.-P. and Humler, E., 2006. Trends and rythms in global seafloor generation rate.
656 *Geochemistry, Geophysics, Geosystems*, **7**(3), doi:10.1029/2005GC001148.

657 Cogné, N., Gallagher, K., Cobbold, P.R., Riccomini, C. & Gautheron, C. 2012. Post-breakup tectonics in
658 southeast Brazil from thermochronological data and combined inverse-forward thermal history
659 modeling. *Journal of Geophysical Research*, **117**, B11413, doi:10.1029/2012JB009340.

660 Crowley, K.D. 1991. Thermal History of Michigan Basin and Southern Canadian Shield from apatite
661 fission track analysis. *Journal of Geophysical Research: Solid Earth*, **96**(B1), 697-711, doi:
662 10.1029/90JB02174.

663 Deynoux, M. 1980. *Les formations glaciaires du Précambrien terminal et de la fin de l'Ordovicien en*
664 *Afrique de l'Ouest. Deux exemples de glaciation d'inlandsis sur une plateforme stable*. Travaux du
665 Laboratoire de Sciences de la Terre, St Jérôme, Marseille.

666 Djimbi, D.M., Gautheron, C., Roques, J., Tassan-Got, L., Gerin, C. & Simoni, E., 2015. Impact of apatite
667 chemical composition on (U-Th)/He thermochronometry: An atomistic point of view. *Geochimica et*
668 *Cosmochimica Acta*, **167**, 162-176, doi:10.1016/j.gca.2015.06.017.

669 Dodson, M. H. (1973), Closure temperature in cooling geochronological and petrological systems,
670 *Contributions to Mineralogy and Petrology*, **40**, 259-274, doi: 10.1007/BF00373790.

671 English, K., Redfern, J., Bertotti, G., English, J.M. & Cherif, R.Y., 2016. Intraplate uplift: new
672 constraints on the Hoggar dome from the Illizi basin (Algeria). *Basin Research*, doi:
673 10.1111/bre.12182.

674 Fabre, J., Arnaud-Vanneau, A., Belhadj, Z. & Monod, T. 1996. Evolution des terrains méso-
675 cénozoïques d'une marge à l'autre du craton ouest africain, entre le Tanezrouft (Algérie) et l'Adrar de
676 Mauritanie. In : Bitam, L. & Fabre, J. (eds) *Géodynamique du craton ouest africain central et oriental :
677 héritage et évolution post-panafricains*. Service géologique de l'Algérie, Boumerdès, Mémoires du
678 Service Géologique de l'Algérie, **8**, 187-229.

679 Fabre, J. 2005. *Géologie du Sahara occidental et central*. Musée Royal de l'Afrique Central, Tervuren,
680 African Geoscience Collection, **108**.

681 Flowers, R.M., Ketcham, R.A., Shuster, D. & Farley, K.A. 2009. Apatite (U–Th)/He thermochronology
682 using a radiation damage accumulation and annealing model. *Geochimica et Cosmochimica Acta*, **73**,
683 2347–2365, doi:10.1016/j.gca.2009.01.015.

684 Flowers, R.M. & Kelley, S.A. 2011. Interpreting data dispersion and “inverted” dates in apatite (U–
685 Th)/He and fission-track datasets: An example from the US Midcontinent. *Geochimica et
686 Cosmochimica Acta*, **75**, 5169-5186, doi:10.1016/j.gca.2011.06.016.

687 Frizon de Lamotte, D., Zizi, M., Missenard, Y., Hafid, M., El Azzouzi, M., Maury, R.C., Charrière, A.,
688 Taki, Z., Benammi, M. & Michard, A., 2008. The Atlas system. In: Michard, A., Chalouan, A. and
689 Saddiqi, O. (eds) *Continental Evolution: The Geology of Morocco. Structure, Stratigraphy, and
690 Tectonics of the Africa-Atlantic-Mediterranean Triple Junction*, Springer Verlag, Lecture Notes in Earth
691 Sciences, **116**, 133-202 doi: 10.1007/978-3-540-77076-3_4.

692 Frizon de Lamotte, D., Tavakoli-Shirazi, S., Leturmy, P., Averbuch, O., Mouchot, N., Raulin, C.,
693 Leparmentier, F., Blanpied, C. & Ringenbach, J.-C. 2013. Evidence for Late Devonian vertical

694 movements and extensional deformation in Northern Africa and Arabia – Integration in the
695 geodynamics of the Devonian world. *Tectonics*, **32**(2), 107-122, doi: 10.1002/tect.20007

696 Furon, R. 1956. Sahara, Afrique occidentale française et portugaise. Lexique stratigraphique
697 international. Editions du CNRS, Paris, **IV** (2), Afrique.

698 Galbraith, R. F. & Laslett, G.M. 1993. Statistical models for mixed fission track ages. *Nuclear tracks*
699 *and radiation measurements*, **21**, 459-480, doi:10.1016/1359-0189(93)90185-C.

700 Gallagher, K., Brown, R.W., & Johnson, C. 1998. Fission track analysis and its applications to
701 geological problems. *Annual Review of Earth and Planetary Sciences*, **26** (5), 9-72, doi:
702 10.1146/annurev.earth.26.1.519.

703 Gallagher, K. 2012. Transdimensional inverse thermal history modeling for quantitative
704 thermochronology. *Journal of Geophysical Research*, **117**, B02408, doi:10.1029/2011JB008825.

705 Gautheron, C., Tassan-got, L., Barbarand, J. & Pagel, M. 2009. Effect of alpha-damage annealing on
706 apatite (U–Th)/He thermochronology. *Chemical Geology*, **266**, 166–179,
707 doi:10.1016/j.chemgeo.2009.06.001.

708 Gautheron, C., Tassan-got, L., Ketcham, R.A. & Dobson, K.J. 2012. Accounting for long alpha-particle
709 stopping distances in (U–Th–Sm)/He geochronology: 3D modeling of diffusion, zoning, implantation,
710 and abrasion. *Geochimica et Cosmochimica Acta*, **96**, 44-56, doi:10.1016/j.gca.2012.08.016.

711 Gautheron, C., Barbarand, J., Ketcham, R.A., Tassan-Got, L., van der Beek, P., Pagel, M., Pinna-Jamme,
712 R., Couffignal, F. & Fialin, M., 2013. Chemical influence on α -recoil damage annealing in apatite:
713 Implications for (U–Th)/He dating. *Chemical Geology*, **351**, 257-267, doi:
714 10.1016/j.chemgeo.2013.05.027.

715 Gevin, P. 1960. *Etudes et reconnaissances géologiques sur l'axe cristallin Yetti-Eglab et ses bordures*
716 *sédimentaires (1ere partie: bordures sédimentaires)*. Service de la carte géologique de l'Algérie **23**.

717 Ghorbal, B., Bertotti, G., Foeken, J. & Andriessen, P. 2008. Unexpected Jurassic to Neogene vertical
718 movements in “stable” parts of NW Africa revealed by low temperature geochronology. *Terra Nova*,
719 **20** (5), 355-363, doi:10.1111/j.1365-3121.2008.00828.x.

720 Gleadow, A.J.W. & Duddy, I.R. 1981. A natural long-term track annealing experiment for apatite.
721 *Nuclear Tracks*, **5**, 169–174, doi:10.1016/0191-278X(81)90039-1.

722 Green, P.F. & Duddy, I.R. 2010. Synchronous exhumation events around the Arctic including
723 examples from Barents Sea and Alaska North Slope. *In: Vining, B.A. & Pickering, S.C. (eds) Petroleum*
724 *Geology: From Mature Basins to Now Frontiers – Proceedings of the 7th Petroleum Geology*
725 *Conference*, Geological Society, London, Petroleum Geology Conference series, 7, 633-644, doi:
726 10.1144/0070633.

727 Green, P.F., Lidmar-Bergström, K., Japsen, P., Bonow, J.M. & Chalmers, J.A. 2013. Stratigraphic
728 landscape analysis, thermochronology and the episodic development of elevated, passive continental
729 margins. *Geological Survey of Denmark and Greenland Bulletin*, **30**, 150p.

730 Grow, J.A. & Sheridan, R.E., 1988. U.S. Atlantic continental margin: a typical Atlantic-type or passive
731 continental margin. *In: Sheridan, R.E. & Grow, J.A. (eds) The Atlantic Continental Margin*, Geological
732 Society of America, Geology of North America, Boulder, Colorado, **1-2**, 1-7.

733 Grist, A.M. & Zentilli, M. 2003. Post-Paleocene cooling in the southern Canadian Atlantic region:
734 evidence from apatite fission track models. *Canadian Journal of Earth Sciences*, **40** (9), 1279-1297,
735 doi: 10.1139/e03- 045.

736 Grobe, R.W., Alvarez-Marrón, J., Glasmacher, U.A. & Stuart, F.M. 2014. Mesozoic exhumation history
737 and paleolandscape of the Iberian Massif in eastern Galicia from apatite fission-track and (U+Th)/He
738 data. *International Journal of Earth Sciences*, **103** (2), 539-561, doi: 10.1007/s00531-013-0976-3.

739 Haddoum, H., Guiraud, R. & Moussine-Pouchkine, A. 2001. Hercynian compressional deformations of
740 the Ahnet–Mouydir Basin, Algerian Saharan Platform: far-field stress effects of the Late Paleozoic
741 orogeny. *Terra Nova*, **13**, 220–226, doi: 10.1046/j.1365-3121.2001.00344.x.

742 Hartley, R.A., Roberts, G.G., White, N. & Richardson, C. 2011. Transient convective uplift of an ancient
743 buried landscape. *Nature Geoscience*, **4**, 562-565, doi: 10.1038/NGEO1191

744 Holford, S.P., Green, P.F., Duddy, I.R., Turner, J.P., Hillis, R.R. &Stoker, M.S. 2009. Regional intraplate
745 exhumation episodes related to plate-boundary deformation. *Geological Society of America Bulletin*,
746 **121** (11–12), 1611–1628, doi:10.1130/B26481.1.

747 Huisman, R. & Beaumont, C. 2011. Depth-dependent extension, two-stage breakup and cratonic
748 underplating at rifted margins. *Nature*, **473**, 74-79, doi:10.1038/nature09988.

749 Hurford, A. J. 1990. Standardization of fission track dating calibration: recommendation by the Fission
750 Track Working Group of the I.U.G.S. Subcommittee on Geochronology. *Chemical Geology: Isotope*
751 *Geoscience section*, **80** (2), 171-178, doi:10.1016/0168-9622(90)90025-8.

752 Hurford, A.J., and Green, P.F. & Green, P.F. 1983. The zeta age calibration of fission-track dating,
753 *Chemical Geology*, **41**, 285-317, doi:10.1016/S0009-2541(83)80026-6.

754 Janowski, M., Loget, N., Gautheron, C., Barbarand, J., Bellahsen, N., Van den Driessche, J., Babault, J.
755 & Meyer, B. 2017. Neogene exhumation and relief evolution in the eastern Betics (SE Spain): insights
756 from the Sierra de Gador. *Terra Nova* in press, doi:10.1111/ter.12252..

757 Jansa, L.F. & Wiedmann, J. 1982. Mesozoic-Cenozoic Development of the Eastern North American
758 and Northwest African continental margins: a comparison. *In: von Rad, U. et al. (eds) Geology of the*
759 *Northwest African Continental Margin*, Springer-Verlag, Berlin Heidelberg, 215-269.

760 Japsen, P., Bonow, J.M., Green, P.F., Chalmers, J.A. & Lidmar-Bergström, K. 2006. Elevated, passive
761 continental margins: long-term highs or Neogene uplifts? New evidence from West Greenland. *Earth
762 and Planetary Science Letters*, **248**, 315–324, doi:10.1016/j.epsl.2006.05.036.

763 Japsen, P., Chalmers, J.A., Green, P.F. & Bonow, J.M., 2012. Elevated, passive continental margins:
764 Not rift shoulders, but expressions of episodic, post-rift burial and exhumation. *Global and Planetary
765 Change*, **90-91**, 73-86, doi: 10.1016/j.gloplacha.2011.05.004.

766 Ketcham, R.A. 2005. Forward and Inverse modeling of Low-temperature Thermochronometry data.
767 *Reviews in Mineralogy & Geochemistry*, **58** (1), 275-314, doi: 10.2138/rmg.2005.58.11.

768 Ketcham, R. A., Carter, A., Donelick, R. A., Barbarand, J. & Hurford, A. J. 2007. Improved modeling of
769 fission-track annealing in apatite. *American Mineralogist*, **92**, 799–810, doi: 10.2138/am.2007.2281.

770 Ketcham, R. A., Gautheron, C. & Tassan-Got, L. 2011. Accounting for long alpha-particle stopping
771 distances in (U–Th–Sm)/He geochronology: refinement of the baseline case. *Geochimica et
772 Cosmochimica Acta*, **75**, 7779–7791, doi:10.1016/j.gca.2011.10.011.

773 Klingelhoefer, F., Labails, C., Cosquer, E., Rouzo, S., Géli, L., Aslanian, D., Olivet, J.L., Sahabi, M.,
774 Nouzé, H. & Unternehr, P., 2009. Deep crustal structure of the SWMorrocan margin from wideangle
775 and reflection seismic data (The DAKHLA experiment). *Tectonophysics*, **468**, 63–82,
776 doi:10.1016/j.tecto.2008.07.022.

777 Kneller, E.A., Johnson, C.A., Karner, G.D., Einhorn, J. & Queffelec, T.A. 2012. Inverse methods for
778 modeling non-rigid plate kinematics: Application to Mesozoic plate reconstructions of the Central
779 Atlantic. *Computers & Geosciences*, **49**, 217-230, doi:10.1016/j.cageo.2012.06.019.

780 Kraml, M., Pik, R., Rahn, M., Selbekk, R., Carignan, J. & Keller, J. 2006. A new multi-mineral age
781 reference material for $^{40}\text{Ar}/^{39}\text{Ar}$, (U–Th)/He and fission track dating methods: the Limberg t3 Tuff.
782 *Geostandards and Geoanalytical Research*, **30**, 73–86, doi: 10.1111/j.1751-908X.2006.tb00914.x.

783 Labails, C., Olivet, J.L. & The Dakhla study group, 2009. Crustal structure of the SW Moroccan margin
784 from wide-angle and reflection seismic data (the Dakhla experiment). Part B — The tectonic heritage.
785 *Tectonophysics*, **468**, 83-97, doi:10.1016/j.tecto.2008.08.028.

786 Labails, C., Olivet, J.L., Aslanian, D. & Roest, W.R. 2010. An alternative early opening scenario for the
787 Central Atlantic Ocean. *Earth and Planetary Science Letters*, **297**, 355-368,
788 doi:10.1016/j.epsl.2010.06.024.

789 Lahondère, D., Thiéblemont, D., Goujou, J.C., Roger, J., Moussine-Pouchkine, A., Le Métour, J.,
790 Cocherie, A. & Guerrot, C. 2003. Notice explicative des cartes géologiques et géologiques à 1:200 000
791 et 1:500 000 du Nord de la Mauritanie, Direction des Mines et de la Géologie, Ministère des Mines et
792 de l'Industrie, Nouakchott, Mauritanie, **1**.

793 Lefranc, J.P. & Guiraud, R. 1990. The Continental Intercalaire of northwestern Sahara and its
794 equivalents in the neighbouring regions. *Journal of African Earth Science*, **10** (1-2), 27-77,
795 doi:10.1016/0899-5362(90)90047-I.

796 Legrand-Blain, M. & Perret-Mirouse, M.F. 2000. *Brachiopodes et Conodontes carbonifères du bassin*
797 *de Taoudeni (Mali, Afrique de l'Ouest) : biostratigraphie et paléogéographie*. Travaux de l'Institut
798 Scientifique de Rabat, série géologie et géographie physique, **20**, 92-107.

799 Leprêtre, R., Barbarand, J., Missenard, Y., Leparmentier, F. and Frizon de Lamotte, D. 2014. Vertical
800 movements along the northern border of the West African Craton : the Reguibat Shield and adjacent
801 basins. *Geological Magazine*, **151** (5), 885-898, doi:10.1017/S0016756813000939.

802 Leprêtre, R., Barbarand, J., Missenard, Y., Gautheron, C., Saddiqi, O. & Pinna-Jamme, R. 2015. Postrift
803 history of the eastern central Atlantic passive margin: Insights from the Saharan region of South
804 Morocco. *Journal of Geophysical Research: Solid Earth*, **120**(6), 4645-4666, doi:
805 10.1002/2014JB011549

806 Logan, P. & Duddy, I.R. 1998. An investigation of the thermal history of the Ahnet and Reggane
807 Basins, Central Algeria, and the consequences for hydrocarbon generation and accumulation. *In:*
808 MacGregor, D.S., Moody, R.T.J. & Clark-Lowes, D.D. (eds.). *Petroleum Geology of North Africa*,
809 Geological Society, London, Special Publications, **132**, 131- 155, doi: 10.1144/GSL.SP.1998.132.01.07.

810 Marzoli, A., Renne, P.R., Piccirillo, E.M., Ernesto, M., Bellieni, G. & De Min, A. 1999. Extensive 200
811 million-year-old continental flood basalts of the Central Atlantic Magmatic Province. *Science*, **284**,
812 616–618, doi:10.1126/science.284.5414.616

813 Lorencak, M., Kohn, B.P., Osadetz, K.G. & Gleadow, A.J.W., 2004. Combined apatite fission track and
814 (U–Th)/He thermochronometry in a slowly cooled terrane: results from a 3440-m-deep drill hole in
815 the southern Canadian Shield. *Earth and Planetary Science Letters*, **227**, 87-104,
816 doi:10.1016/j.epsl.2004.08.015.

817 Maillard, A., Malod, J., Thiébot, E., Klingelhoefer, F. & Réhault, J.-P. 2006. Imaging a lithospheric
818 detachment at the continent-ocean crustal transition off Morocco. *Earth and Planetary Science*
819 *Letters*, **241**, 686-698, doi:10.1016/j.epsl.2005.11.013.

820 Martinis, B. & Visintin, V. 1966. Données géologiques sur le bassin sédimentaire côtier de Tarfaya. *In:*
821 Reyre, D. (ed) *Sedimentary Basins of the African Coasts, Part 1: Atlantic Coast*, Association des
822 Services Géologiques Africains, Paris, 13-26.

823 Matton, G. & Jebrak, M. 2009. The Cretaceous Peri-Atlantic Alkaline Pulse (PAAP): deep mantle
824 plume origin or shallow lithospheric break-up? *Tectonophysics*, **469**, 1-12,
825 doi:10.1016/j.tecto.2009.01.001.

826 McDowell, F. W., McIntosh, W. C. & Farley, K. A. 2005. A precise ⁴⁰Ar–³⁹Ar reference age for the
827 Durango apatite (U–Th)/He and fission-track dating standard. *Chemical Geology*, **214**, 249–63,
828 doi:10.1016/j.chemgeo.2004.10.002.

829 McHone, J.G. & Butler, J.R. 1984. Mesozoic igneous provinces of New England and the opening of the
830 North Atlantic Ocean. *Geological Society of America Bulletin*, **95** (7), 757-765, doi: 10.1130/0016-
831 7606(1984)9.

832 Miall, A.D., Balkwill, H.R. & McCracken, J., 2008. The Atlantic Margin Basins of North America. *In:*
833 Miall, A.D. (ed) *The Sedimentary Basins of the United States and Canada, Sedimentary Basins of the*
834 *World*, Elsevier, Amsterdam, Boston, Heidelberg, **5**, 473-504, , doi: 10.1016/S1874- 5997(08)00014-2.

835 Michard, A., Soulaïmani, A., Hoepffner, C., Ouanaimi, H., Baidder, L., Rjimati, E.C. & Saddiqi, O. 2010.
836 The South-Western Branch of the Variscan Belt: Evidence from Morocco. *Tectonophysics*, **492**, 1-24,
837 doi:10.1016/j.tecto.2010.05.021.

838 Murray, K.E., Orme, D.A. & Reiners, P.W. 2014. Effects of U–Th-rich grain boundary phases on apatite
839 helium ages. *Chemical Geology*, **390**, 135-151, doi:10.1016/j.chemgeo.2014.09.023.

840 Oukassou, M., Saddiqi, O., Barbarand, J., Sebti, S., Baidder, L. & Michard, A. 2013. Post-Variscan
841 exhumation of the Central Anti-Atlas (Morocco) constrained by zircon and apatite fission-track
842 thermochronology. *Terra Nova*, **25** (2), 151-159, doi: 10.1111/ter.12019.

843 Peucat, J.J., Capdevila, R., Drareni, A., Mahdjoub, Y. & Kahoui, M. 2005. The Eglab massif in the West
844 African Craton (Algeria), an original segment of the Eburnean orogenic belt: petrology, geochemistry
845 and geochronology. *Precambrian Research*, **136**, 309-352, doi:10.1016/j.precamres.2004.12.002.

846 Poag, C.W. & Valentine, P.C. 1988. Mesozoic and Cenozoic stratigraphy of the United States Atlantic
847 continental shelf and slope. *In:* Sheridan, R.E. & Grow, J.A. (eds) *The geology of North America: the*
848 *Atlantic continental margin*, Geological Society of America, Boulder, Colorado, **1-2**, 67–85.

849 Poag, C.W. & Schlee, J. S. 1984. Depositional sequences and stratigraphic gaps on submerged United
850 States Atlantic margin. *In:* Schlee, J.S. (ed.) *Interregional Unconformities and Hydrocarbon*
851 *Accumulation*, American Association of Petroleum Geologists, Memoir, **36**, 165-182.

852 Potrel, A., Peucat, J.J. & Fanning, C.M. 1998. Archean crustal evolution of the West African Craton:
853 example of the Amsaga Area (Reguibat Rise). U-Pb and Sm-Nd evidence for crustal growth and
854 recycling. *Precambrian Research*, **90** (3-4), 107-117, doi:10.1016/S0301-9268(98)00044-8.

855 Ranke, U., von Rad, U. & Wissmann, G. 1982. Stratigraphy, facies and tectonic development of the
856 on- and off-shore Aaiun-Tarfaya basin-A review. In: von Rad, U., Hinz, K., Sarnthein, M. & Seibold, E.
857 (eds) *Geology of the Northwestern African Continental Margin*, Springer-Verlag, New York, Berlin,
858 Heidelberg, 86-105, doi: 10.1007/978-3-642-68409-8_6.

859 Ratschiller, L.K. 1968. *Lithostratigraphy of the Northern Sahara*. Museo tridentino di scienze naturali,
860 Trento, Italy.

861 Roden-Tice, M.K., Tice, S.J. and Schofield, I.S., 2000. Evidence for Differential Unroofing in the
862 Adirondack Mountains, New York State, determined by apatite fission-track thermochronology.
863 *Journal of Geology*, **108**, 155-169, doi: 10.1086/314395.

864 Roden-Tice, M.K. & Wintsch, R.P., 2002. Early Cretaceous Normal Faulting in Southern New England:
865 Evidence from Apatite and Zircon Fission-Track Ages. *Journal of Geology*, **110** (2), 159-178, doi:
866 10.1086/338281.

867 Roden-Tice, M.K. & Tice, S.J., 2005. Regional-Scale Mid-Jurassic to Late Cretaceous Unroofing from
868 the Adirondack Mountains through Central New England Based on Apatite Fission-Track and
869 (U-Th)/He Thermochronology. *Journal of Geology*, **113** (5), 535-552, doi: 10.1086/431908.

870 Roden-Tice, M.K., Dykstra Eusden, J. & Wintsch, R.P. 2012. Apatite fission-track evidence for the
871 Cretaceous development of kilometer-scale relief and steady-state Tertiary topography in New
872 England. *Geomorphology*, **141-142**, 114-120, doi:10.1016/j.geomorph.2011.12.029.

873 Rosenbaum, G., Lister, G.S. & Duboz, C., 2002. Relative motions of Africa, Iberia and Europe during
874 Alpine orogeny. *Tectonophysics*, **359**, 117-129, doi:10.1016/S0040-1951(02)00442-0.

875 Rougier, S. 2012. *Interactions Lithosphère-Asténosphère et mouvements verticaux : Le cas du massif*
876 *du Hoggar*. PhD thesis, Université Paris Sud XI, France.

877 Rougier, S., Missenard, Y., Gautheron, C., Barbarand, J., Zeyen, H., Pinna, R., Liégeois, J.P., Bonin, B.,
878 Ouabadi, A., Derder, M. E.M. & Frizon de Lamotte, D. 2013. Eocene exhumation of the Tuareg Shield
879 (Sahara Desert, Africa). *Geology*, **41** (5), 615-618, doi: 10.1130/G33731.1.

880 Ruiz, G. M. H., Sebti, S., Negro, F., Saddiqi, O., Frizon de Lamotte, D., Stockli, D., Foeken, J., Stuart, F.,
881 Barbarand, J. & Schaer, J.-P. 2011. From central Atlantic continental rift to Neogene uplift – western
882 Anti-Atlas (Morocco). *Terra Nova*, **23**, 35-41, doi: 10.1111/j.1365-3121.2010.00980.x.

883 Saddiqi, O., El Haimer, F.-Z., Michard, A., Barbarand, J., Ruiz, G. M. H., Mansour, E. M., Leturmy, P. &
884 Frizon de Lamotte, D. 2009. Apatite fission-track analyses on basement granites from south-western
885 Meseta, Morocco: paleogeographic implications and interpretation of AFT age discrepancies.
886 *Tectonophysics*, **475**, 29-37, doi:10.1016/j.tecto.2009.01.007.

887 Schettino, A. & Turco, E., 2009. Breakup of Pangaea and plate kinematics of the central Atlantic and
888 Atlas regions. *Geophysical Journal International*, **178**, 1078-1097, doi: 10.1111/j.1365-
889 246X.2009.04186.x.

890 Schofield, D.I., Horstwood, M.S.A., Pitfield, P.E.J., Gillespie, M., Darbyshire, F., O'Connor, E.A. &
891 Abdouloye, T.B. 2012. U–Pb dating and Sm–Nd isotopic analysis of granitic rocks from the Tiris
892 Complex: New constraints on key events in the evolution of the Reguibat Shield, Mauritania.
893 *Precambrian Research*, **204-205**, 1-11, doi:10.1016/j.precamres.2011.12.008.

894 Sebti, S., Saddiqi, O., El Haimer, F.Z., Michard, A., Ruiz, G., Bousquet, R., Baidder, L. & Frizon de
895 Lamotte, D. 2009. Vertical movements at the fringe of the West African Craton: First zircon fission
896 track datings from the Anti-Atlas Precambrian basement, Morocco. *Comptes Rendus Géoscience*, **341**,
897 71-77, doi:10.1016/j.crte.2008.11.006.

898 Sehrt, M. 2014. *Variscan to Neogene long-term landscape evolution at the Moroccan passive*
899 *continental margin (Tarfaya Basin and western Anti-Atlas)*. PhD thesis, Ruprecht-Karls-Universität,
900 Heidelberg, Germany.

901 Sheridan, R.E. & Grow, J.A. 1988. *The Atlantic continental margin*, Geological Society of America,
902 Boulder, Colorado, USA.

903 Shuster, D.L., Flowers, R.M. and Farley, K.A., 2006. The influence of natural radiation damage on
904 helium diffusion kinetics in apatite. *Earth and Planetary Science Letters*, **249**, 148-161,
905 doi:10.1016/j.epsl.2006.07.028.

906 Shuster, D.L. & Farley, K.A., 2009. The influence of artificial radiation damage and thermal annealing
907 on helium diffusion kinetics in apatite. *Geochimica et Cosmochimica Acta*, **73**, 183-196,
908 doi:10.1016/j.gca.2008.10.013.

909 Spiegel C., Kohn B., Belton D., Berner Z., Gleadow A. (2009) Apatite (U–Th–Sm)/He
910 thermochronology of rapidly cooled samples: The effect of He implantation. *Earth and Planetary*
911 *Science Letters* **285**, 1–2, 105–114

912 Spotila, J.A., Bank, G.C., Reiners, P.W., Naeser, C.W., Naeser, N.D. & Henika, B.S., 2004. Origin of the
913 Blue Ridge escarpment along the passive margin of Eastern North America. *Basin Research*, **16**, 41-
914 63, doi: 10.1046/j.1365-2117.2003.00219.x.

915 Stampfli, G.M. & Borel, G.D. 2004. The TRANSMED Transects in Space and Time: Constraints on the
916 Paleotectonic Evolution of the Mediterranean Domain. *In: Cavazza, W., Roure, F., Spakman, W.,*
917 *Stampfli, G.M. & Ziegler, P.A. (eds) The TRANSMED Atlas. The Mediterranean Region from Crust to*
918 *Mantle*, Springer, Berlin, Heidelberg, 53-80, doi: 10.1007/978-3-642-18919-7_3.

919 Tavakoli-Shirazi, S., Frizon de Lamotte, D., Wrobel-Daveau, J.C. & Ringenbach, J.C. 2012. Pre-Permian
920 uplift and diffuse extensional deformation in the High Zagros Belt (Iran): integration in the

921 geodynamic evolution of the Arabian plate. *Arabian Journal of Geosciences*, **6** (7), 2329-2342, doi:
922 10.1007/s12517-012-0542-5.

923 Taylor, J.P. & Fitzgerald, P. 2011. Low-temperature thermal history and landscape development of
924 the eastern Adirondack Mountains, New York: Constraints from apatite fission-track
925 thermochronology and apatite (U-Th)/He dating. *Geological Society of America Bulletin*, **123** (3-4),
926 412-426, doi: 10.1130/B30138.1.

927 Trompette, R. 1973. *Le Précambrien et le Paléozoïque inférieur de l'Adrar de Mauritanie (bordure*
928 *occidentale du bassin de Taoudeni, Afrique de l'Ouest). Un exemple de sédimentation de craton.*
929 *Etude stratigraphique et sédimentologique.* Travaux du Laboratoire de Sciences de la Terre, St-
930 Jérôme, Marseille.

931 Tucholke, B.E., Sawyer, D.S. & Sibuet, J.C. 2007. Breakup of the Newfoundland-Iberia rift. *In*: Karner,
932 G.D., Manatschal, G. & Pinheiro, L.M. (eds) *Imaging, Mapping and Modelling Continental Lithosphere*
933 *Extension and Breakup*, Geological Society, London, Special Publications, **282**, 9-46, doi:
934 10.1144/SP282.2.

935 Turner, J.P., Green, P.F., Holford, S.P. & Lawrence, S.R. 2008. Thermal history of the Rio Muni)-NE
936 Brazil margins during continental breakup. *Earth and Planetary Science Letters*, **270**, 354-367, doi:
937 doi:10.1016/j.epsl.2008.04.002.

938 Verati, C., Bertrand, H. & Féraud, G. 2005. The farthest record of the Central Atlantic Magmatic
939 Province into West Africa Craton: Precise $^{40}\text{Ar}/^{39}\text{Ar}$ dating and geochemistry of Taoudenni basin
940 intrusives (northern Mali). *Earth and Planetary Science Letters*, **235**, 391-407,
941 doi:10.1016/j.epsl.2005.04.012.

942 Verati, C., Rapaille, C., Féraud, G., A. Marzoli, Bertrand, H. & Youbi, N. 2007. $^{40}\text{Ar}/^{39}\text{Ar}$ ages and
943 duration of the Central Atlantic Magmatic Province volcanism in Morocco and Portugal and its

944 relation to the Triassic–Jurassic boundary. *Palaeogeography, Palaeoclimatology, Palaeoecology*, **244**,
945 308-325, doi:10.1016/j.paleo.2006.06.033.

946 Villeneuve, M. 2008. Review of the orogenic belts on the western side of the West African craton: the
947 Bassarides, Rokelides and Mauritanides. *In: Ennih, N., & J.P. Liégeois, J.P. (eds.), The boundaries of*
948 *the West African Craton*, Geological Society, London, Special Publications, **297**, 169-201, doi:
949 10.1144/SP297.8.

950 von Rad, U., & Sarti, M. 1986. Early Cretaceous “events” in the evolution of the eastern and western
951 North Atlantic continental margins. *Geologische Rundschau*, **75** (1), 139-158,
952 doi:10.1007/BF01770184.

953 von Rad, U., Hinz, K., Sarnthein, M. & Seibold, E. 1982. *Geology of the Northwest African Continental*
954 *Margin*, Springer, Berlin, Heidelberg.

955 Wade, J.A. & McLean, B.C. 1990. The Stratigraphy of Georges Bank Basin and Relationships To the
956 Scotian Basin. *In: Keen, M.J. & Williams, G.L. (eds) Geology of the Continental Margin of Eastern*
957 *Canada*, Geological Survey of Canada, Geology of Canada Series, **2**, 190-238.

958 Wang, H.F., Crowley, K.D. & Nadon, G.C. 1994. Thermal History of the Michigan Basin from Apatite
959 Fission-Track Analysis and Vitrinite Reflectance. *In: Ortoleva, P.J. (ed.) Basin Compartments and Seals*,
960 AAPG Special Volume, **M61**.

961 Wildman, M., Brown, R.W., Watkins, R., Carter, A., Gleadow, A. & Summerfield, M. 2015. Post break-
962 up tectonic inversion across the southwestern cape of South Africa: New insights from apatite and
963 zircon fission track thermochronometry. *Tectonophysics*, **654**, 30-55,
964 doi:10.1016/j.tecto.2015.04.012.

965

966

967 **Figure captions**

968 Fig. 1: Geological map of the Reguibat Shield and location of the samples. (a) Geographical location of
969 the studied area. The Reguibat Shield belongs to the NWAC, bounded to the East by the Panafrican
970 suture, separating it from the Tuareg Shield. Tf: Tindouf Basin; Td: Taoudeni Basin; lu: lullemeden
971 Basin; Ah: Ahnet Basin; O.M: Oued Mya Basin; Gh: Ghadames Basin. (b) Geological map of the
972 Reguibat Shield. TLDB: Tarfaya-Laayoune-Dakhla Basin. Samples have black or grey labels depending
973 on whether they are published or new data, respectively. Mixed labels (*e.g.* TGH4072A) indicate that
974 AFT data have been published but AHe data are new. Cret. : Cretaceous. (c) Simplified stratigraphical
975 log of the TLDB (modified after Leprêtre *et al.*, 2015). 1: conglomerates and coarse detrital
976 sediments; 2: coarse to fine sandstones; 3: shales with variable sandy proportion; 4: Shales and clays,
977 sometimes interbedded with limestones; 5: limestones.

978 Fig. 2: Segmentation of the Reguibat shield based on the LTT results. The data are projected along a
979 NW-SE transect, perpendicular to the Central Atlantic passive margin. AHe ages are Ft corrected
980 ages. Errors for AFT and AHe ages are indicated at 2σ . The distinction between the three domains of
981 the Reguibat Shield is evidenced by the dispersion of the data and discussed in the text (section
982 Sampling). Red outlines correspond to new data.

983 Fig. 3: AFT age vs. MTL plot for the whole Reguibat Shield. The grey bar indicates the timing and
984 duration of the Jurassic rifting up to break-up, as defined by Labails *et al.* (2010).

985 Fig. 4: Track length distributions for all samples. They are separated by geographical area. Samples
986 with more than 50 measured confined lengths have their names in black boxes.

987 Fig. 5: Corrected AHe ages vs. eU plots. (a) for the eastern Reguibat Shield; (b) for the central
988 Reguibat Shield; (c) for the western Reguibat Shield. (d-i) Raw AHe ages vs. eU plots for the eastern
989 Reguibat with expanded eU scale to better image to relationship between AHe age and eU. Light
990 colored areas underline the grouping of single-grain AHe ages.

991 Fig. 6: Representative individual modeling for each domain of the Reguibat Shield. (a) Thermal
992 modeling of sample GH3 in the eastern Reguibat Shield. (b) Predicted single-grain AHe ages against
993 measured ones. Ages are corrected for Ft. (c) Predicted AFT data against measured ones. (d), (e) and
994 (f) show the thermal modeling results for sample TGH3163 in the central Reguibat Shield, with the
995 same legend than (a), (b) and (c), respectively. (g) and (h) show the thermal modeling results for
996 sample AG167 in the western Reguibat Shield, with the same legend than (a) and (c), respectively.

997 Fig. 7: Inverse thermal modelings for the three Reguibat Shield domains. (a-c) Thermal modeling
998 results for the eastern Reguibat Shield (a), for the central Reguibat Shield (b) and for the western
999 Reguibat Shield (after Leprêtre *et al.*, 2015 for AOS, SC, TAS233 and TAS29 samples) (c). The light grey
1000 box indicates in each panel the duration of the major cooling event. The dark grey box in (b-c) shows
1001 the duration of the subsequent reheating, which is not recorded in the eastern Reguibat Shield (a).
1002 For the western domain, black thermal paths correspond to the thermal modelings realized by
1003 Leprêtre *et al.* (2015). Due to the new AHe data, we have made new thermal modeling for the data
1004 from the central domain obtained by Leprêtre *et al.* (2014). For all modelings, the way we have
1005 defined the constraint-boxes is explained within the text.
1006 Fig. 8: Forward modeling for the central
1007 Reguibat Shield. (a) Tested thermal paths with HeFTy software (Ketcham, 2005). (b) Corresponding
1008 predicted AHe ages for each tested thermal path in (a). The measured Ft-corrected single-grain AHe
1009 ages are also indicated to ensure direct comparison. A small simplified map of the Reguibat Shield
1009 shows the segmentation between the different domains.

1010 Fig. 8: Forward and inverse modeling for the central Reguibat Shield. (a) Tested thermal paths with
1011 HeFTy software (Ketcham, 2005). (b) Corresponding predicted AHe ages for each tested thermal path
1012 in (a).

1013 Fig. 9: Comparison between AFT datasets of the conjugate passive margins of the northern Central
1014 Atlantic Ocean. (a, b) DEMs of Northeast America and Northwest Africa, respectively. Colored dots
1015 locate the AFT samples of the different studies quoted in the text with a color scale for the range of

1016 AFT ages. White lines are the profiles used to project the data with respect to the hinge line. (c, d)
1017 AFT datings along perpendicular profiles, from the hinge line at $x=0$. For the African AFT profile, data
1018 are from: Ghorbal *et al.* (2008); Saddiqi *et al.* (2009); Ruiz *et al.* (2011); Oukassou *et al.* (2013),
1019 Leprêtre *et al.* (2014, 2015) and this study. For the American profile, data come from the studies
1020 quoted in the text. Smaller panels on each profile show the MTL vs. AFT age plot. The grey bar
1021 indicates the age range of the rifting of the Central Atlantic Ocean (Labails *et al.*, 2010).

1022 Fig. 10: Comparison of Middle Jurassic-Aptian stratigraphical record of Central Atlantic Ocean
1023 conjugate passive margins. The map at the bottom shows the approximate position of North America
1024 and West Africa at Chron 25 (154 Ma). Continent contours and the 2 km-depth bathymetry are the
1025 present-day ones. The basins whose stratigraphy is described in the text are located in dark grey. The
1026 margins have been divided into a northern and a southern segment, given their respective
1027 stratigraphy. Only one stratigraphical log is used for the northern segment since all basins shared a
1028 common evolution during the considered period. Legend for sedimentary rocks: 1. marls; 2.
1029 carbonates; 3. Dolomites, 4. siltstones and marls; 5. coarse clastics; 6. sandstones to siltstones.
1030 Legend for the period described on the stratigraphic logs: EJ. Early Jurassic; MJ: Middle Jurassic; LJ:
1031 Late Jurassic; NC: Neocomian (Berriasian-Hauterivian); BAP: Barremian-Aptian.

1032 Fig. 11: Evolution of the spreading rates in the Central Atlantic Ocean from Early Jurassic to Early
1033 Cretaceous. This compilation is based on works by Schettino & Turco (2009), Labails *et al.* (2010) and
1034 Kneller *et al.* (2012).

1035 Fig. 12: Representative thermal paths from the onshore eastern North America. Thermal paths are
1036 coming from: (a) Nova Scotia in the northern proximal passive margin (Grist & Zentili, 2003); (b) the
1037 Michigan Basin, deep in the interior of the continent (Wang *et al.*, 1994); (c) the southern Canadian
1038 Shield (Lorenca *et al.*, 2004); (d) the Northern Appalachian (Taylor & Fitzgerald, 2011). Dark grey box
1039 defines the main period of uplift in the western and central Reguibat Shield domains in the
1040 conjugated African passive margin.

1041 Table 1: AFT results*

	Sample	Rock-type	Location	Elevation (m)	$\rho_s (10^5 \cdot \text{cm}^{-2})$ / Ns	$\rho_i (10^5 \cdot \text{cm}^{-2})$ / Ni	$\rho_d (10^5 \cdot \text{cm}^{-2})$ / Nd	P (χ^2) %	Central age (Ma) $\pm 1\sigma$	U (ppm)	MTL (μm) \pm se	Std dev.	Dpar (μm)
<i>Western domain</i>	AG167	charnockite	13°24'2.07"W	233	0.218	0.195	6.73	74	137 \pm 12	4	-	-	1.72 \pm 0.1
			20°42'56.76"N		323	289	6849		(20)		-		-
	AG169	charnockite	13°24'2.07"W	237	0.201	0.207	6.682	93	118 \pm 10	4	-	-	1.54 \pm 0.2
			20°42'56.76"N		309	319	6849		(20)		-		-
<i>Central domain</i>	TGH3111B	granite	9°22'12"W	252	3.246	2.598	6.611	65	150 \pm 8	48	11.9 \pm 0.2	1.7	1.63 \pm 0.1
			24° 00'00"N		1097	878	6563		(20)		(101)		
	TEN4065	microgranite	10° 1'47.00"W	258	6.444	4.462	6.595	8	172 \pm 13	82	11.7 \pm 0.3	2	2.06 \pm 0.5
			24°20'23.00"N		883	477	6563		(20)		(35)		
	AL10	granodiorite	7° 7'5.15"W	394	1.334	0.866	7.255	63	202 \pm 14	15	12 \pm 0.2	1.6	1.77 \pm 0.1
			26°37'33.06"N		675	438	6849		(20)		(49)		
	YT7	monzogranite	7°20'37.34"W	384	1.862	1.394	6.825	72	166 \pm 8	25	11.4 \pm 0.3	1.8	1.60 \pm 0.2
			26°28'59.39"N		1380	1033	6849		(20)		(49)		
<i>Eastern domain</i>	IG3	rhyolite	6° 9'0.43"W	366	0.469	0.149	6.968	84	393 \pm 36	3	-	-	1.66 \pm 0.2
			26° 6'22.40"N		543	172	6849		(20)		-		
	CH1	gabbrodiorite	3°35'36.69"W	252	1.098	0.454	7.159	6	307 \pm 26	8	11.5 \pm 0.2	2.1	1.86 \pm 0.2
			25°35'45.94"N		862	356	6849		(20)		(101)		
	CH2	gabbrodiorite	3°35'36.69"W	252	3.105	1.516	7.112	18	264 \pm 21	26	12 \pm 0.2	1.7	1.99 \pm 0.2
			25°35'45.94"N		770	376	6849		(20)		(69)		
	CH3	gabbrodiorite	3°35'36.69"W	252	1.059	0.426	7.064	86	315 \pm 24	7	11.5 \pm 0.3	2.3	1.95 \pm 0.2
			25°35'45.94"N		686	276	6849		(20)		(64)		
	GH3	trondhjemite	6° 3'54.77"W	360	1.177	0.41	7.016	6	359 \pm 27	7	11.5 \pm 0.2	1.9	1.76 \pm 0.2
			25°29'36.53"N		1130	394	6849		(20)		(100)		
	DEG6	gabbro	2°57'15.60"W	355	2.276	0.701	6.111	46	355 \pm 25	12	11.2 \pm 0.4	2.1	1.97 \pm 0.1
			26° 4'50.02"N		1065	328	6849		(20)		(27)		
	GH20	gabbro	6° 0'2.87"W	350	0.471	0.101	5.996	73	497 \pm 61	2	-	-	1.75 \pm 0.1
			25°32'51.89"N		206	44	3012		(10)		-		
	TL3	gabbro	3°10'37.45"W	381	0.818	0.376	6.052	66	237 \pm 21	8	-	-	2.12 \pm 0.2
			27°21'31.99"N		447	207	3012		(20)		-		

1042

1043 * ρ – density of tracks with s and i – spontaneous and induced densities in apatite crystals and the mica detector; d – tracks density of the neutron glass
1044 monitor (CN5); for ρ_s , ρ_i , ρ_d , are written in italics the number of counted tracks. Densities are expressed in $10^5 t/cm^2$. MTL – mean track length. Values in
1045 bracket for central age and MTL are, respectively, the number of single-grain ages and the number of lengths measured. 1σ is the standard deviation. Dpar
1046 corresponds to a kinetic factor determined for each sample (Barbarand *et al.*, 2003).

1047

1048

1049

1050

1051 Table 2: AHe results*

	Name	Rs (μm)	Weight(μg)	F_r	$^4\text{He}(\text{ncc/g})$	U (ppm)	Th (ppm)	Sm (ppm)	eU (ppm)	Age (Ma)	Age c. (Ma)
<i>Central</i>	1153-A	80.8	11.85	0.87	46201.6	3.8	11.9	7.0	6.7	57	66 \pm 5
<i>Domain</i>	1153D	34.4	1.17	0.715	120399,0	10.4	31.9	20.3	18.3	55	77 \pm 6
	1153-F	63.2	6.54	0.815	100000.8	7.6	20.3	9.5	12.6	66	81 \pm 6
	1153-H	59	4.69	0.83	63086.4	11.2	22.6	12.5	16.7	31	38 \pm 3
	1153-I	47.5	2.56	0.79	57756,0	5.5	16.8	13.3	9.6	50	63 \pm 5
	3163-A	54.1	3.6	0.809	717183.1	37.7	1.9	27.2	38.3	155	191 \pm 15
	3163-E	66	7.11	0.827	288616.5	16.9	1.4	17.6	17.4	137	166 \pm 13
	3163-I	65.6	6.26	0.847	470679.8	17.8	25.6	24.6	24.1	162	191 \pm 15
	3163G	96.1	17.27	0.875	549045.6	25,0	22,0	NA	30.3	150	172 \pm 14
	AL10-A	46	2.4	0.755	405681.5	22.5	20.6	31.8	27.7	121	161 \pm 13
	AL10-E	39.3	1.18	0.701	675195,0	76.1	26.7	31.3	82.8	67	96 \pm 8*
	AL10-C	50.5	3.53	0.765	229447.2	11.1	11.9	29.3	14.2	134	175 \pm 14
	AL10-L	44.1	1.57	0.679	1341456.8	34.3	31.1	59.4	42.2	263	388 \pm 31*
	AL10-J	37.2	1.22	0.724	231868.3	7.9	10,0	37.4	10.5	182	252 \pm 20
	AL10-I	45.5	2.02	0.76	395904.9	22.4	14.9	41,0	26.3	124	164 \pm 13
	AL10-B	39	1.39	0.726	557702.2	20.6	11.6	37.5	23.7	195	269 \pm 21
	AL10-K	37.9	1.28	0.717	145483.1	12.5	8.8	35.5	14.9	81	112 \pm 9
	AL10-F	38.7	1.23	0.687	129286.7	9.5	15.8	44.8	13.6	79	115 \pm 9
	AL10-G	39.9	1.23	0.707	1327362.4	32.4	26.5	65.3	39.3	280	396 \pm 32*
	AL10-H	42.6	1.58	0.713	236976.2	18.4	18.2	50.1	23.2	85	119 \pm 10
<i>Eastern</i>	CH1-A	47.3	2.43	0.789	79475.1	7.2	6.9	5.3	9	74	93 \pm 7

<i>Domain</i>	CH1-B	56.4	4.13	0.809	28513.1	2.7	3.2	1.4	3.5	68	84 ± 7
	CH1-C	49.4	2.68	0.802	48729.7	13.1	11.1	5.3	15.8	26	32 ± 3*
	CH1-D	40.2	1.45	0.751	205297.8	10.1	12.5	5.6	13.1	130	173 ± 14
	CH1-F	38.8	1.31	0.754	127741.1	11	9.6	3.4	13.3	80	106 ± 8
	CH1-G	64	6.37	0.831	88950.2	6.2	8.5	5.1	8.2	90	108 ± 9
	CH1-H	37.9	1.28	0.717	392039.3	26.1	23.4	6	31.8	102	143 ± 11
	CH1-J	50.6	3.96	0.761	141712.3	5,0	6.5	4.5	6.6	178	234 ± 19
	CH1-K	40.7	1.74	0.723	190623.3	19,0	10.3	14.9	21.6	73	101 ± 8
	CH3-C	50.5	3.04	0.789	119938.2	4.2	5.9	3.7	5.7	175	222 ± 18
	CH3-F	35.5	0.96	0.717	191786.5	13.4	11.3	4.2	16.1	99	138 ± 11
	CH3-A	54.7	4.25	0.79	93992.9	5.7	5.5	3.2	7	111	141 ± 11
	CH3-G	59.2	6.11	0.793	71842,0	3.7	5	2.7	4.9	122	153 ± 12
GH3A	GH3A	66.1	7.49	0.823	292746.2	8.1	5.6	12.7	9.6	253	307 ± 25
	GH3B	91.1	21.74	0.876	172995.7	4.7	4.6	6.4	5.9	243	278 ± 22
	GH3-C	71.5	8.99	0.842	56806.1	4.5	3.5	8.9	5.4	88	104 ± 8
	GH3-E	57.9	4.06	0.784	230520.3	6.5	3.8	10.8	7.5	256	326 ± 26
	GH3-F	99	19.03	0.883	21444.4	1.7	0.4	2.2	1.8	98	111 ± 9
IG3-C	IG3-C	43.8	1.72	0.722	332846.2	18.1	18.9	44.7	23	120	166 ± 13
	IG3-E	39.4	1.31	0.686	191182.1	5	10	48.9	7.8	203	295 ± 24
	IG3-F	36.7	0.99	0.675	118582.6	3.8	10.9	47.2	6.8	146	216 ± 17
	IG3-G	40.6	1.56	0.741	91106.9	3.7	4.9	38.8	5.1	147	198 ± 16
	IG3-I	40.4	1.67	0.721	187725,0	3.9	5.5	49.9	5.6	277	384 ± 31
TL3-L	TL3-L	41.1	1.58	0.745	131554.4	6.3	18.8	29.8	11.1	99	133 ± 11
	TL3-B	49.4	2.68	0.803	66784.2	8.8	17	23.8	13.1	42	53 ± 4
	TL3-C	41.3	1.57	0.778	73141.8	9.2	43.5	27	19.8	31	40 ± 3*
	TL3-D	39	1.44	0.717	86327.5	6.3	20.9	33.8	11.6	62	87 ± 7

TL3-F	41.4	1.92	0.717	123516.5	7.1	25.1	35.2	13.4	77	107 ± 9
TL3-G	43.5	1.98	0.745	95782.6	6.4	21.9	34.3	12	67	89 ± 7
TL3-J	52	3.29	0.797	93130.9	5.4	17.1	25.4	9.7	80	101 ± 8
TL3-H	47	2.35	0.777	123871.0	8	27.5	36.9	14.9	69	89 ± 7
TL3-K	46.6	2.77	0.746	21915.9	3.6	8.2	19.6	5.7	32	42 ± 3
GH20-A	36.4	1.14	0.702	58542.3	5.8	5.2	129.6	8.1	60	85 ± 7
GH20-C	37.4	1.28	0.703	74174.8	12.9	6.9	26.5	14.7	42	59 ± 5
GH20-D	37.4	1.28	0.703	54325.7	5.9	5.1	31.4	7.3	61	87 ± 7
GH20-F	41.1	1.58	0.745	34723.6	4.1	5.3	30.5	5.7	51	68 ± 5
GH20-H	35.1	1.22	0.663	37173.2	9.5	6.2	37.8	11.2	27	41 ± 3
GH20-G	39.2	1.52	0.711	54027.8	11.1	7	34.3	13.1	34	48 ± 4

1052

1053 * R_s (sphere equivalent radius) and F_T (ejection factor) have been calculated using the developed procedure of Gautheron & Tassan-Got (2010) and Ketcham
1054 *et al.* (2011). eU (effective uranium) has been calculated with the formula $[eU] = [U] + 0.24*[Th] + 0.008*[Sm]$. "Age c." means (U-Th-Sm)/He age corrected
1055 from alpha-ejection with the F_T . The error is estimated to be a maximum of 8%.

Figure 1

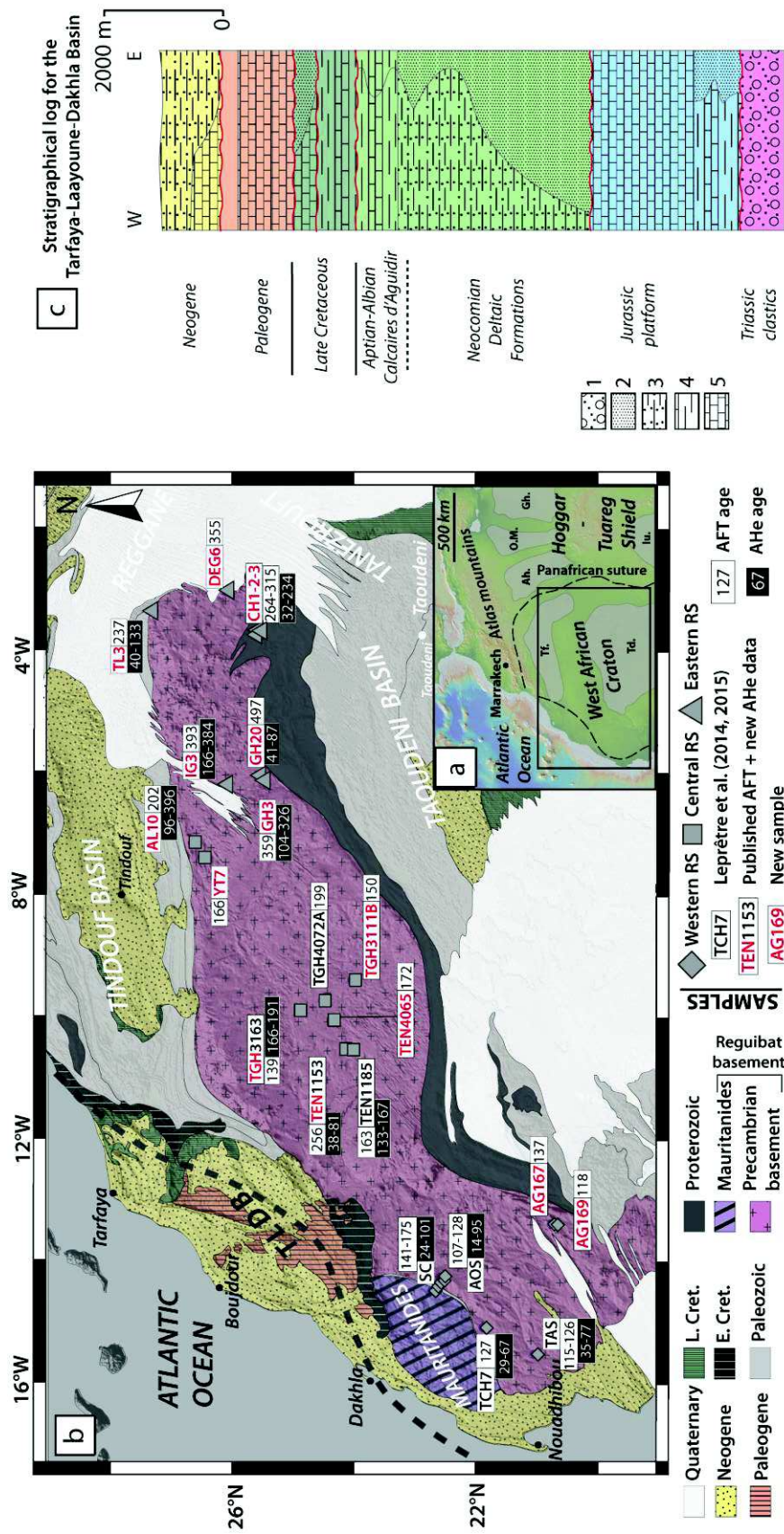


Figure 2

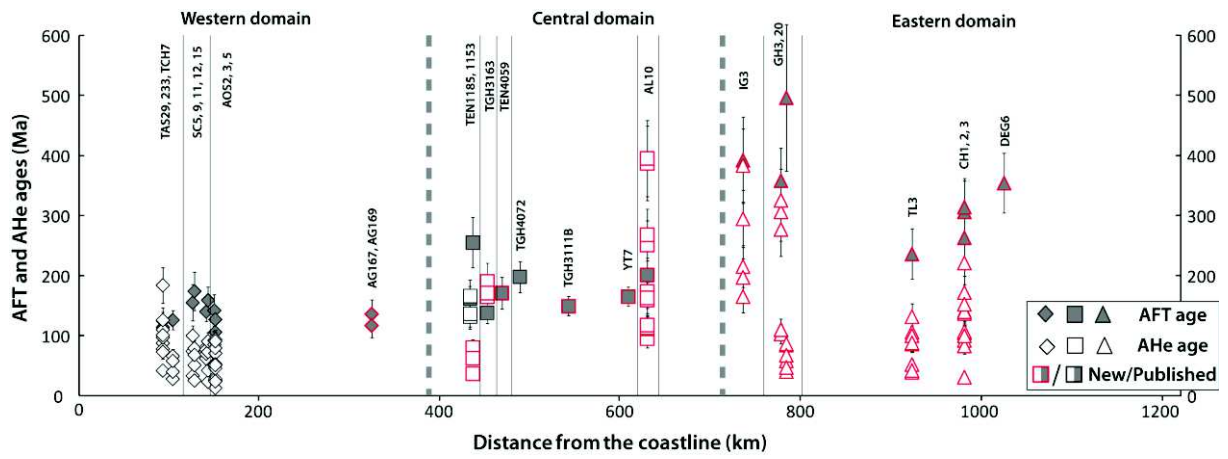


Figure 3

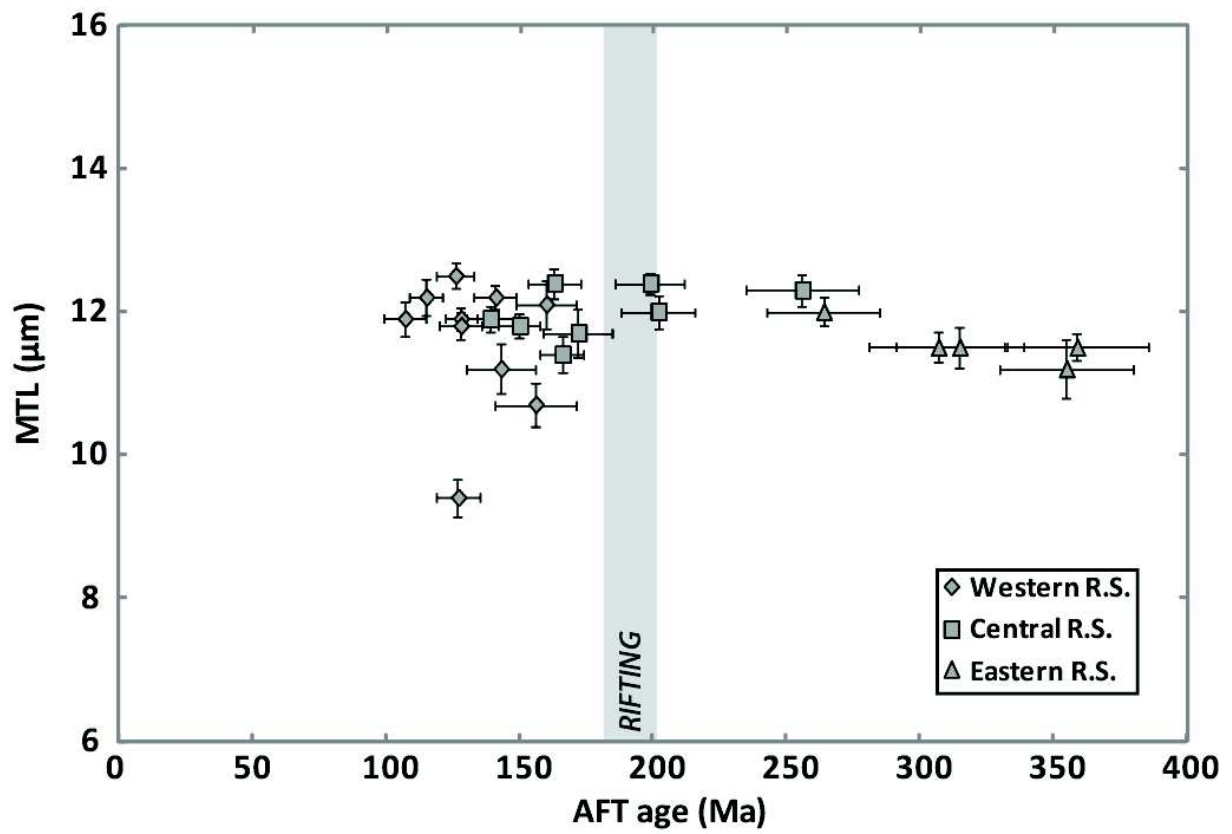


Figure 4

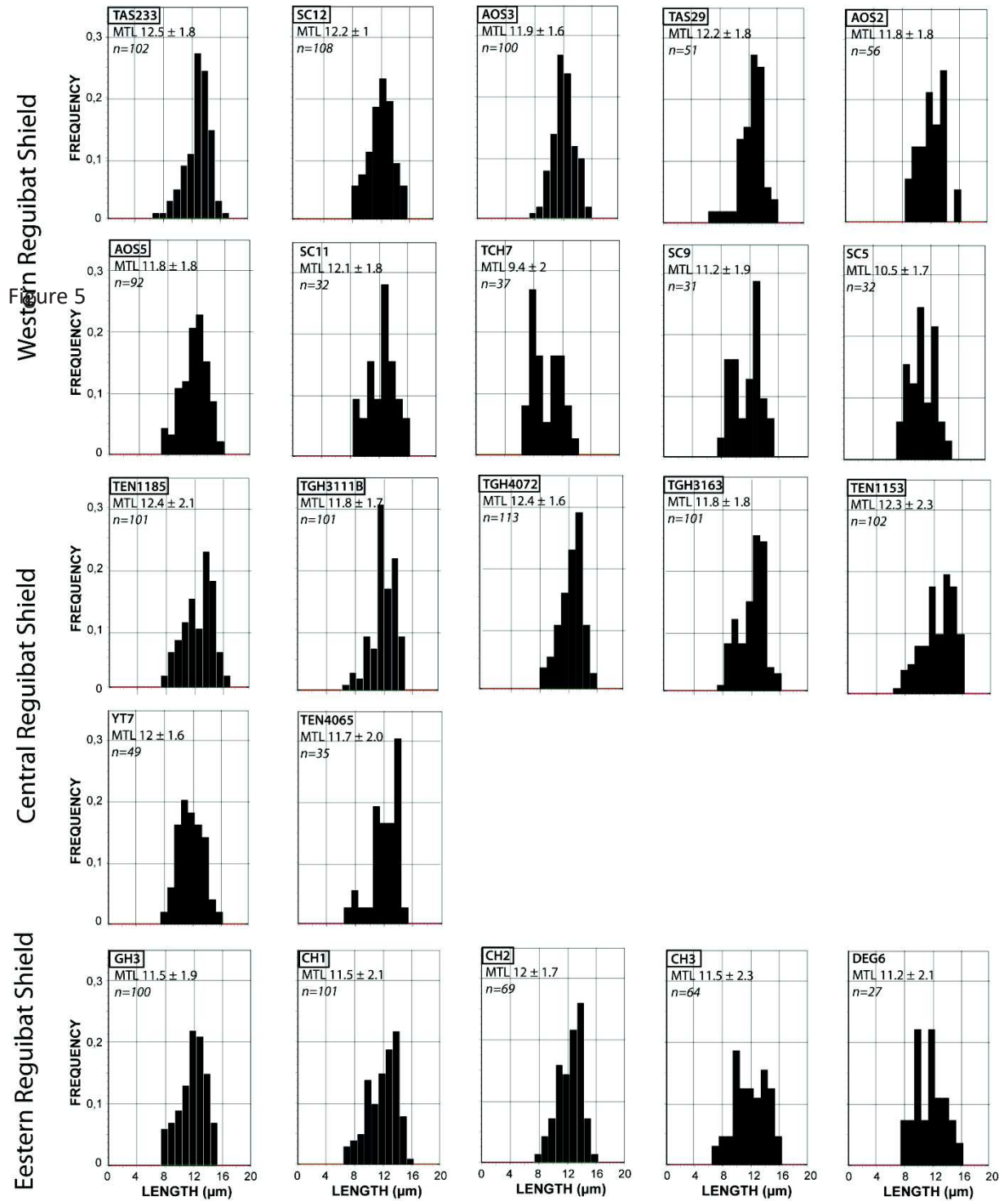


Figure 5

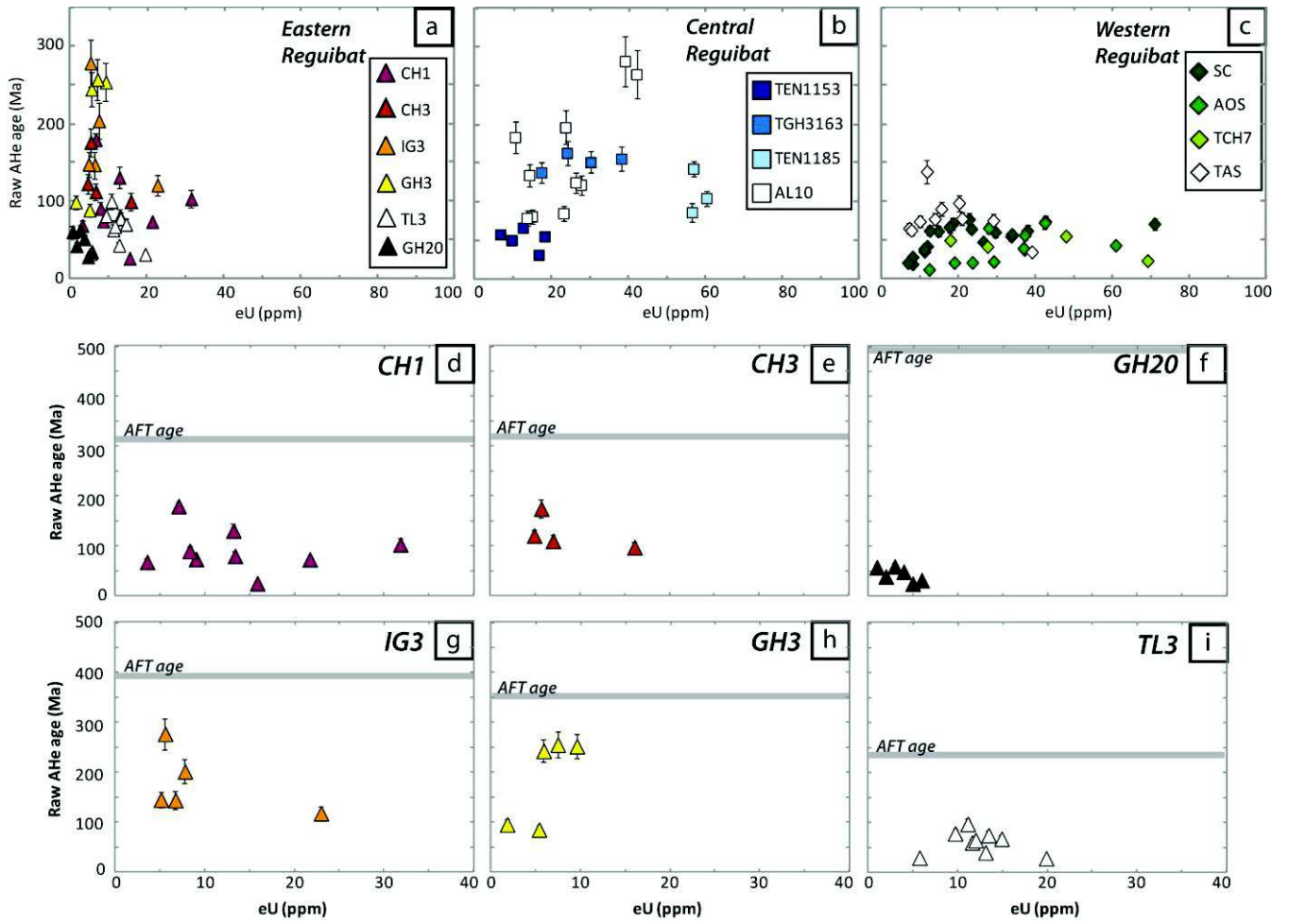


Figure 6

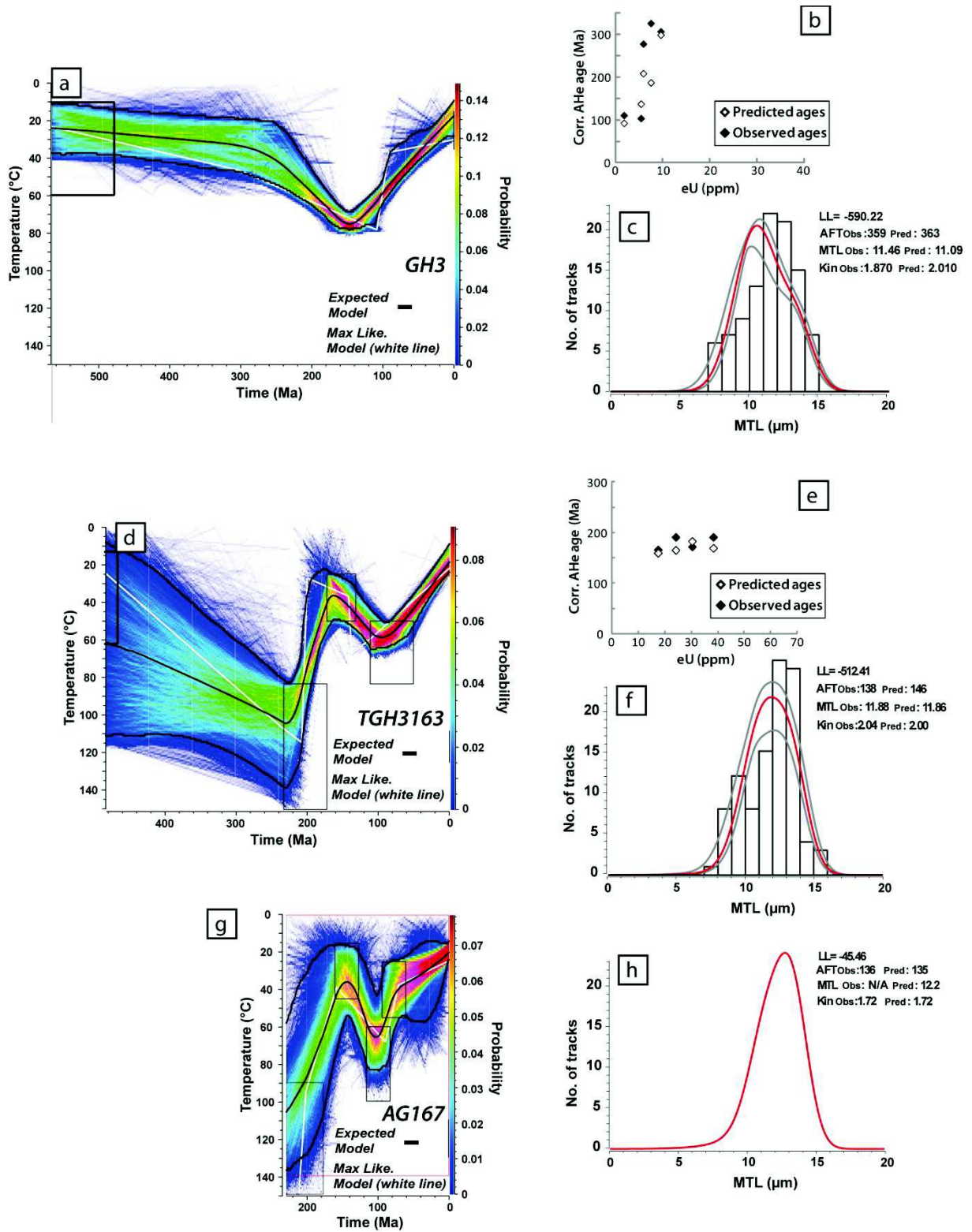


Figure 7

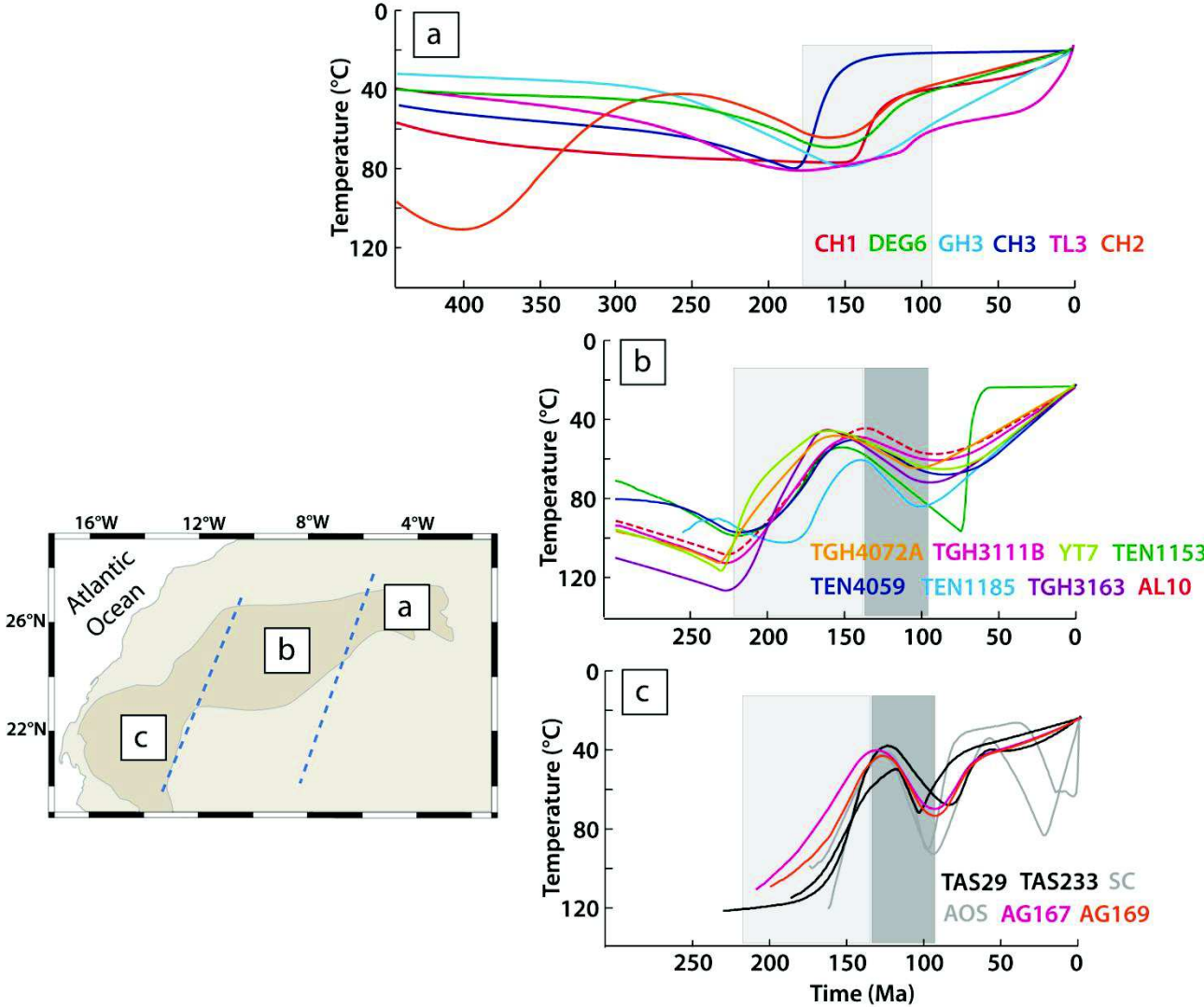


Figure 8

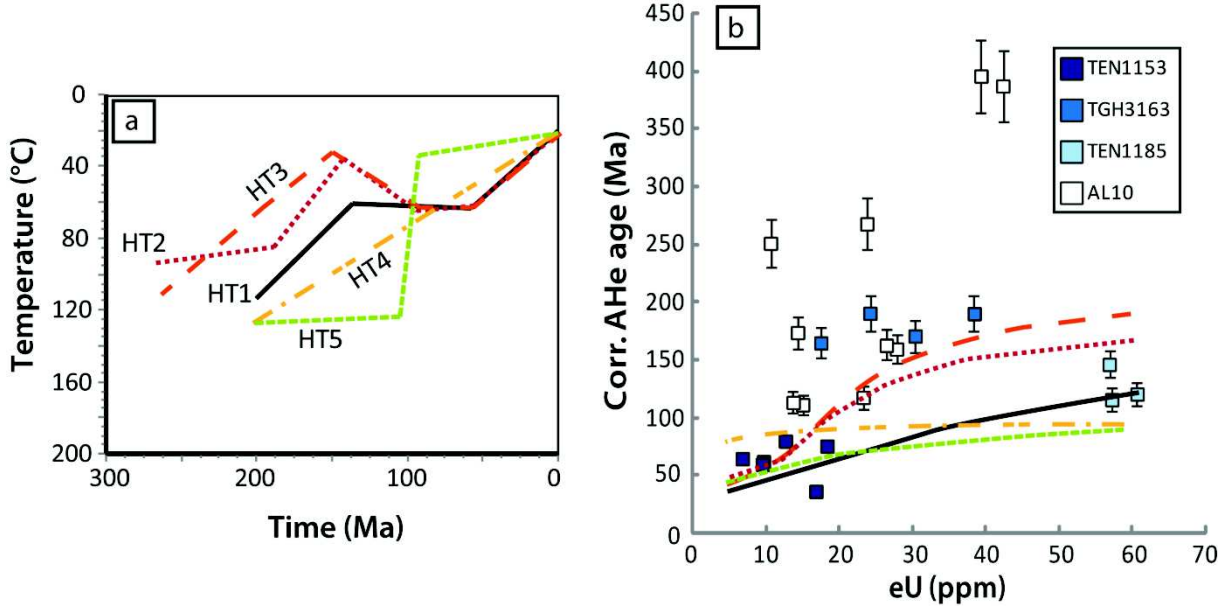


Figure 9

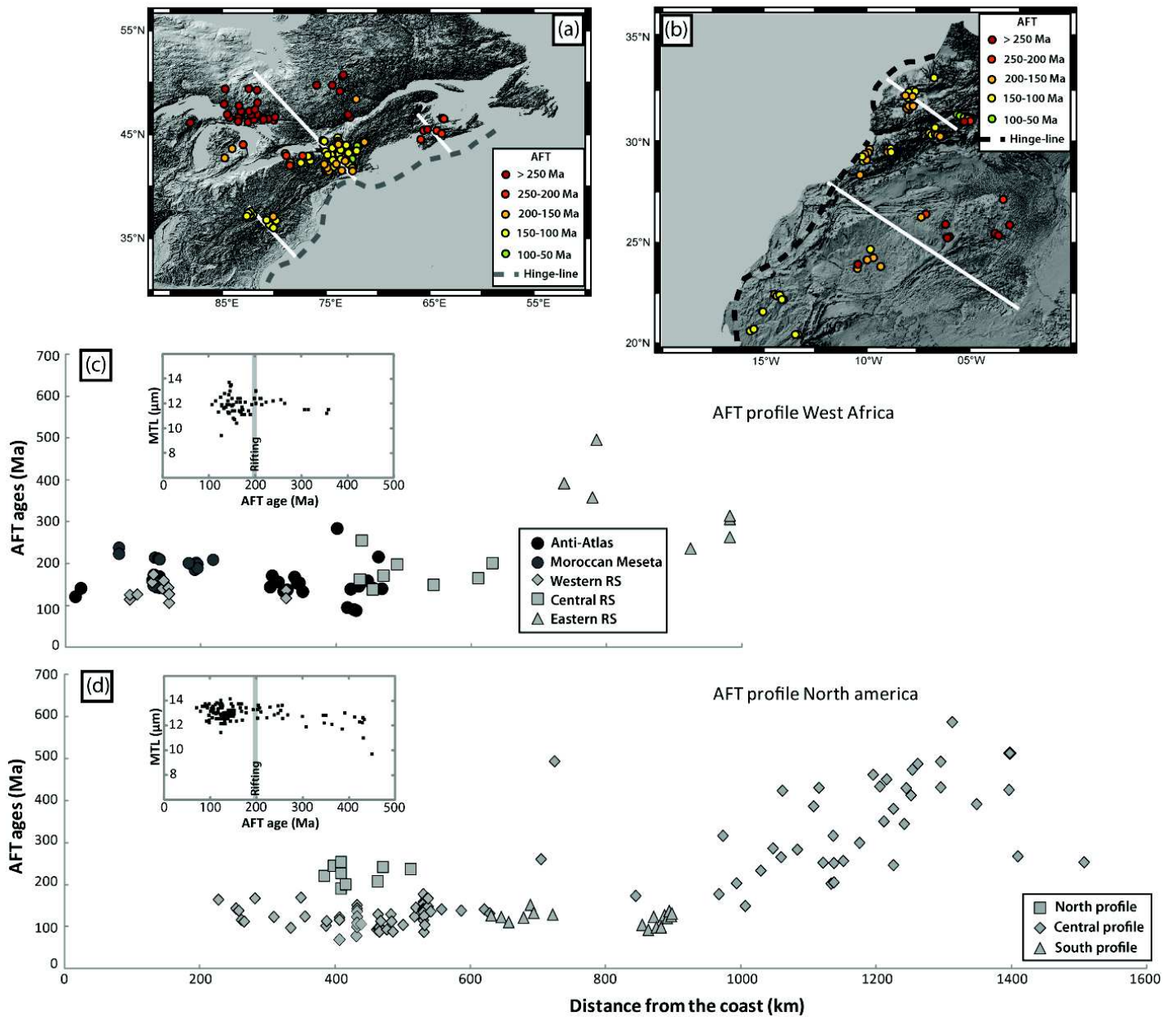


Figure 10

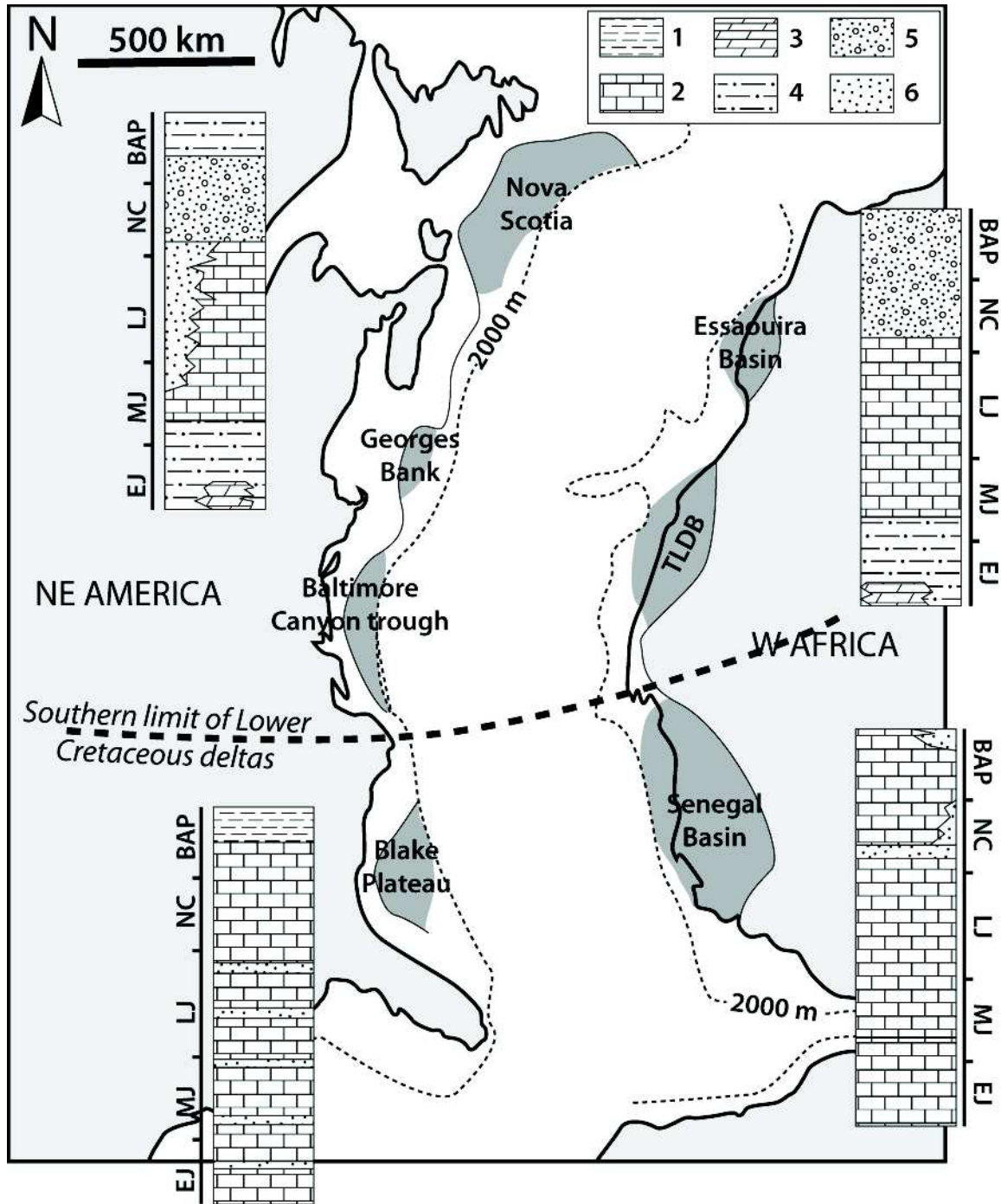


Figure 11

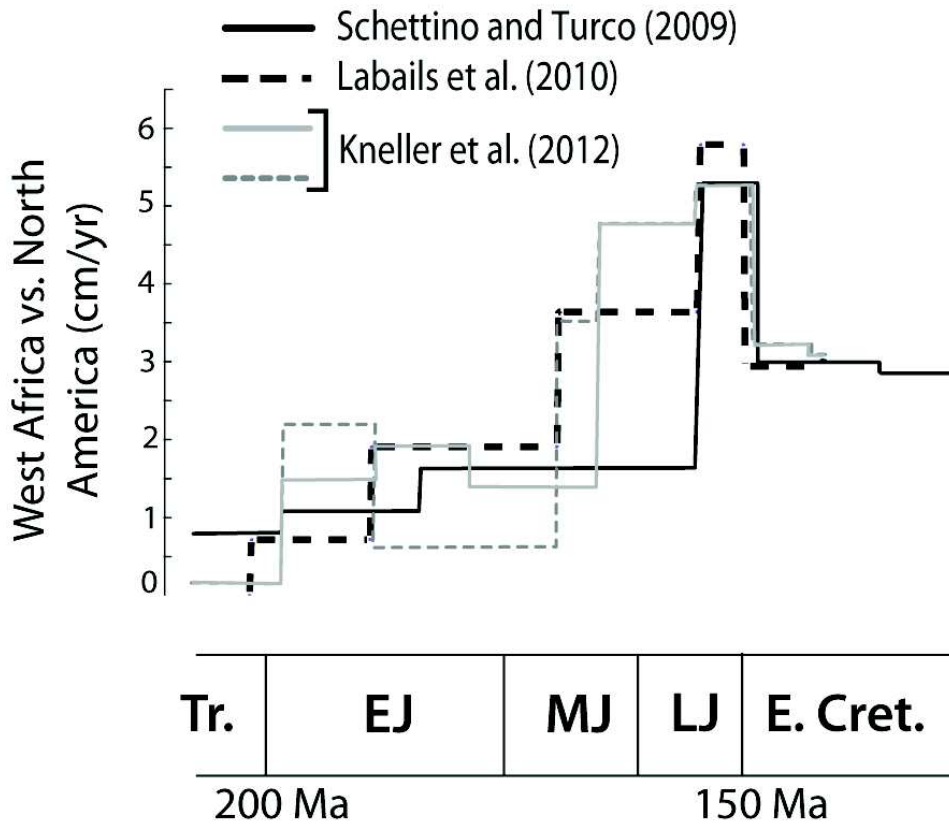
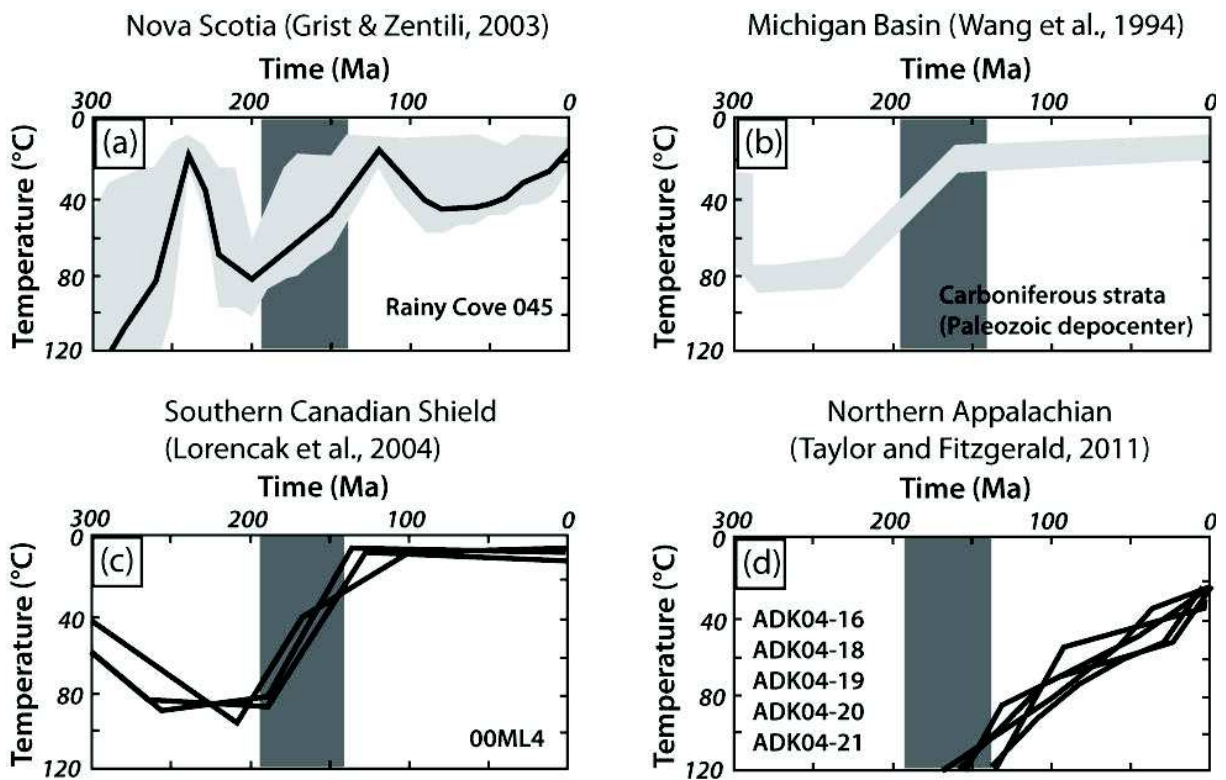


Figure 12



Supplementary Data

Text S1 – Modeling procedure for western RS samples

The thermal modeling for western RS samples is briefly recalled here. The reader is invited to read the extensive description given in Leprêtre et al. (2015).

The modeling of samples of the western RS was done through three steps, given the complexity of the dataset. A first step of inverse modeling was used as an exploratory tool to search the (T, t) space. The stratigraphical constraint given by the unconformity of the Lower Cretaceous deposits and a data-dependent constraint implying samples to be at temperatures higher than 110°C before 200 Ma were incorporated in the modeling to narrow the exploration of the (T, t) space.

Second, representative thermal histories obtained in the first step were discriminated using the forward modeling. They implied further restrictions on the available (T,t) paths that were incorporated as constraints in the third step of the modeling. The last step used inverse modeling with all determined constraints during the early steps to explore the degrees of freedom left to the model to better fit the data.

This three-step procedure led to four major constraints that we re-use here to model the AFT ages of AG167 and AG169 samples: (1) samples were at temperatures higher than 110°C before 200 Ma; (2) samples were near or at the surface during the Early Cretaceous; (3) a necessary reheating step occurred until the beginning of the Late Cretaceous; (4) a subsequent cooling up to 40°C by the end of the Late Cretaceous.

Text S2 – influence of apatite chemistry on the single-grain AHe ages scattering

To investigate the influence of the chemistry on the scattering of the single-grain AHe age, we used the mean thermal paths obtained through thermal modeling for all samples with AHe datasets. With forward modeling, we consider the whole range of Dpar and grain size of single grain within each sample. The grain size range is approximated through the equivalent sphere radius (Rs; see Table 2). The chemistry variations are taken into account through the *rmr0* factor, as defined by Ketcham et al. (2007). An empirical relationship links the Dpar and the *rmr0* through the following equation:

$rmr0 = 0.84 \times [(4.58 - Dpar)/2.98]^{0.21}$, the *rmr0* being used as the chemical determinant for the forward modeling with HeFTy for our tests.

We tested each final thermal path in forward modeling, varying the values of *rmr0* and Rs. For an eU range, we then reported the obtained AHe age-eU relationship for the four couple (*rmr0*; Rs) tested (Fig. S17). One can see on figure S17 that generally, the single-grain AHe ages scattering can simply depend on these two parameters. Some out-of-trend replicates need others explanations, like the shape of broken apatite crystals (Brown et al., 2013) or contamination (Gautheron et al., 2012).

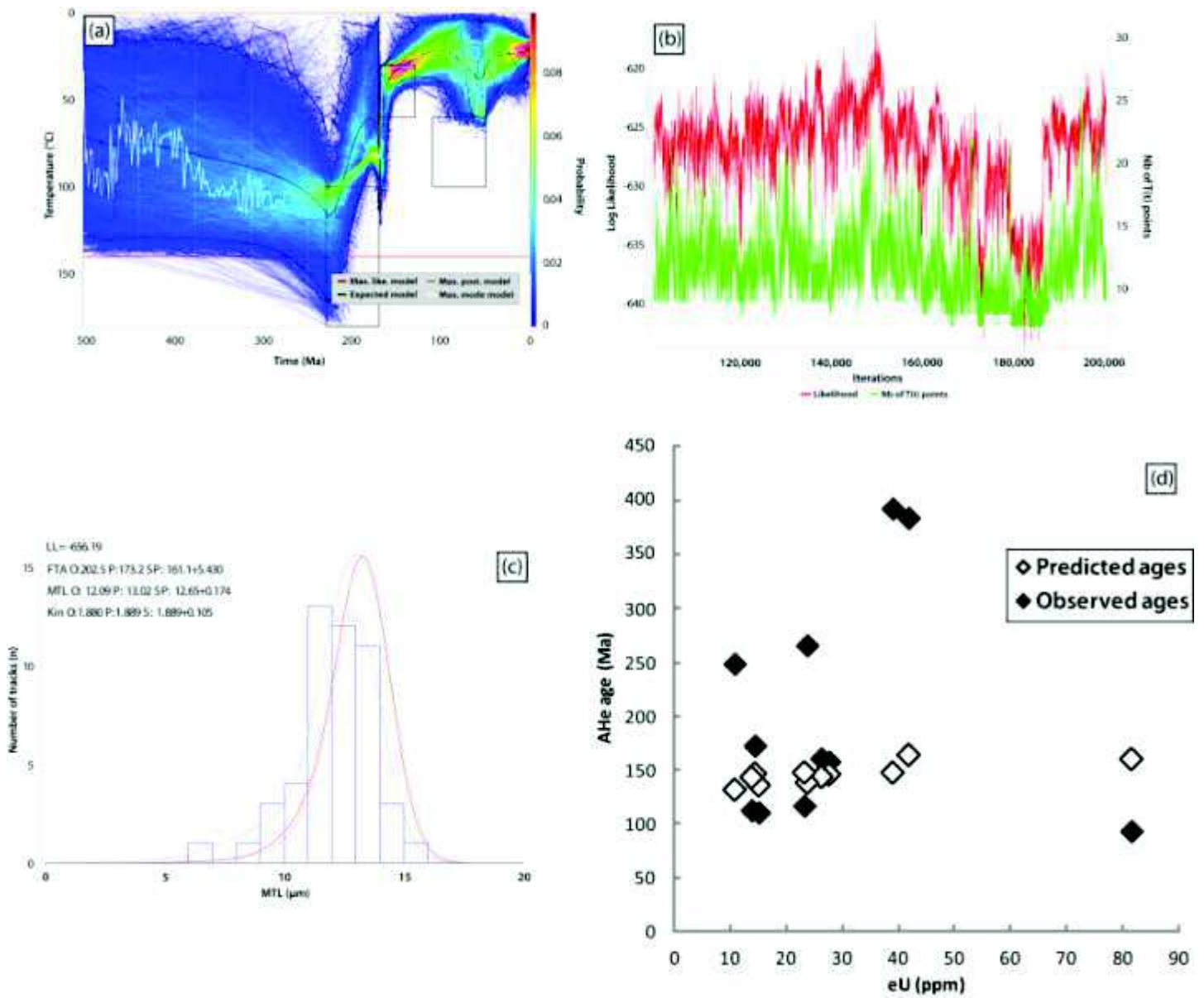


Figure S1: Thermal modeling of AL10 sample with all single-grain AHe ages. The figure must be compared with figure S12. It shows the instabilities produced by the use of anomalous replicates. . (a) Thermal history with different outputs (see details in Gallagher, 2012); (b) Evolution of the LL and the number of T(t) points during the post-burn-in phase; (c) Predicted parameters for the expected model (black line in (a)). In red line is the predicted length distribution (superimposed on blue histogram in other samples). LL: LogLikelihood; FTA: fission track age; MTL: mean track length; Kin: Dpar; O: observed; P: predicted.

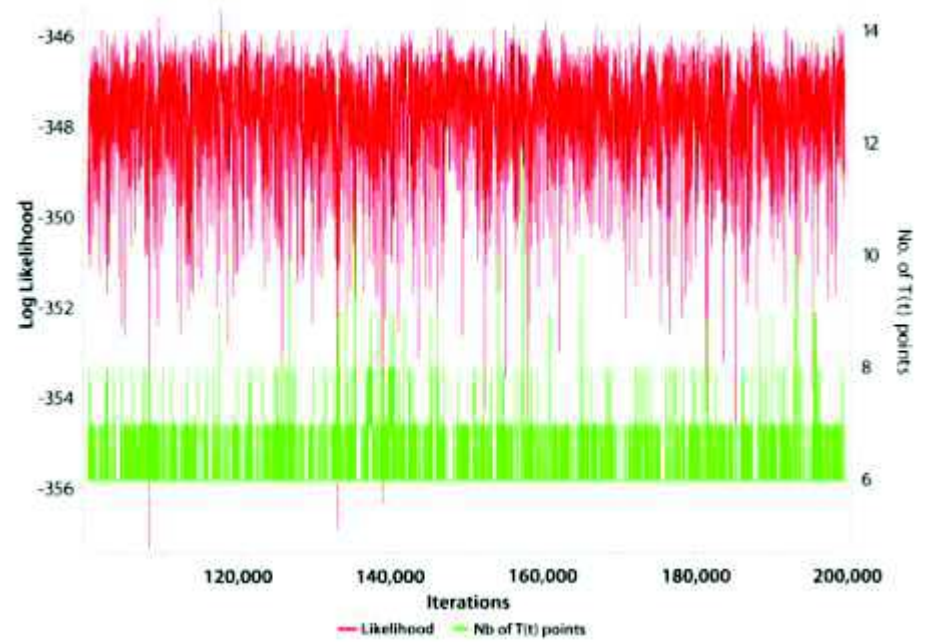
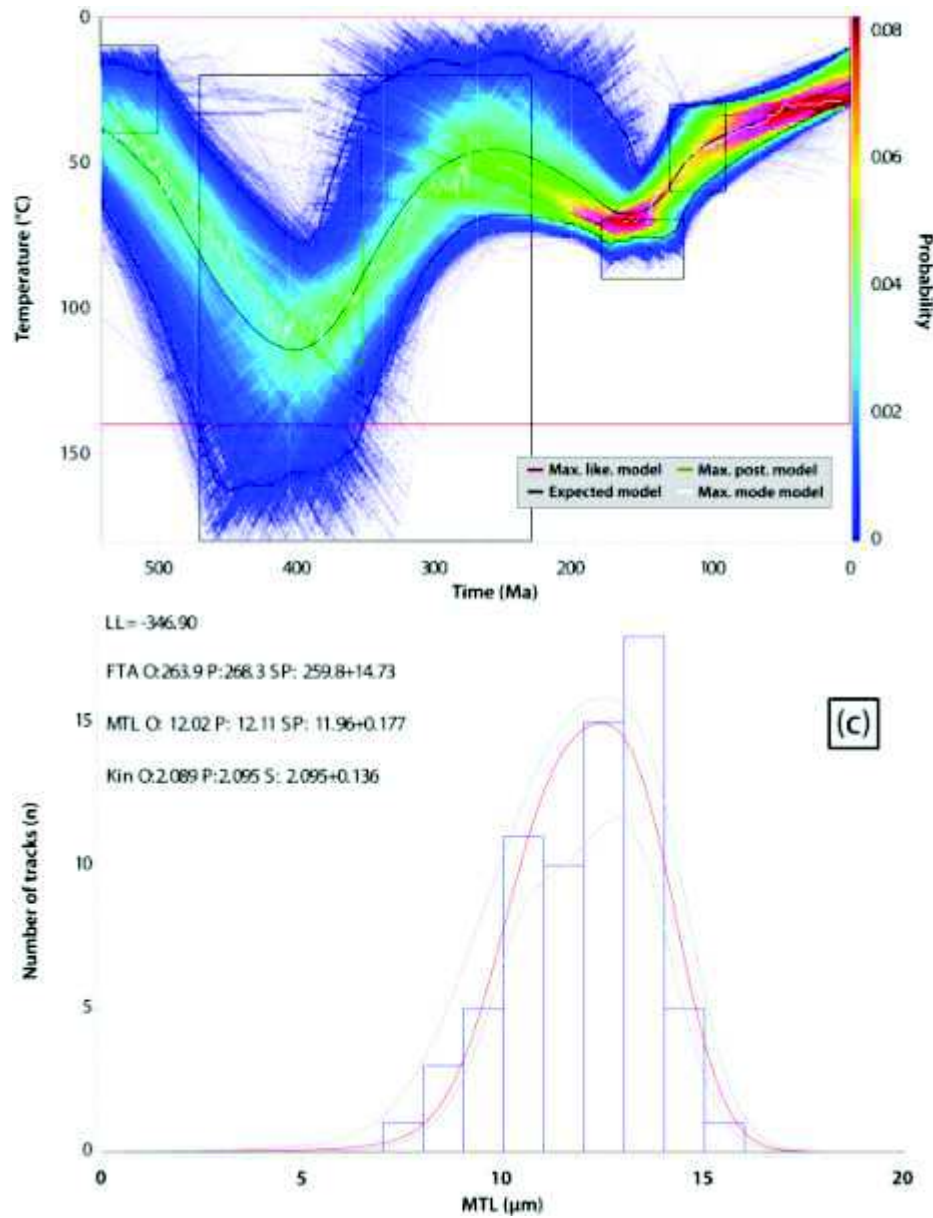


Figure S2: Thermal modeling of CH2 sample. (a) Thermal history with different outputs (see details in Gallagher, 2012); (b) Evolution of the LL and the number of T(t) points during the post-burn-in phase; (c) Predicted parameters for the expected model (black line in (a)). In red line is the predicted length distribution (superimposed on blue histogram in other samples). LL: LogLikelihood; FTA: fission track age; MTL: mean track length; Kin: Dpar; O: observed; P: predicted;

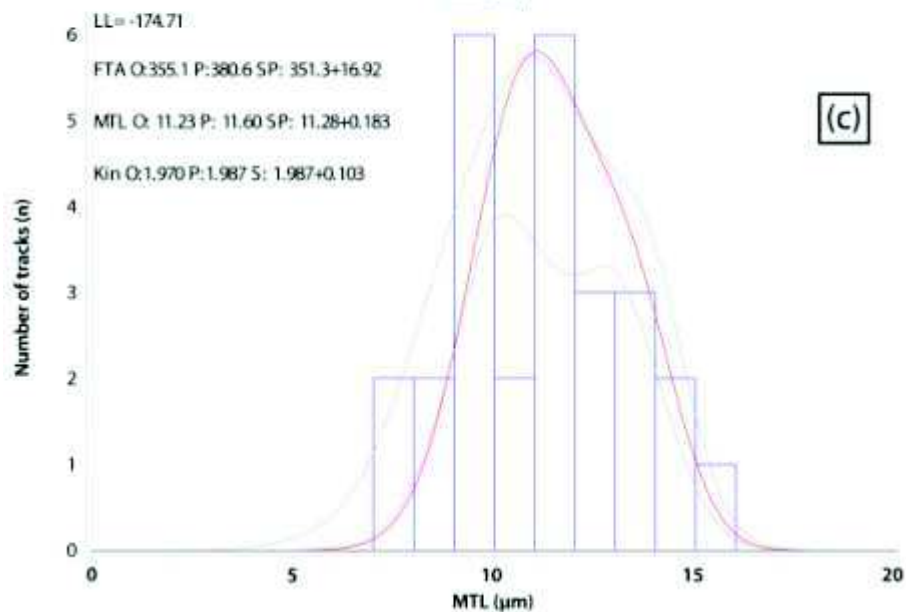
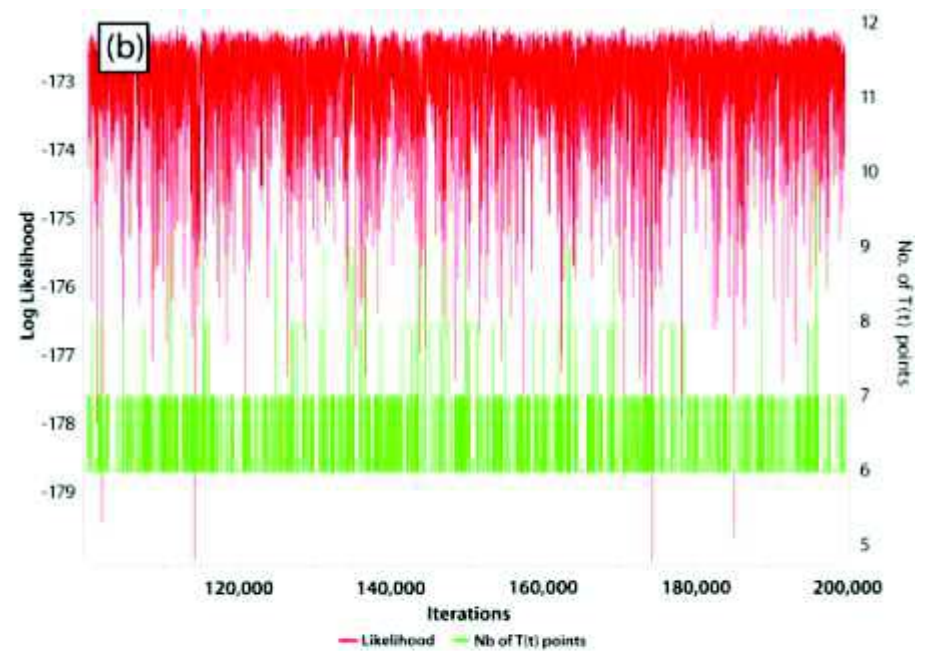
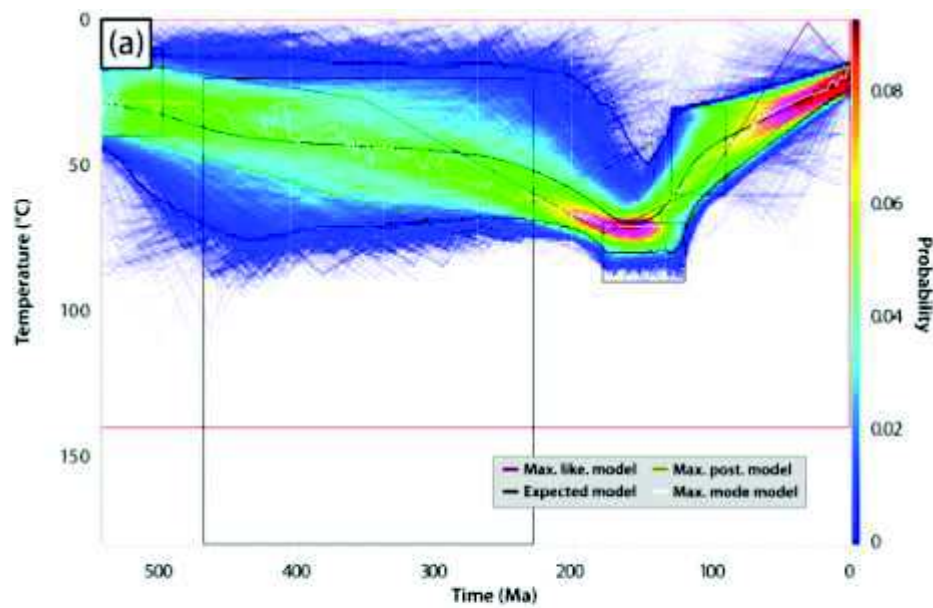


Figure S3: Inverse modeling for samples DEG6. Same legend as in figure S2.

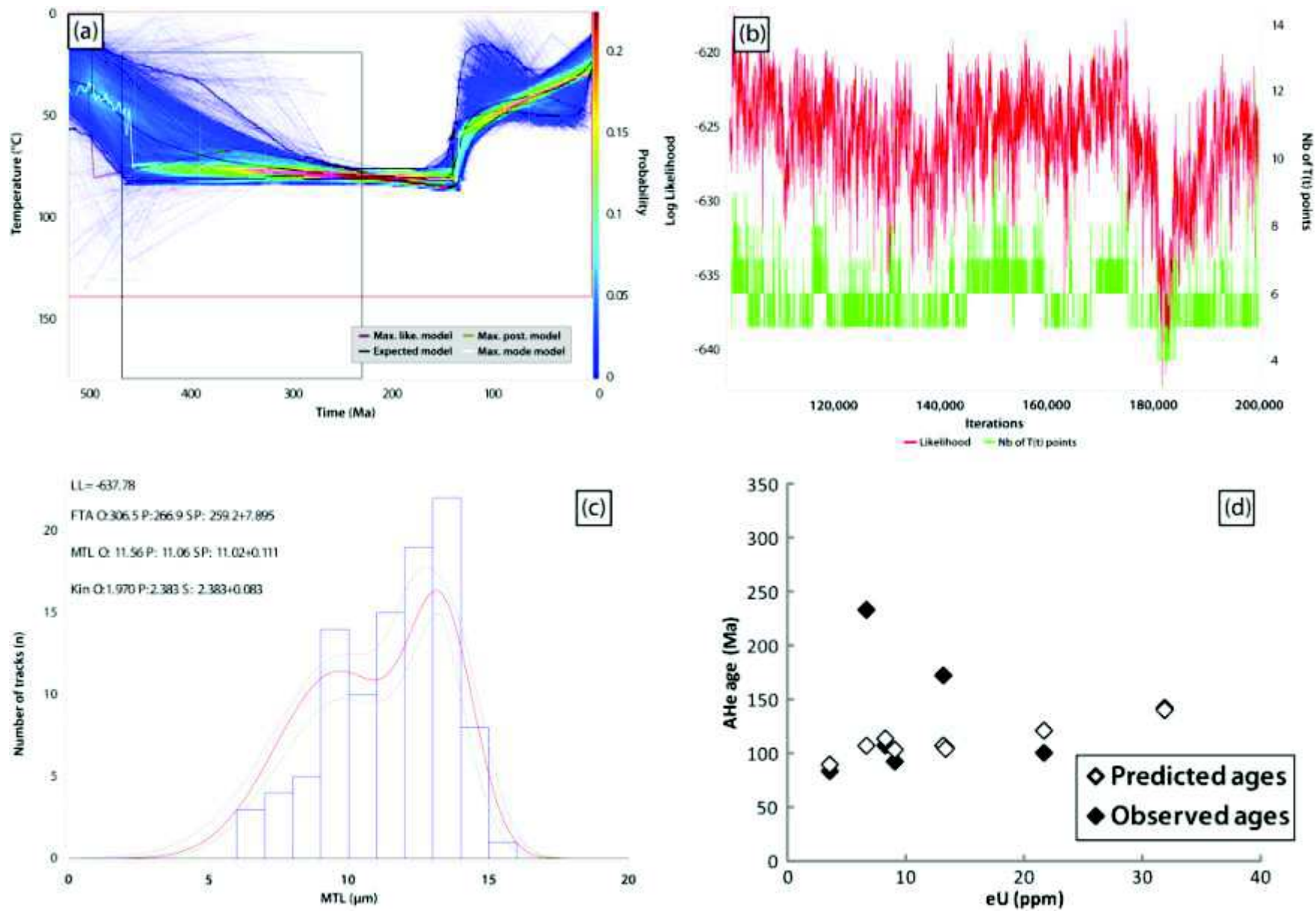


Figure S4: Inverse modeling for sample CH1. Same legend as in figure S2. (d) observed vs. predicted AHe ages.

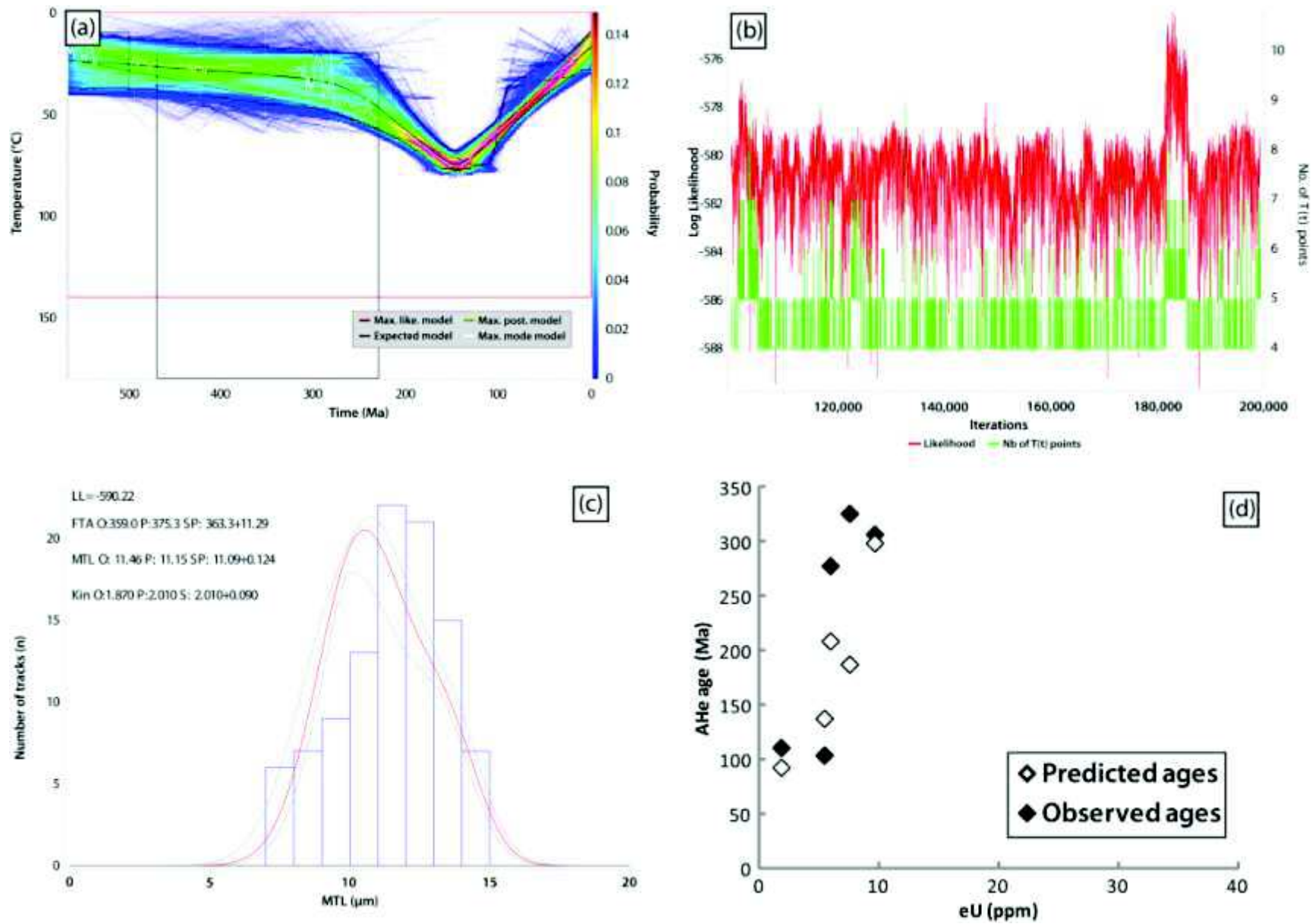


Figure S5: Inverse modeling for sample CH3. Same legend as in figures S2 and S4.

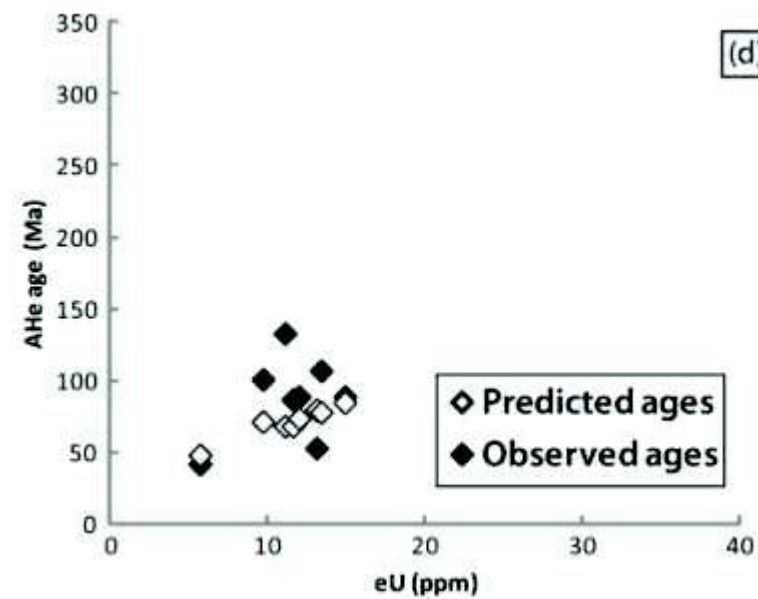
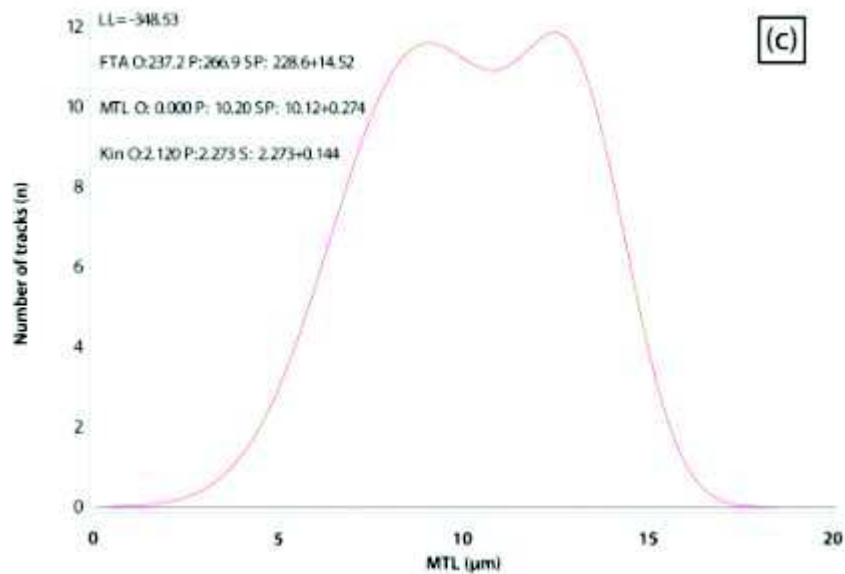
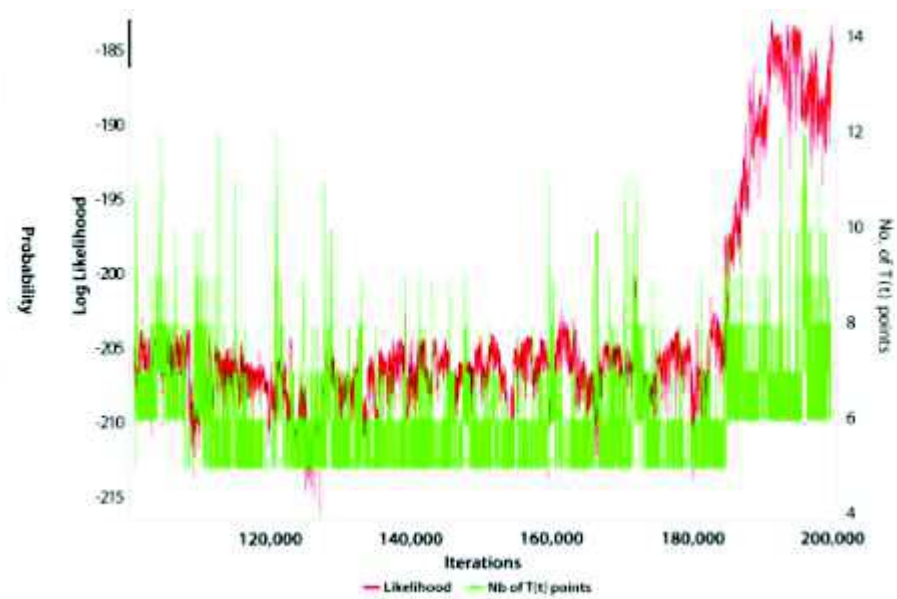
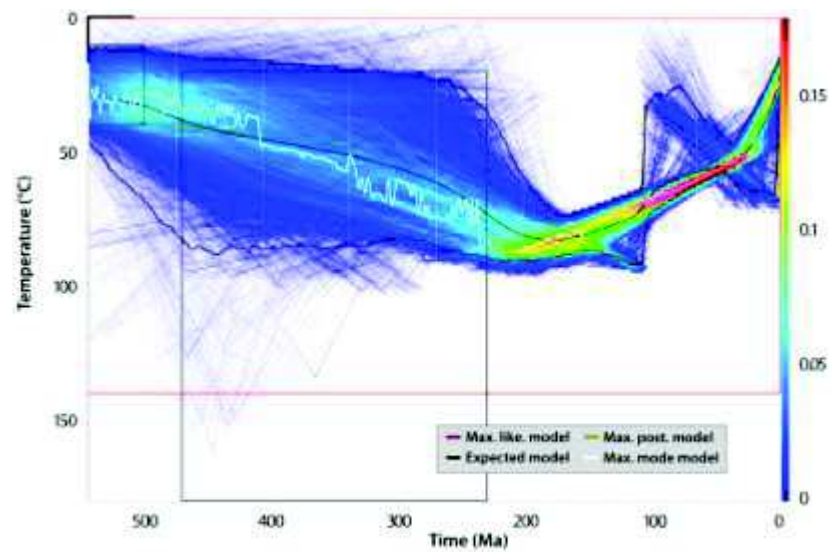


Figure S6: Inverse modeling for sample TL3. Same legend as in figures S2 and S4.

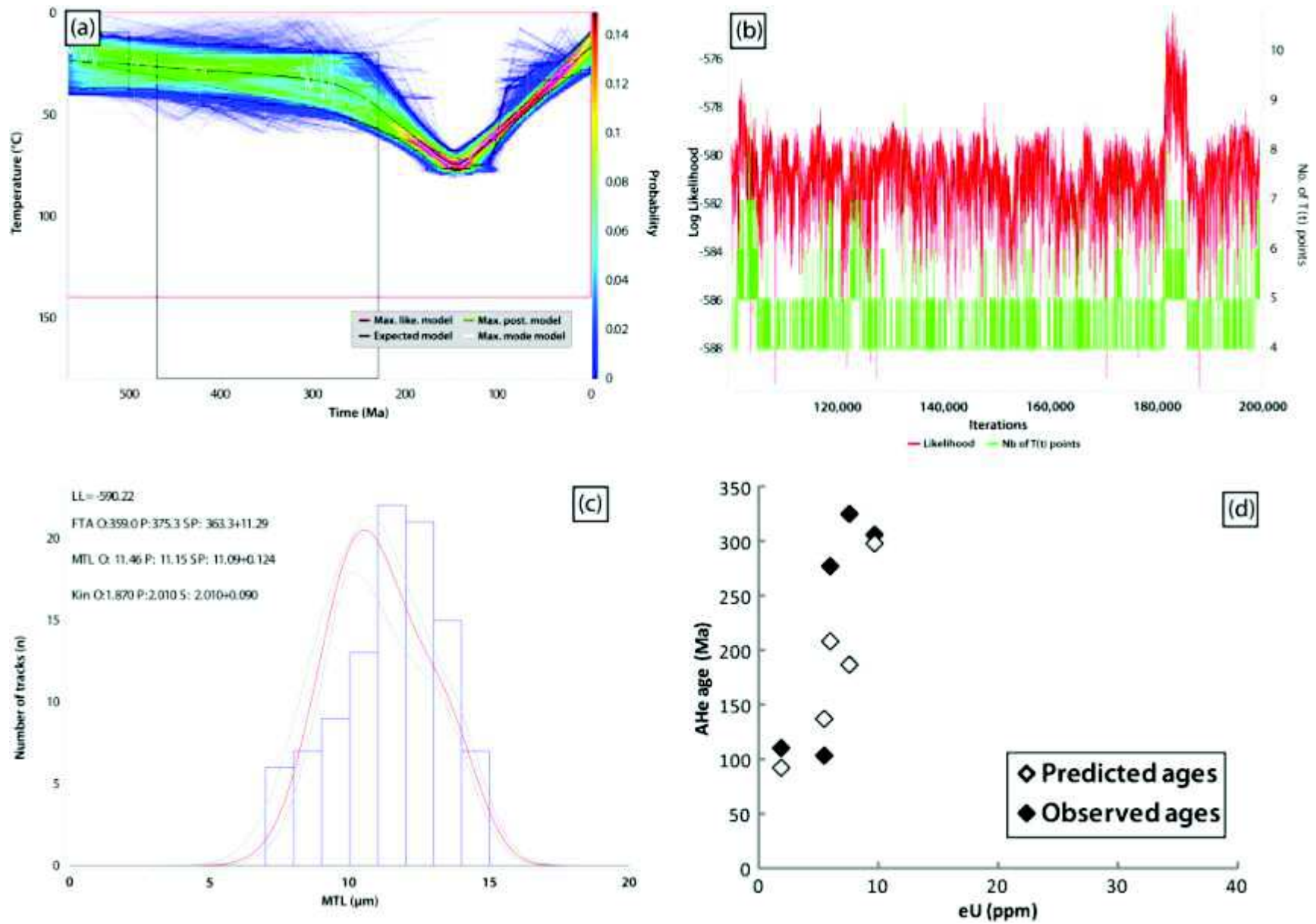


Figure S7: Inverse modeling for sample GH3. Same legend as in figures S2 and S4.

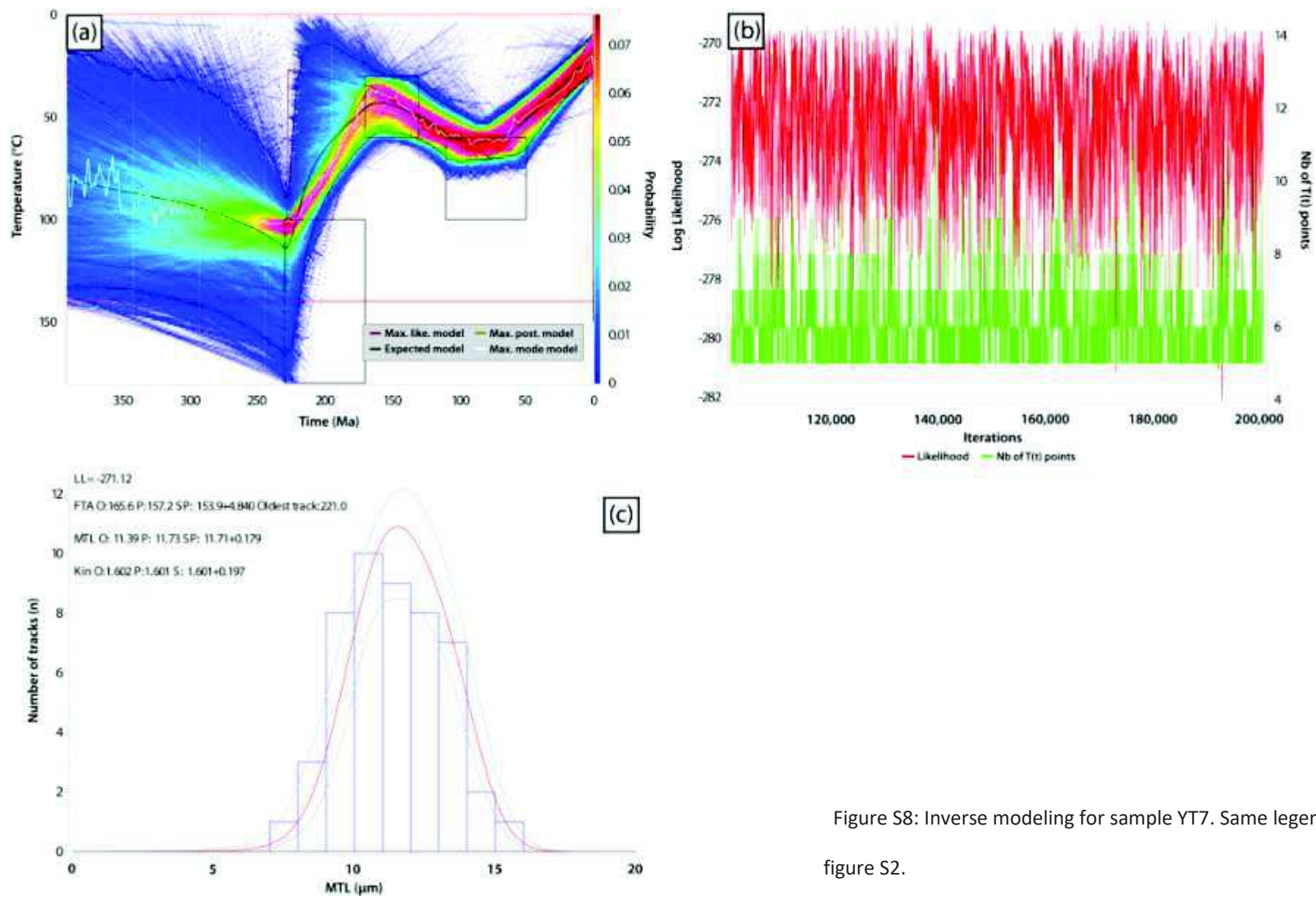


Figure S8: Inverse modeling for sample YT7. Same legend as in figure S2.

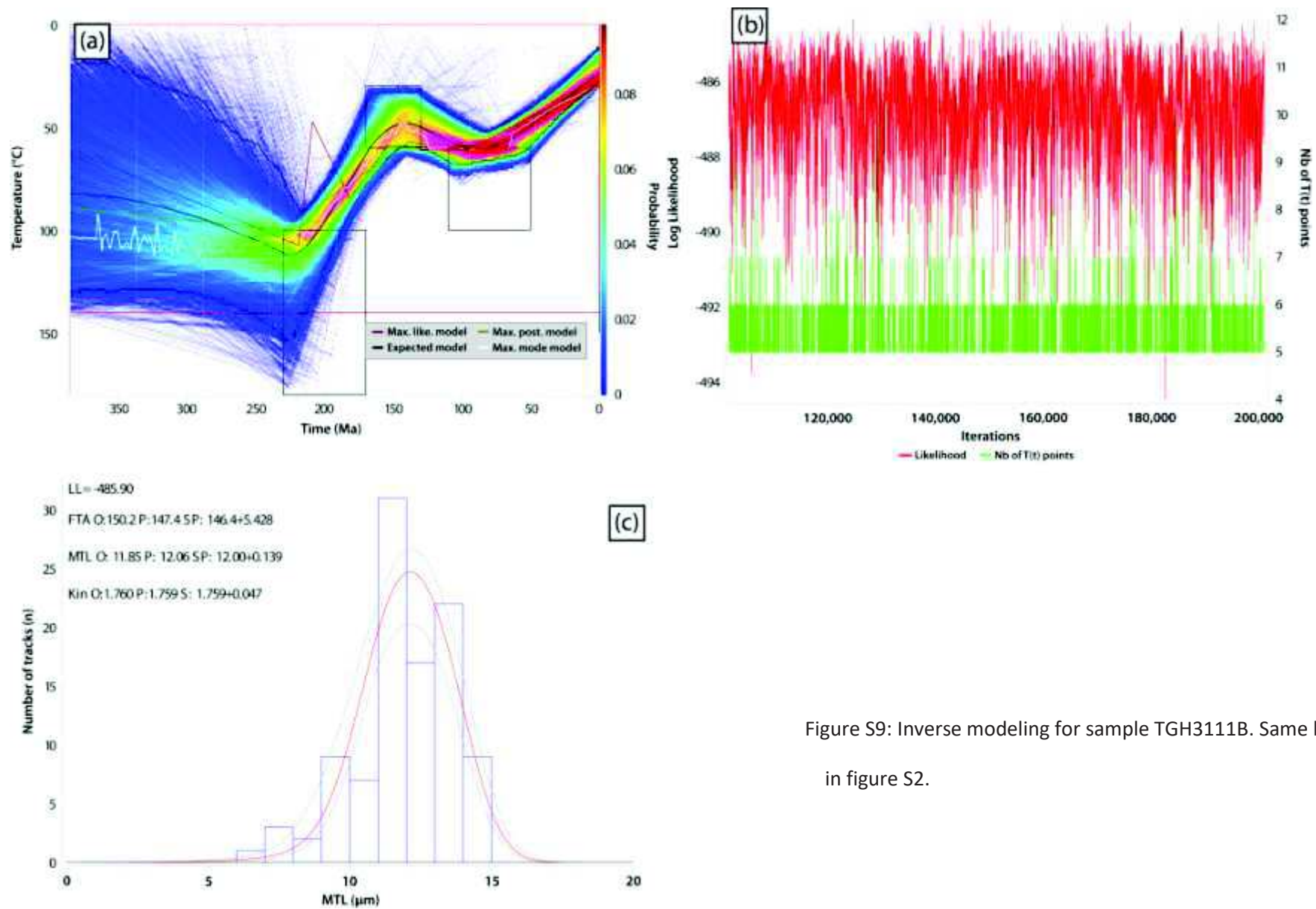


Figure S9: Inverse modeling for sample TGH3111B. Same legend as in figure S2.

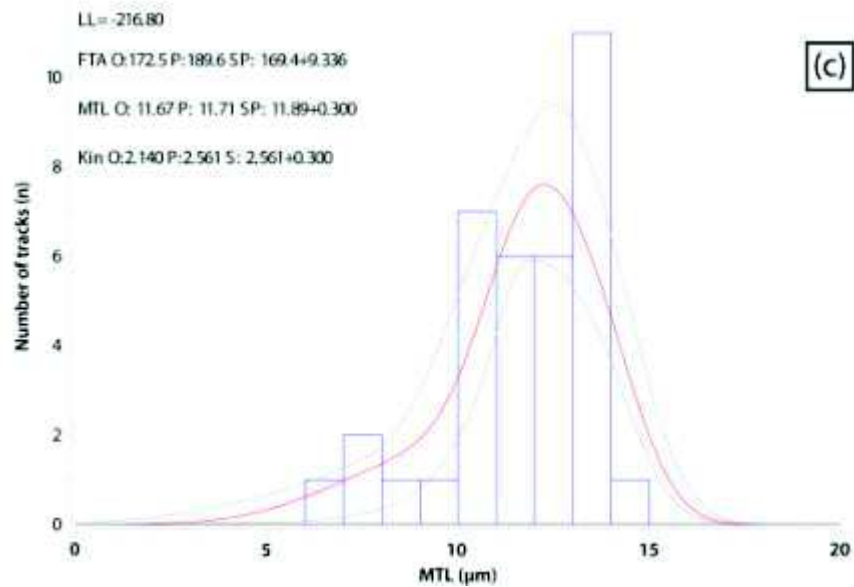
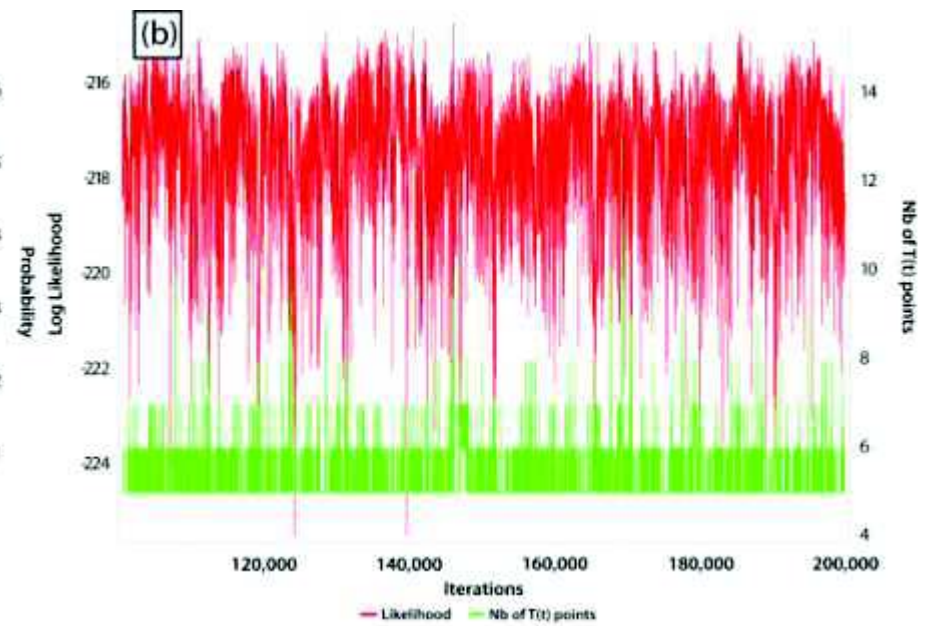
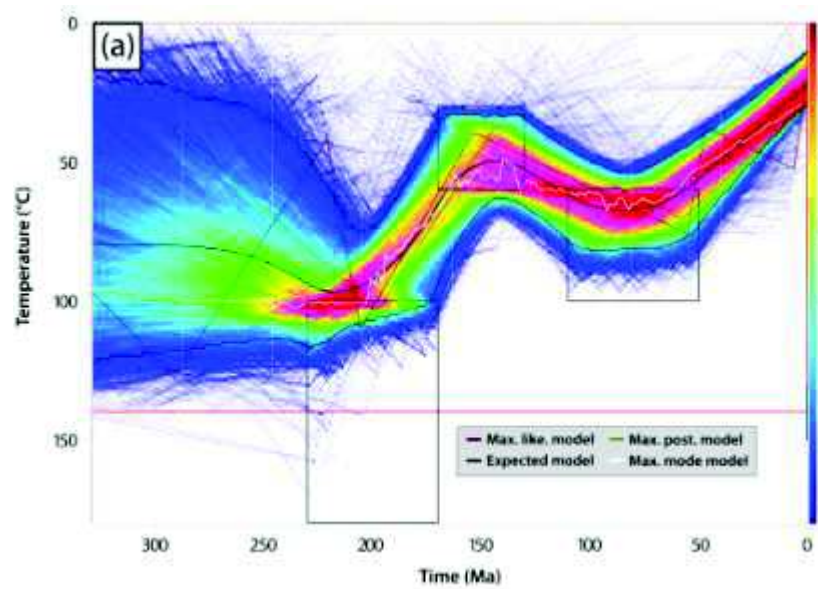


Figure S10: Inverse modeling for sample TEN4065. Same legend as in figure S2.

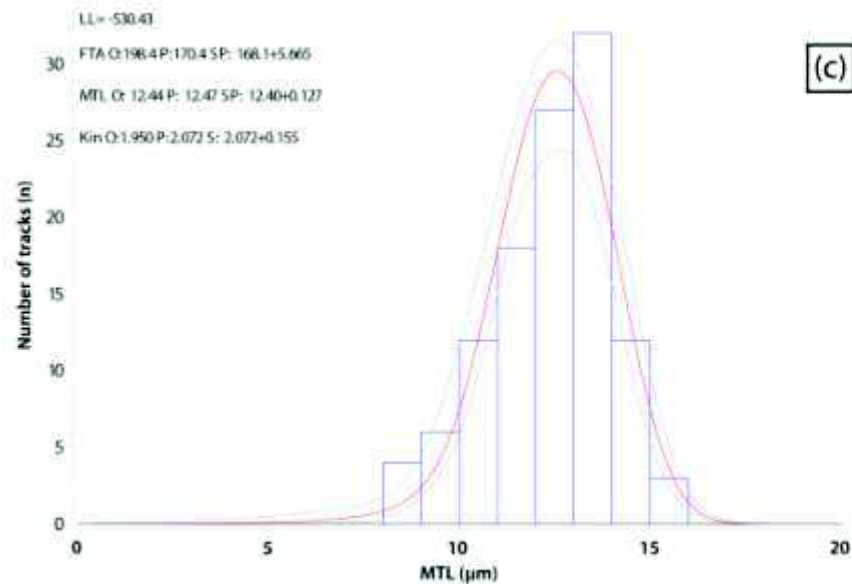
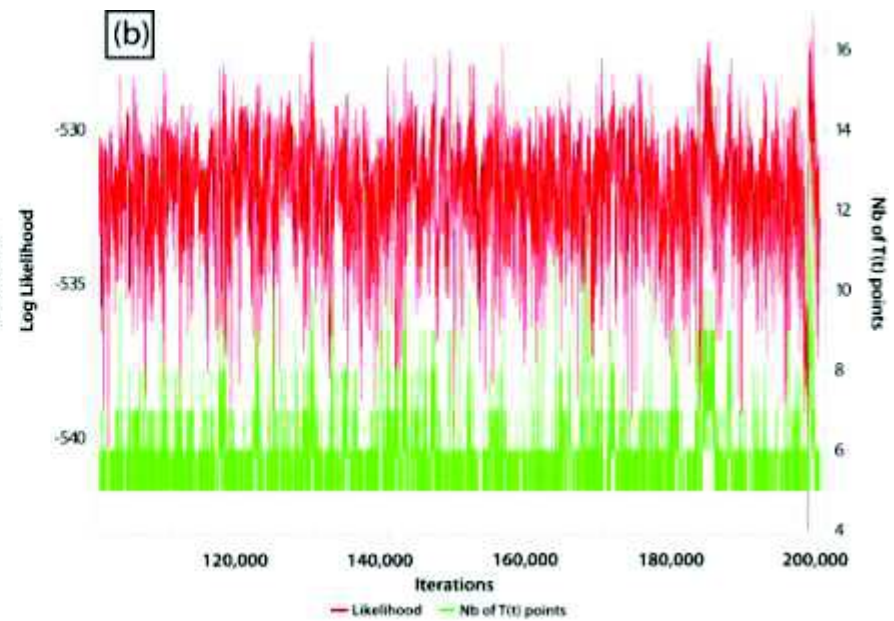
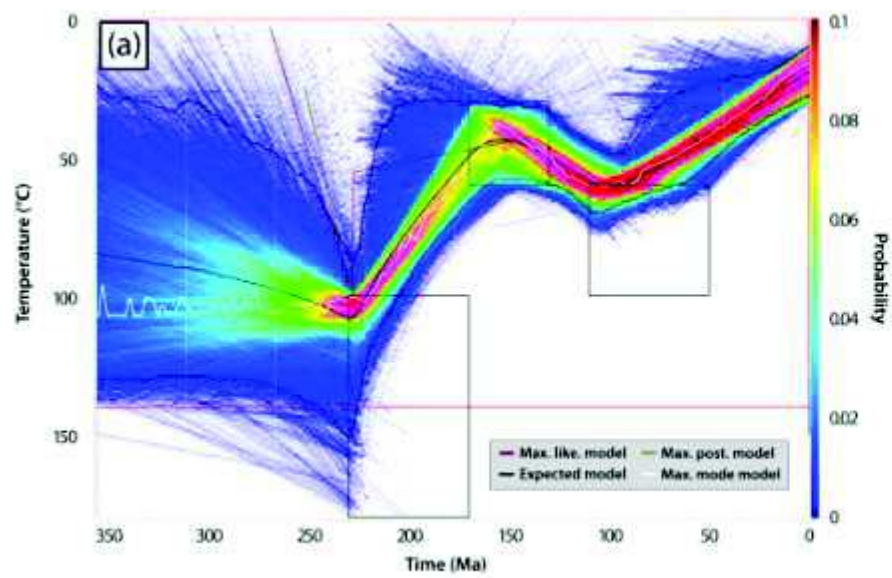


Figure S11: Inverse modeling for sample TGH4072A. Same legend as in figure S2.

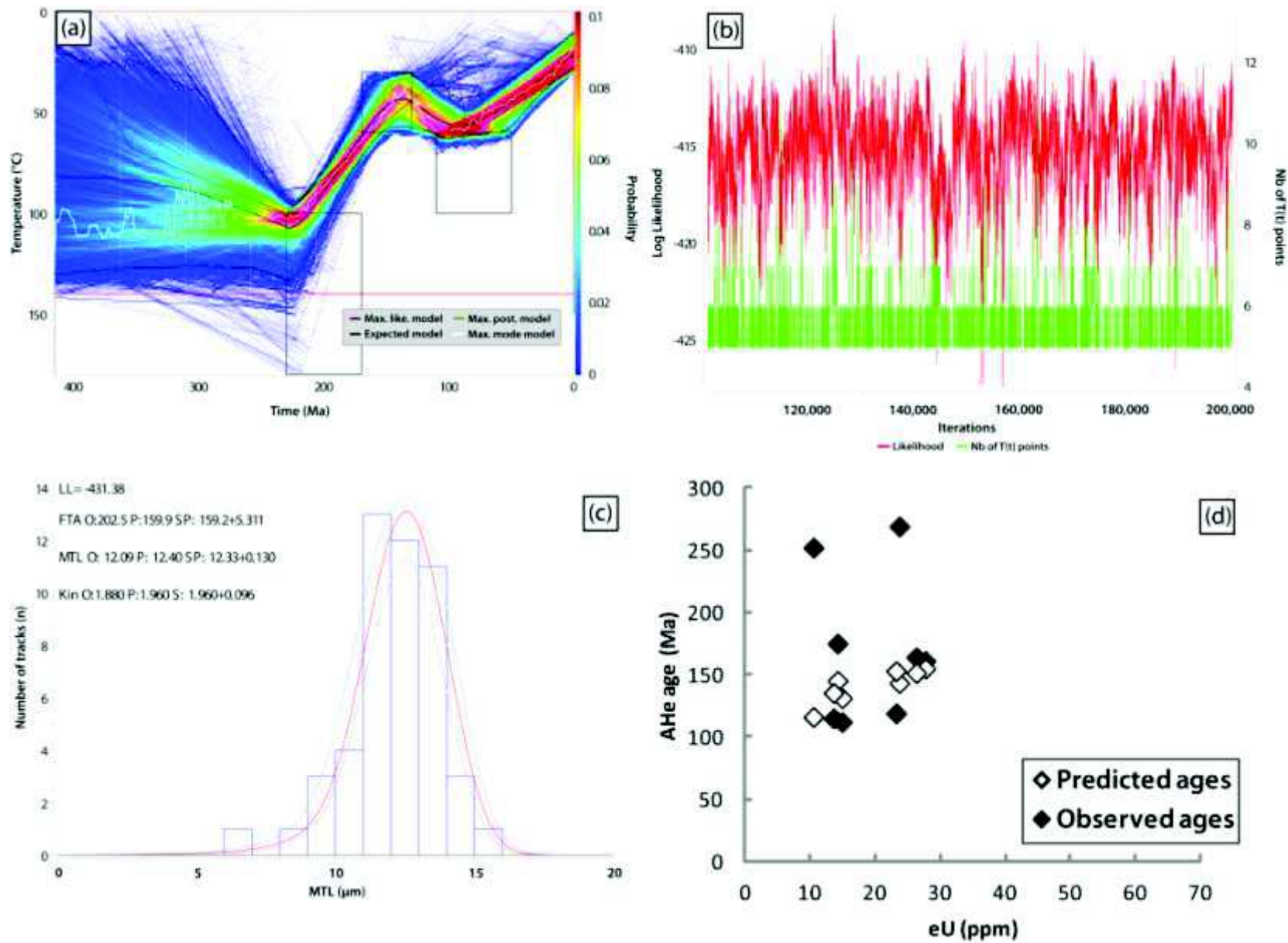


Figure S12: Inverse modeling for sample AL10. Same legend as in figures S2 and S4.

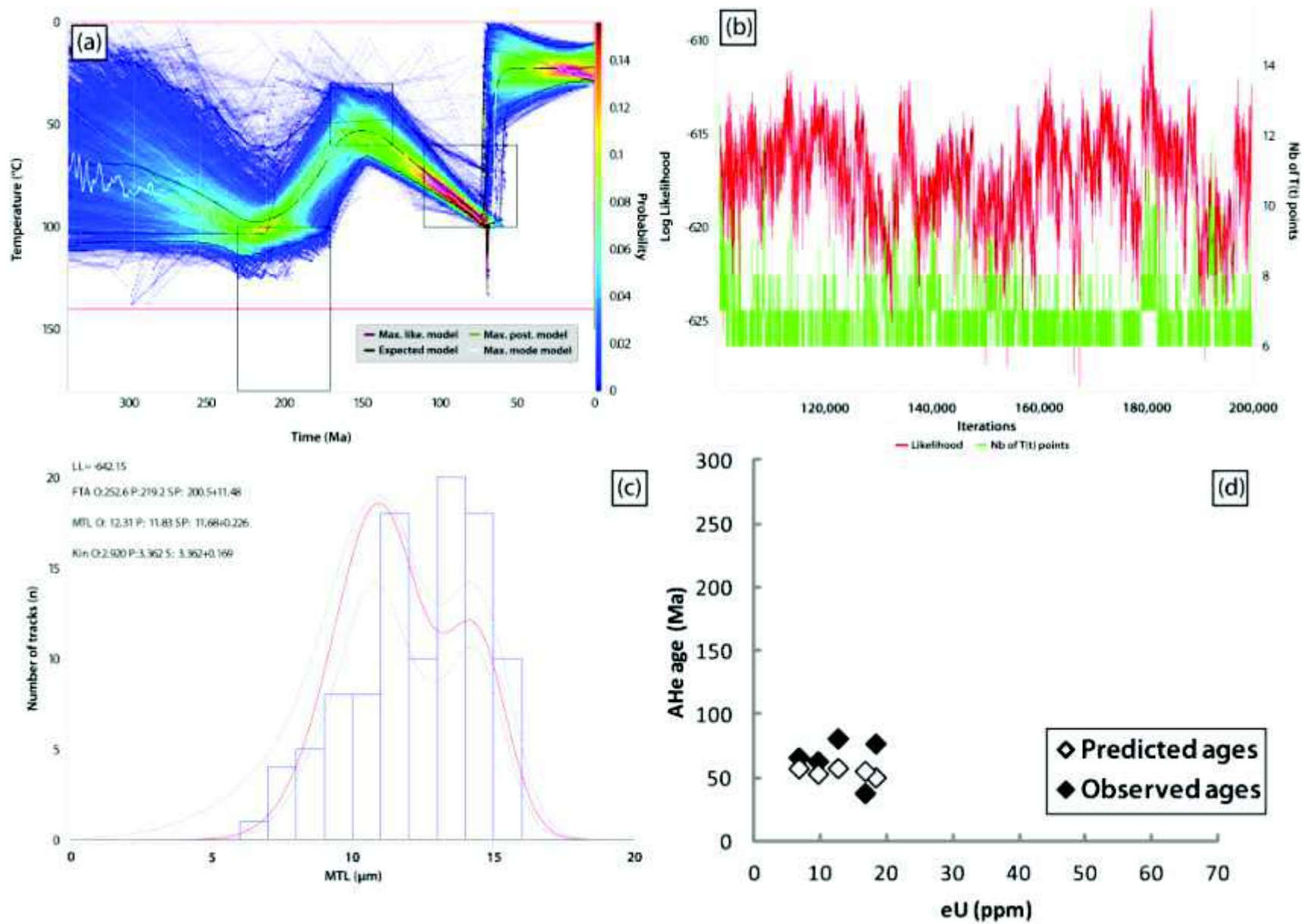


Figure S13: Inverse modeling for sample TEN153. Same legend as in figures S2 and S4.

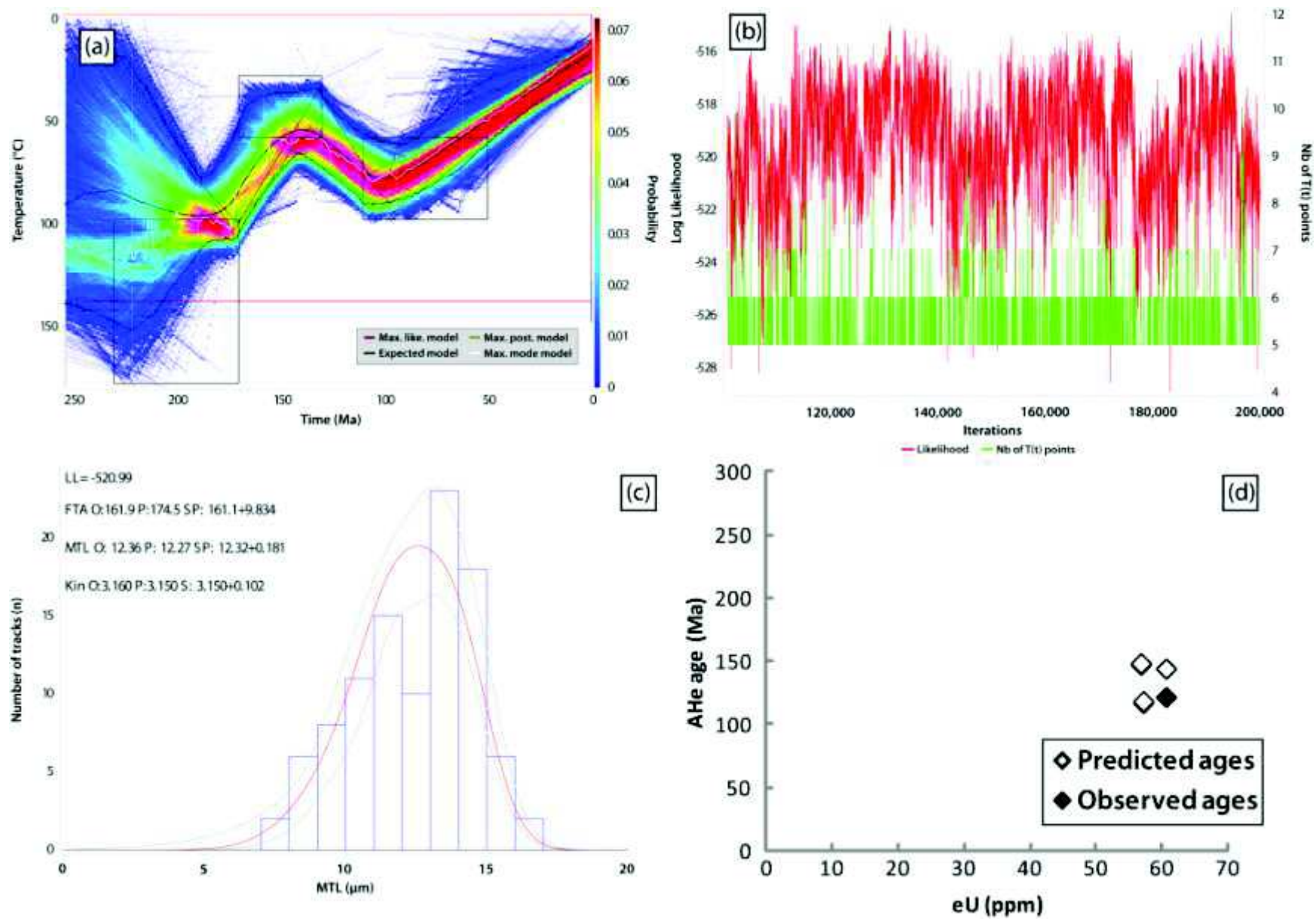


Figure S14: Inverse modeling for samples TEN1185. Same legend as in figures S2 and S4.

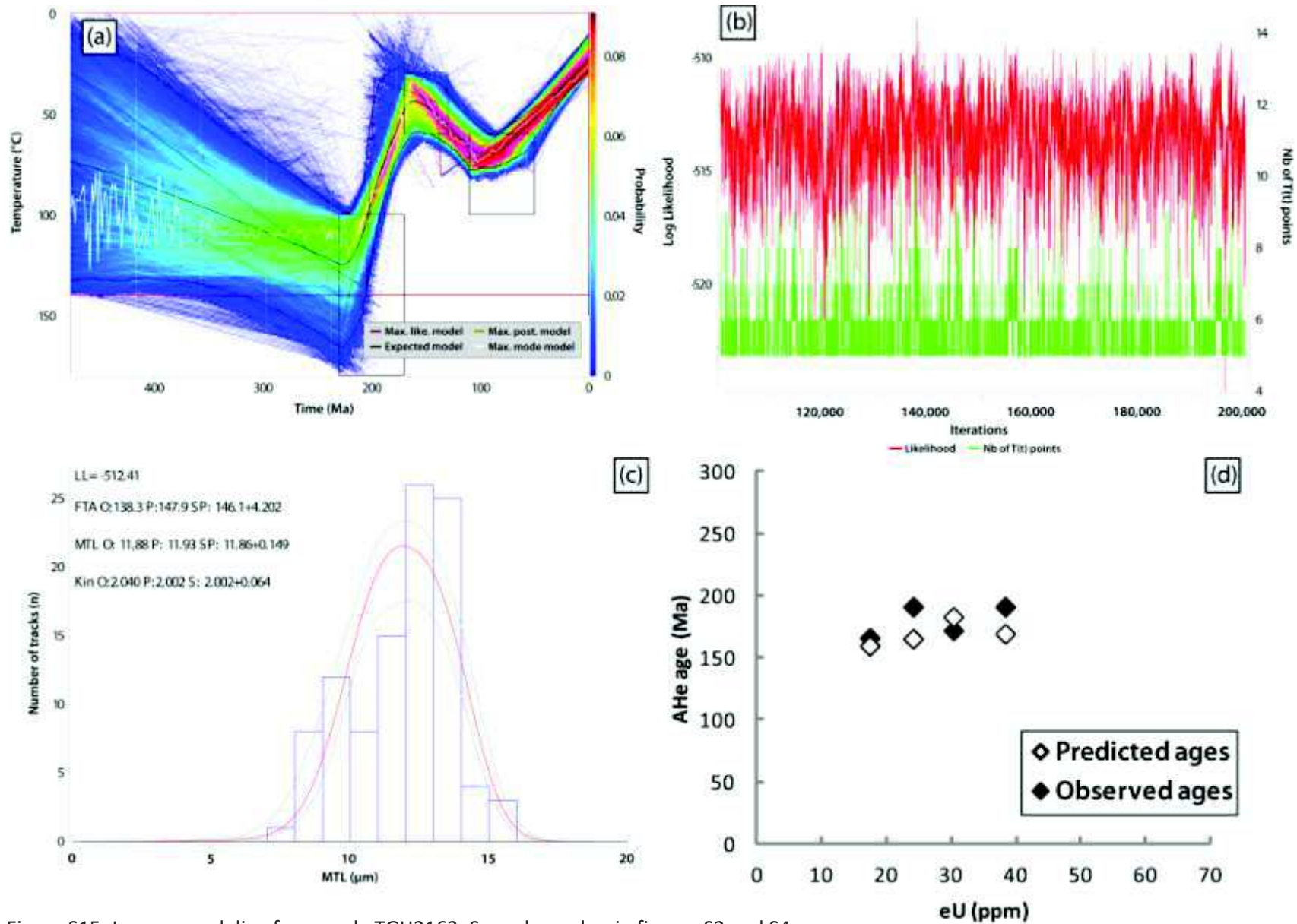


Figure S15: Inverse modeling for sample TGH3163. Same legend as in figures S2 and S4.

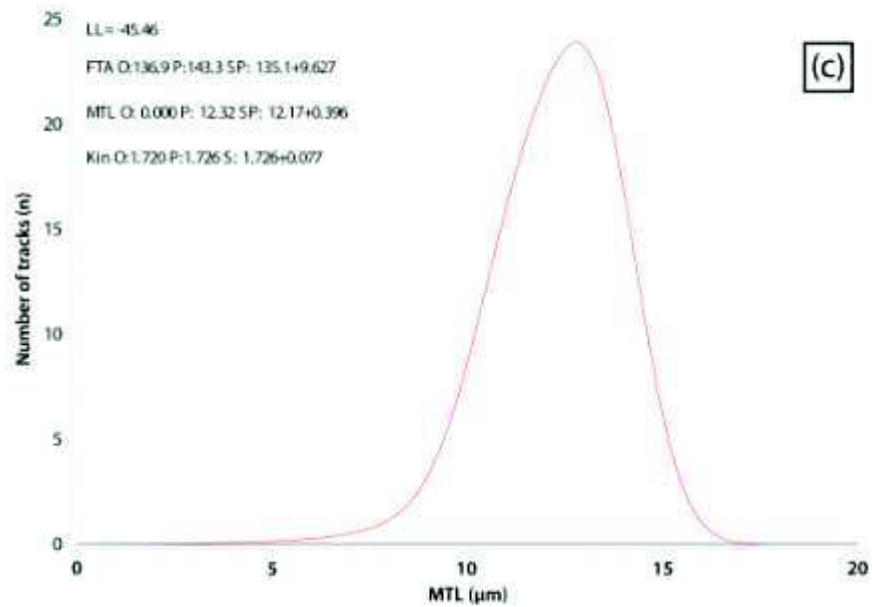
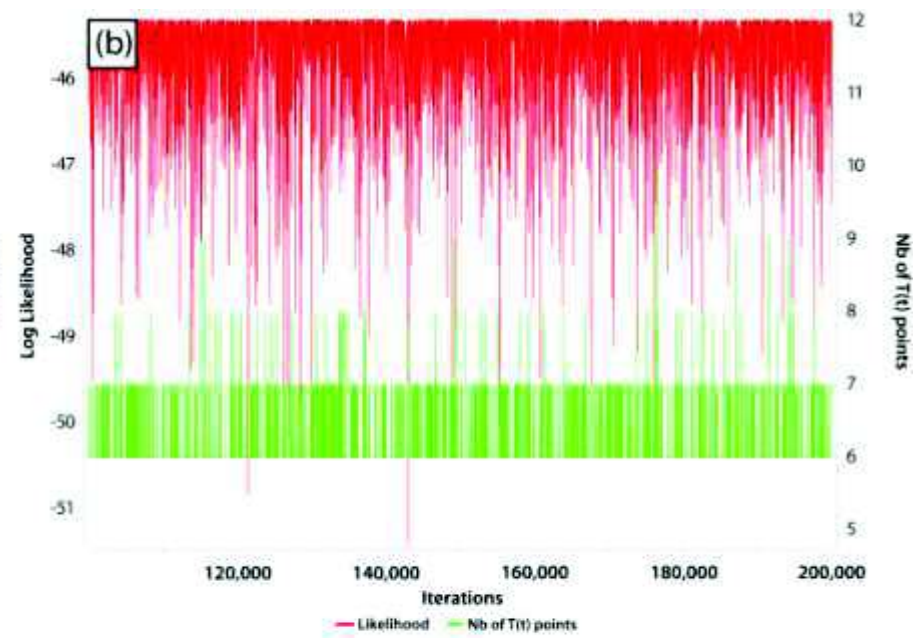
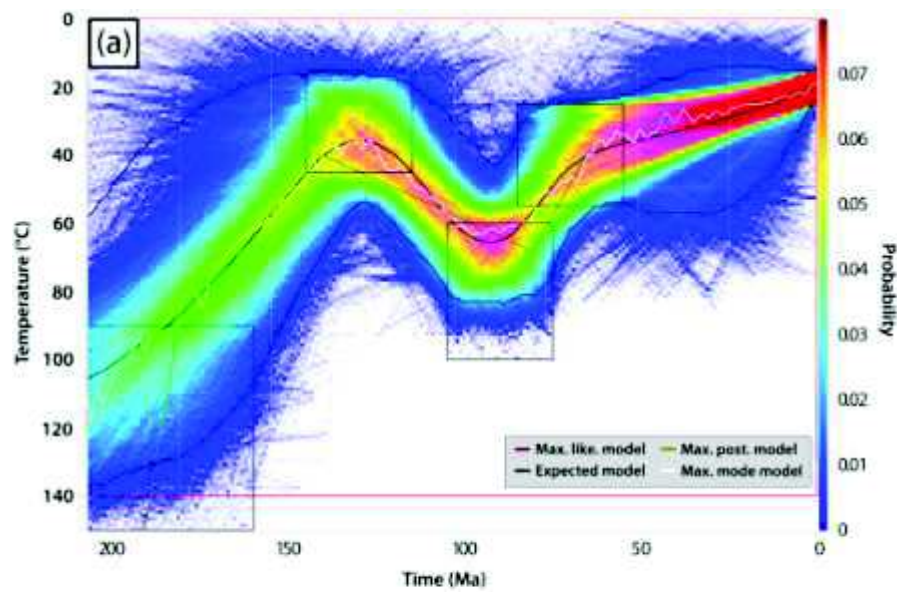


Figure S16: Inverse modeling for sample AG167. Same legend as in figure S2.

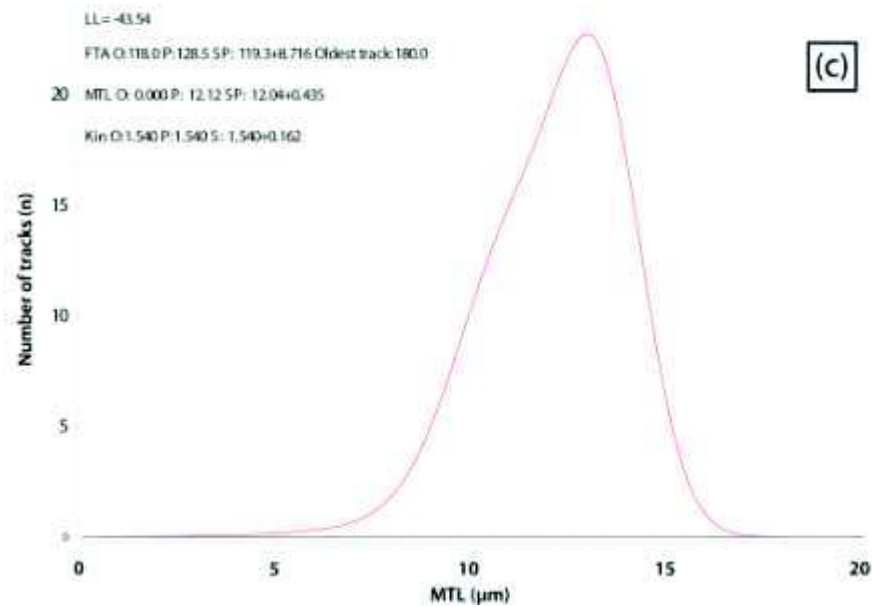
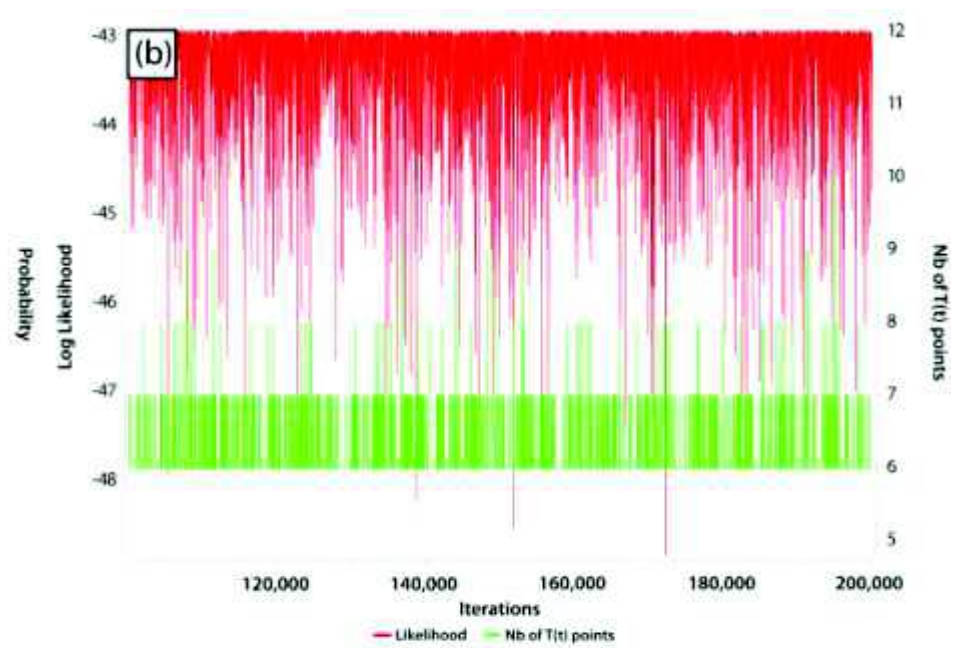
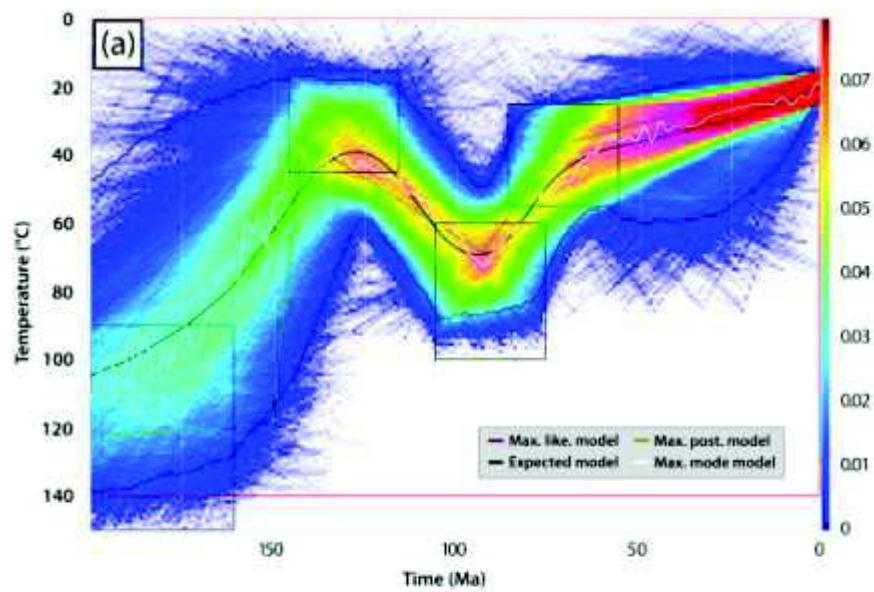


Figure S17: Inverse modeling for sample AG169. Same legend as in figure S2.

Figure S18: Compositional chemical variations in apatites

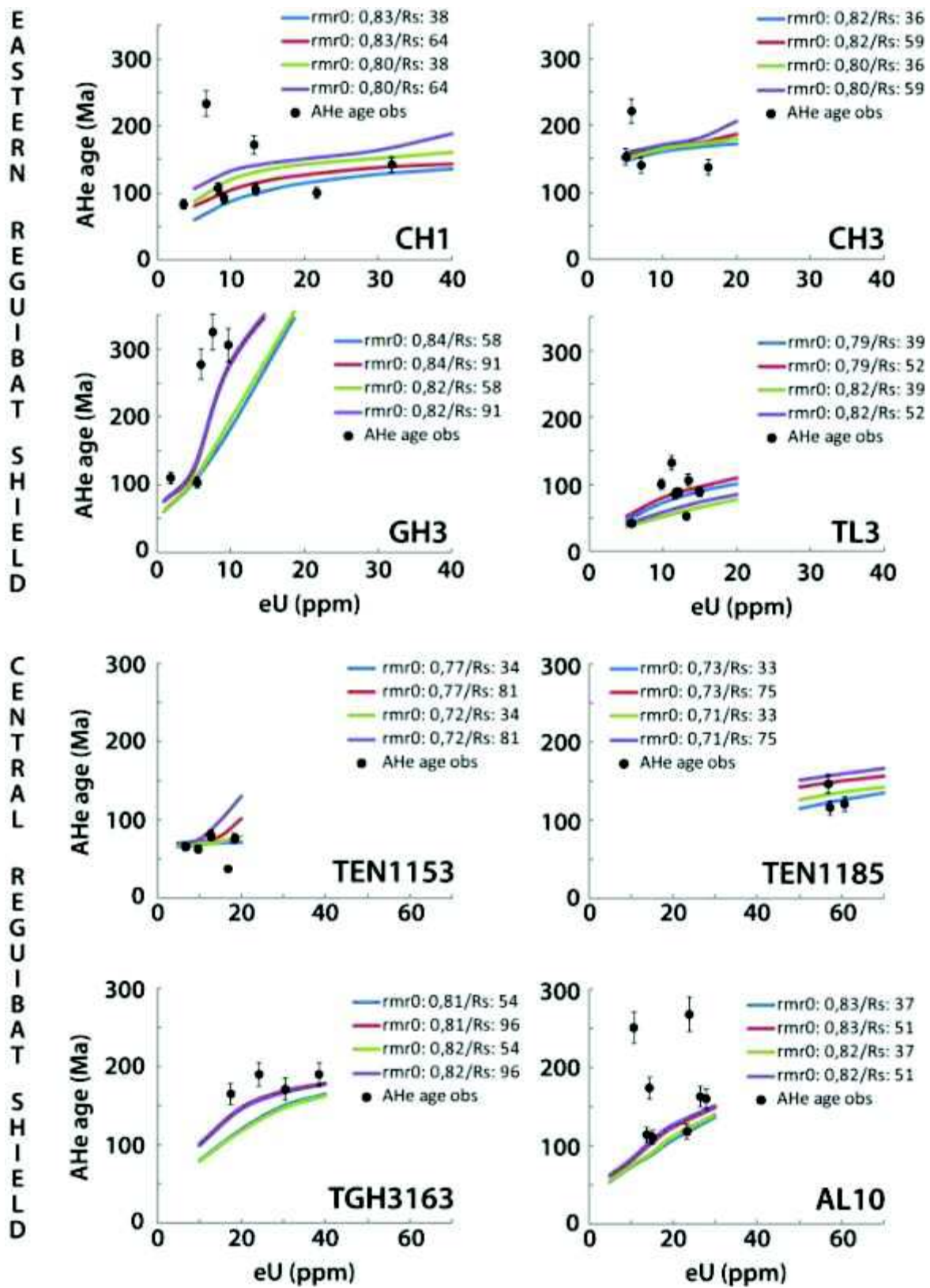


Table S1: AFT results* for the Reguibat Shield

Reguibat Central

Sample	Rock-type	Location	Elevation (m)	ρ_s	ρ_i	ρ_d	P (χ^2) %	Central age (Ma) $\pm 1\sigma$	U (ppm)	MTL (μm) $\pm se$	Std dev.	Dpar
TEN1153	gabbro	10° 30' 36"W 24° 1' 12"N	216	0.759 581	0.333 255	6.14 4738	73	256 \pm 21 23	7	12.3 \pm 0.22 102	2.3	2.89 \pm 0.29
TEN1185	gabbro	10° 30' 0"W 24° 6' 36"N	236	2.652 875	1.806 596	6.07 4738	62	163 \pm 10 23	36	12.4 \pm 0.21 101	2.1	1.13 \pm 0.43
TGH3163	granite	9° 52' 48"W 24° 52' 48"N	305	1.546 881	1.219 695	5.99 4738	44	139 \pm 9 20	25	11.9 \pm 0.18 101	1.8	1.95 \pm 0.12
TGH4072A	granite	9° 43' 12"W 24° 28' 48"N	273	1.784 883	0.964 477	5.92 4738	68	199 \pm 13 20	20	12.4 \pm 0.15 113	1.6	1.02 \pm 0.11
TGH3111B	granite	9°22'12"W 24° 00'00"N	252	3.246 1097	2.598 878	6.611 6563	65	150 \pm 8 20	48	11.9 \pm 0.17 101	1.7	1.63 \pm 0.06
TEN4065	microgranite	10° 1'47.00"W 24°20'23.00"N	258	6.444 754	4.462 522	6.595 6563	8	172 \pm 13 20	82	11.7 \pm 0.33 35	2	2.06 \pm 0.53
AL10	granodiorite	7° 7'5.15"W 26°37'33.06"N	394	1.334 675	0.866 438	7.255 6849	63	202 \pm 14 20	15	12 \pm 0.23 49	1.6	1.77 \pm 0.12
YT7	monzogranite	7°20'37.34"W 26°28'59.39"N	384	1.862 1380	1.394 1033	6.825 6849	72	166 \pm 8 20	25	11.4 \pm 0.25 49	1.8	1.60 \pm 0.19

Reguibat West

Sample	Rock-type	Location	Elevation (m)	ρ_s	ρ_i	ρ_d	P (χ^2) %	Central age (Ma) $\pm 1\sigma$	U (ppm)	MTL (μm) $\pm se$	Std dev.	Dpar
AOS2	syénite neph	14°17'W 22°32'N	400	1.1237 654	1.258 732	6.61 6528	2	107 \pm 8 21	23	11.8 \pm 0.24 56	1.8	1.65 \pm 0.27
AOS3	syénite neph	14°17'W	400	1.899	1.772	6.58	63	128 \pm 6	33	11.9 \pm 0.16	1.6	1.65 \pm 0.27

		22°32'N		1301	1241	6528		21		100		
AOS5	syénite neph	14°17'W	400	1.381	1.308	6.55	1	128 ± 8	24	11.8 ± 0.19	1.8	1.79 ± 0.33
		22°32'N		1153	1092	6528		21		92		
SC11	granite	14°21'38"W	293	0.85	0.627	6.5	50	160 ± 11	12	12.1 ± 0.33	1.8	1.75 ± 0.28
		22°34'36"N		604	446	6528		21		32		
SC12	granite	14°23'00"W	292	1.383	1.155	6.47	27	141 ± 8	22	12.2 ± 0.17	1.8	1.54 ± 0.22
		22°35'14"N		1094	914	6528		21		108		
TCH7	granite	15° 6'37.25"W	194	0.955	0.889	6.52	27	127 ± 8	17	9.4 ± 0.27	2	1.60 ± 0.36
		21°50'54.88"N		916	853	6528		21		37		
SC5	granite	14°29'38.00"W	284	1.04	0.839	6.657	< 1	156 ± 15	15	10.7 ± 0.31	1.7	1.63 ± 0.10
		22°40'50.00"N		1131	913	6563		20		32		
SC9	granite	14°18'56.00"W	318	1.742	1.549	6.641	< 1	143 ± 13	28	11.2 ± 0.35	1.9	1.70 ± 0.11
		22°33'8.00"N		866	770	6563		20		31		
SC15	granite	14°28'52.00"W	282	0.6	0.425	6.626	10	175 ± 16	8	-	-	1.70 ± 0.12
		22°40'17.00"N		482	341	6563		20		-	-	
TAS29	gneiss	15°32'55.96"W	110	0.743	0.778	6.586	11	115 ± 6	14	12.2 ± 0.25	1.8	1.70 ± 0.12
		20°59'34.10"N		1047	1096	6849		20		51		
AG167	charnockite	13°24'2.07"W	233	0.218	0.195	6.73	74	137 ± 12	4	-	-	1.72 ± 0.08
		20°42'56.76"N		323	289	6849		20		-	-	
AG169	charnockite	13°24'2.07"W	237	0.201	0.207	6.682	93	118 ± 10	4	-	-	1.54 ± 0.17
		20°42'56.76"N		309	319	6849		20		-	-	
TAS233	volcanite	15°32'55.96"W	110	0.68	0.651	6.634	87	126 ± 7	12	12.5 ± 0.18	1.8	1.63 ± 0.15
		20°59'34.10"N		797	763	6849		20		102		

Reguibat East

Sample	Rock-type	Location	Elevation (m)	ρ_s	ρ_i	ρ_d	P (χ^2) %	Central age (Ma) $\pm 1\sigma$	U (ppm)	MTL (μm) $\pm se$	Std dev.	Dpar
IG3	rhyolite	6° 9'0.43"W	366	0.469	0.149	6.968	84	393 \pm 36	3	-	-	1.66 \pm 0.16
		26° 6'22.40"N		<i>543</i>	<i>172</i>	<i>6849</i>		20				
CH1	gabbrodiorite	3°35'36.69"W	252	1.098	0.454	7.159	6	307 \pm 26	8	11.5 \pm 0.21	2.1	1.86 \pm 0.19
		25°35'45.94"N		<i>862</i>	<i>356</i>	<i>6849</i>		20		<i>101</i>		
CH2	gabbrodiorite	3°35'36.69"W	252	3.105	1.516	7.112	18	264 \pm 21	26	12 \pm 0.2	1.7	1.99 \pm 0.17
		25°35'45.94"N		<i>770</i>	<i>376</i>	<i>6849</i>		20		<i>69</i>		
CH3	gabbrodiorite	3°35'36.69"W	252	1.059	0.426	7.064	86	315 \pm 24	7	11.5 \pm 0.29	2.3	1.95 \pm 0.18
		25°35'45.94"N		<i>686</i>	<i>276</i>	<i>6849</i>		20		<i>64</i>		
GH3	trondhjemite	6° 3'54.77"W	360	1.177	0.41	7.016	6	359 \pm 27	7	11.5 \pm 0.19	1.9	1.76 \pm 0.16
		25°29'36.53"N		<i>1130</i>	<i>394</i>	<i>6849</i>		20		<i>100</i>		
DEG6	gabbro	2°57'15.60"W	355	2.276	0.701	6.111	46	355 \pm 25	12	11.2 \pm 0.41	2.1	1.97 \pm 0.11
		26° 4'50.02"N		<i>1065</i>	<i>328</i>	<i>6849</i>		20		<i>27</i>		
GH20	gabbro	6° 0'2.87"W	350	0.471	0.101	5.996	73	497 \pm 61	2	-	-	1.75 \pm 0.13
		25°32'51.89"N		<i>206</i>	<i>44</i>	<i>3012</i>		10		-		
TL3	gabbro	3°10'37.45"W	381	0.818	0.376	6.052	66	237 \pm 21	8	-	-	2.12 \pm 0.19
		27°21'31.99"N		<i>447</i>	<i>207</i>	<i>3012</i>		20				

* ρ – density of tracks with s and i – spontaneous and induced densities in apatite crystals and the mica detector; d – tracks density of the neutron glass monitor (CN5); for ρ_d is written in italics the number of counted tracks. Densities are expressed in 10^5t/cm^2 . MTL – mean track length. Values in italics for central age and MTL are, respectively, the number of single-grain ages and the number of lengths measured. 1σ is the standard deviation. Dpar corresponds to a kinetic factor determined for each sample (Barbarand *et al.*, 2003).

Table S2: AHe results* for the whole Reguibat Shield

Reguibat Central

Name	Rs (μm)	Weight(μg)	FT	4He(ncc/g)	U (ppm)	Th (ppm)	Sm (ppm)	eU (ppm)	Age (Ma)	Age c. (Ma)*	s.d.
1185C	52,1	3,11	0,756	678000	45,4	63,3	NA	60,6	104	138	11
1185D	74,5	10,33	0,849	868000	44,4	51,6	-	56,8	142	167	13
1185E	33,4	1,02	0,65	530000	39,4	74	-	57,1	86	133	11
1153-A	80,8	11,85	0,87	46201,6	3,8	11,9	7,0	6,7	57	66	5
1153D	34,4	1,17	0,715	120399,0	10,4	31,9	20,3	18,3	55	77	6
1153-F	63,2	6,54	0,815	100000,8	7,6	20,3	9,5	12,6	66	81	6
1153-H	59	4,69	0,83	63086,4	11,2	22,6	12,5	16,7	31	38	3
1153-I	47,5	2,56	0,79	57756,0	5,5	16,8	13,3	9,6	50	63	5
1153-J	71,5	8,33	0,87	58868,8	5,6	17,0	12,9	9,7	50	58	5
3163-A	54,1	3,6	0,809	717183,1	37,7	1,9	27,2	38,3	155	191	15
3163-E	66	7,11	0,827	288616,5	16,9	1,4	17,6	17,4	137	166	13
3163-I	65,6	6,26	0,847	470679,8	17,8	25,6	24,6	24,1	162	191	15
3163G	96,1	17,27	0,875	549045,6	25,0	22,0	NA	30,3	150	172	14
AL10-A	46	2,4	0,755	405681,5	22,5	20,6	31,8	27,7	121	161	13
AL10-E	39,3	1,18	0,701	675195,0	76,1	26,7	31,3	82,8	67	96	8
AL10-C	50,5	3,53	0,765	229447,2	11,1	11,9	29,3	14,2	134	175	14
AL10-L	44,1	1,57	0,679	1341456,8	34,3	31,1	59,4	42,2	263	388	31
AL10-J	37,2	1,22	0,724	231868,3	7,9	10,0	37,4	10,5	182	252	20
AL10-I	45,5	2,02	0,76	395904,9	22,4	14,9	41,0	26,3	124	164	13
AL10-B	39	1,39	0,726	557702,2	20,6	11,6	37,5	23,7	195	269	21

AL10-K	37,9	1,28	0,717	145483,1	12,5	8,8	35,5	14,9	81	112	9
AL10-F	38,7	1,23	0,687	129286,7	9,5	15,8	44,8	13,6	79	115	9
AL10-G	39,9	1,23	0,707	1327362,4	32,4	26,5	65,3	39,3	280	396	32
AL10-H	42,6	1,58	0,713	236976,2	18,4	18,2	50,1	23,2	85	119	10

Reguibat West

Name	Rs (µm)	Weight(µg)	FT	4He(ncc/g)	U (ppm)	Th (ppm)	Sm (ppm)	eU (ppm)	Age (Ma)	Age c. (Ma)*	s.d.
AOS3A	57,7	4,14	0,781	379655,5	29,6	40,2	403,0	42,5	74	95	8
AOS3B	48,3	2,56	0,786	368565,3	29,6	47,8	167,0	42,4	72	92	7
AOS3C	58,4	5,02	0,803	168335,8	27,7	28,6	318,0	37,1	38	47	4
AOS3E	55	3,82	0,806	317447,5	50,1	31,7	391,0	60,9	43	54	4
AOS5A	54,4	3,77	0,843	17656,2	9,4	7,6	125,0	12,3	12	14	1
AOS5D	48,7	2,8	0,736	59629,6	17,5	16,4	263,0	23,5	21	29	2
AOS5F	48,2	2,27	0,754	175595,4	29,5	24,2	195,0	36,9	39	52	4
AOS2A	58,6	4,48	0,783	252824,1	31,0	12,2	400,0	37,2	56	72	6
AOS2B	62,7	6,65	0,812	219640,8	23,1	16,3	105,0	27,8	65	81	6
AOS2C	47	2,35	0,777	47197,6	14,8	11,6	152,0	18,8	21	27	2
AOS2D	43,8	1,96	0,756	77464,5	20,3	30,6	179,0	29,1	22	29	2
TCH7A	49,4	2,8	0,802	194360,7	59,4	34,9	179,0	69,2	23	29	2
TCH7B	68,7	8,03	0,833	137470,0	19,1	23,5	339,0	27,5	41	50	4
TCH7C	63,6	6,25	0,823	318644,3	43,4	11,1	229,0	47,9	55	67	5
TCH7D	64,6	6,31	0,838	106663,8	13,5	8,9	267,0	17,8	50	59	5

SC5A	46,9	2,61	0,756	209790,4	20,7	5,3	83,0	22,6	77	101	8
SC5C	56,6	4,35	0,802	26663,6	6,3	6,0	16,0	7,9	28	35	3
SC5D	59,9	5,69	0,802	214046,7	26,8	10,6	14,9	29,5	60	75	6
SC9B	59,9	5,4	0,809	59285,0	6,7	11,6	271,0	11,7	42	52	4
SC9D	41,4	1,92	0,717	282683,0	26,7	37,2	274,0	37,9	62	86	7
SC9E	45,8	2,35	0,761	606340,6	52,0	65,8	401,0	71,0	71	93	7
SC11C	50,3	3,01	0,782	18223,7	4,7	4,0	284,0	7,9	19	24	2
SC11D	68	7,34	0,839	92903,5	7,3	13,5	228,0	12,4	62	74	6
SC11E	53,2	2,98	0,775	157369,9	11,4	25,5	103,0	18,4	71	92	7
SC11F	66,7	5,97	0,815	47092,6	8,2	2,9	266,0	11,0	35	43	3
SC12A	41,6	1,65	0,749	108423,6	9,6	13,1	232,0	14,6	61	82	7
SC12D	64	6,22	0,827	180770,1	19,1	9,4	241,0	23,3	64	78	6
SC12G	49,5	2,44	0,754	222394,6	22,1	12,8	141,0	26,3	48	63	5
SC12F	52,3	2,8	0,77	151382,1	24,6	25,6	360,0	33,7	55	71	6
SC15A	59,7	4,73	0,833	141643,9	10,6	16,3	382,0	17,5	67	80	6
SC15B	56,5	3,7	0,782	16790,6	3,6	8,7	126,0	6,7	21	27	2
SC15F	48,3	2,27	0,747	50901,3	5,6	19,5	90,0	11,0	39	52	4
SC15G	56,5	3,99	0,828	234089,4	25,4	23,6	340,0	33,8	57	69	6
T233-B	52,5	3,31	0,833	87654,0	9,1	2,6	12,9	9,8	74	89	7
T233-H	55,5	4,01	0,803	163091,7	35,9	12,9	9,4	39,0	35	43	3
T233-D	49,3	1,4	0,678	263063,3	27,0	7,2	30,6	29,0	75	111	9
T233-G	58,8	4,58	0,822	55323,1	6,5	1,9	14,3	7,0	65	79	6
T233-F	49,7	2,85	0,786	127884,5	12,9	3,2	12,5	13,7	77	98	8
TAS29A	66,7	5,97	0,815	168827,7	14,1	5,4	12,1	15,4	90	111	9

TAS29B	42,1	2	0,767	238975,6	16,0	16,9	27,9	20,1	98	127	10
TAS29C	50	2,57	0,758	196139,6	19,6	4,9	10,1	20,8	78	102	8
TAS29D	56,9	3,14	0,748	196541,4	10,7	3,9	13,1	11,7	138	185	15
TAS29E	71,4	7,22	0,84	57789,0	7,2	1,8	6,5	7,6	62	74	6

Reguibat East

Name	Rs (μm)	Weight(μg)	FT	4He(ncc/g)	U (ppm)	Th (ppm)	Sm (ppm)	eU (ppm)	Age (Ma)	Age c. (Ma)*	s.d.
CH1-A	47,3	2,43	0,789	79475,1	7,2	6,9	5,3	9,0	74	93	7
CH1-B	56,4	4,13	0,809	28513,1	2,7	3,2	1,4	3,5	68	84	7
CH1-C	49,4	2,68	0,802	48729,7	13,1	11,1	5,3	15,8	26	32	3
CH1-D	40,2	1,45	0,751	205297,8	10,1	12,5	5,6	13,1	130	173	14
CH1-F	38,8	1,31	0,754	127741,1	11,0	9,6	3,4	13,3	80	106	8
CH1-G	64	6,37	0,831	88950,2	6,2	8,5	5,1	8,2	90	108	9
CH1-H	37,9	1,28	0,717	392039,3	26,1	23,4	6,0	31,8	102	143	11
CH1-J	50,6	3,96	0,761	141712,3	5,0	6,5	4,5	6,6	178	234	19
CH1-K	40,7	1,74	0,723	190623,3	19,0	10,3	14,9	21,6	73	101	8
CH3-C	50,5	3,04	0,789	119938,2	4,2	5,9	3,7	5,7	175	222	18
CH3-F	35,5	0,96	0,717	191786,5	13,4	11,3	4,2	16,1	99	138	11
CH3-A	54,7	4,25	0,79	93992,9	5,7	5,5	3,2	7,0	111	141	11
CH3-G	59,2	6,11	0,793	71843,0	3,7	5,0	2,7	4,9	122	153	12
GH3A	66,1	7,49	0,823	292746,2	8,1	5,6	12,7	9,6	253	307	25
GH3B	91,1	21,74	0,876	172995,7	4,7	4,6	6,4	5,9	243	278	22
GH3-C	71,5	8,99	0,842	56806,1	4,5	3,5	8,9	5,4	88	104	8
GH3-E	57,9	4,06	0,784	230520,3	6,5	3,8	10,8	7,5	256	326	26
GH3-F	99	19,03	0,883	21444,4	1,7	0,4	2,2	1,8	98	111	9

IG3-C	43,8	1,72	0,722	332846,2	18,1	18,9	44,7	23,0	120	166	13
IG3-E	39,4	1,31	0,686	191182,1	5,0	10,0	48,9	7,8	203	295	24
IG3-F	36,7	0,99	0,675	118582,6	3,8	10,9	47,2	6,8	146	216	17
IG3-G	40,6	1,56	0,741	91106,9	3,7	4,9	38,8	5,1	147	198	16
IG3-I	40,4	1,67	0,721	187725,0	3,9	5,5	49,9	5,6	277	384	31
TL3-L	41,1	1,58	0,745	131554,4	6,3	18,8	29,8	11,1	99	133	11
TL3-B	49,4	2,68	0,803	66784,2	8,8	17,0	23,8	13,1	42	53	4
TL3-C	41,3	1,57	0,778	73141,8	9,2	43,5	27,0	19,8	31	40	3
TL3-D	39	1,44	0,717	86327,5	6,3	20,9	33,8	11,6	62	87	7
TL3-F	41,4	1,92	0,717	123516,5	7,1	25,1	35,2	13,4	77	107	9
TL3-G	43,5	1,98	0,745	95782,6	6,4	21,9	34,3	12,0	67	89	7
TL3-J	52	3,29	0,797	93130,9	5,4	17,1	25,4	9,7	80	101	8
TL3-H	47	2,35	0,777	123871,0	8,0	27,5	36,9	14,9	69	89	7
TL3-K	46,6	2,77	0,746	21915,9	3,6	8,2	19,6	5,7	32	43	3
											0
GH20-A	36,4	1,14	0,702	58542,3	5,8	5,2	129,6	8,1	60	85	7
GH20-C	37,4	1,28	0,703	74174,8	12,9	6,9	26,5	14,7	42	59	5
GH20-D	37,4	1,28	0,703	54325,7	5,9	5,1	31,4	7,3	61	87	7
GH20-F	41,1	1,58	0,745	34723,6	4,1	5,3	30,5	5,7	51	68	5
GH20-H	35,1	1,22	0,663	37173,2	9,5	6,2	37,8	11,2	27	41	3
GH20-G	39,2	1,52	0,711	54027,8	11,1	7,0	34,3	13,1	34	48	4

* R_s (sphere equivalent radius) and F_T (ejection factor) have been calculated using the developed procedure of Gautheron & Tassan-Got (2010) and Ketcham *et al.* (2011). eU (effective uranium) has been calculated with the formula $[eU] = [U] + 0.24*[Th] + 0.008*[Sm]$. "Age c." means (U-Th-Sm)/He age corrected from alpha-ejection with the F_T . The error is estimated to be a maximum of 8%.

Table S3: Results from forward modeling of central RS samples

Equivalent sphere radius = 55 μ m

eU (ppm)	AHe age (Ma)	HT1	HT2	HT3	HT4	HT5
5	45	37	42	42	45	79
10	55	46	58	55	54	85
15	78	54	81	81	61	88
20	125	63	106	112	67	90
30	165	82	137	151	75	92
40	180	99	152	171	81	94
60	190	120	167	189	90	95

HT: Thermal History

eU: efficient Uranium